Complete Electrification of Short-Range Aircraft Propulsion Systems

by

Diego García de Vega Yáñez

Submitted to the Department of Electrical Engineering, Electronics, Computers and Systems
in partial fulfillment of the requirements for the degree of
Master of Science in Electrical Energy Conversion and Power Systems
at the
UNIVERSIDAD DE OVIEDO
July 2024

Author . . . .

Certified by . . . .
Daniel Fernández Alonso
Associate Professor
Thesis Supervisor

Certified by . . . .
María Martínez Gómez
Assistant Professor
Thesis Supervisor

Complete Electrification of Short-Range Aircraft Propulsion Systems

by

Diego García de Vega Yáñez

Submitted to the Department of Electrical Engineering, Electronics, Computers and Systems
on 19 of July of 2024, in partial fulfillment of the
requirements for the degree of
Master of Science in Electrical Energy Conversion and Power Systems

Abstract

With growing global concern over climate change, sustainable solutions for industry and transportation see their popularity increased. In this context, electrical energy is being proposed as an alternative to fossil fuels for many sectors such as aviation. This thesis will be the starting point of a long term project related with the electrification of short-range aircraft propulsion systems. More specifically, the possible advantages of a VF-PMSM in the context of aviation are explored. Analysis and design techniques are proposed to address this adoption in the future, as well as some preliminary conclusions on its viability.

Thesis Supervisor: Daniel Fernández Alonso
Title: Associate Professor

Thesis Supervisor: María Martínez Gómez
Title: Assistant Professor

Acknowledgments

I would like to begin this document by expressing my gratitude to my advisors, Daniel Fernández and María Martínez. Their guidance has helped me improve not only during the development of this master's thesis but over the last three years. Thank you for introducing me into research and finding time to come up with solutions for my everyday obstacles. Moreover, I want to extend my gratitude to my groupmates, Diego, Marcos, Lidia and Javier for their assistance and advice whenever needed. Thank you for encouraging me through research difficulties and for making these months more enjoyable with your laughter during coffee breaks. You have made my time at AECP a truly enriching experience and I am confident that it will continue to be so in the future.

Outside of academics, I have nothing but kind words for my friends. Since high school, countless good times I have shared with you have helped me stay happy through both the highs and lows.

Lastly, I would like to express my gratitude to my family, with special appreciation to my parents. I would not have come close to where I am today without their endless care, help and support.

Contents

List of Figures

List of Tables

Chapter 1

Introduction

1.1 Climate change and sustainable mobility

In recent years, societal concern about climate change has reached unprecedented levels, driven by the growing body of scientific evidence and the increasing visibility of its impacts [1]. Central to the discourse on climate change, is the recognition of human activity as a critical driver of the phenomenon. Extensive research and consensus among climate scientists confirm that the burning of fossil fuels, deforestation, and industrial processes are significantly increasing greenhouse gas concentrations in the atmosphere, leading to global warming and climate instability [2][3]. To show this relation, Fig. 1-1 [4] depicts observed global temperature rise (compared to 1960), along with equivalent CO_2 emissions since the end of the industrial revolution. This increasing awareness has derived in a global movement advocating for sustainable practices and policies that mitigate human impact on planet's climate.

Sustainable mobility is increasingly recognised as a critical component in addressing this challenge. Transportation sector is a significant contributor to global greenhouse gas emissions, accounting for up to 16% of all emissions worldwide (See Fig. 1-2, compilation based on [4][5]). Consequently, transforming how people and goods move is essential to reduce the overall carbon footprint and mitigate climate change.

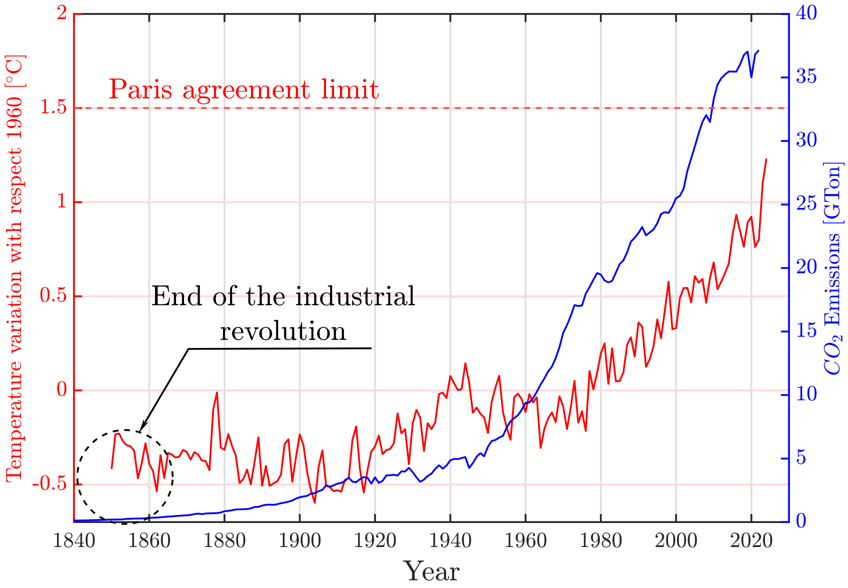

Figure 1-1: Observed temperature rise and equivalent global CO_2 emissions

While accounting for an estimate of only 2% of global emissions, aviation has captured the attention of governments due to its high carbon intensive nature. Despite recent studies showing that aviation industry is reducing its energy intensity over the years, the increased demand, combined with the almost constant carbon emissions per unit of energy have caused aggregated CO_2 emissions to rise [6][7]. Fig. 1-3 (Compilation based on [6][7]) illustrates this evolution over the years[1]. Note how energy needed per km and passenger has almost decreased by half, while the demand of passenger flights has increased up to four times in a 30 years time span. Since fuel composition has remained fairly constant, resulting emissions have approximately doubled in the same time range. Considering that flight demand is not expected to decrease [8][2], governments and companies are trying to evolve towards a more sustainable aviation model.

---

[1] Sudden drop in data is attributed to 2020 COVID-19 pandemic, during which travel restrictions were imposed, growing tendency has been recovered [7]

[2] Currently, an estimate of 10% of world population afford to travel by plane. As developing countries increase their income, the figure is only expected to grow

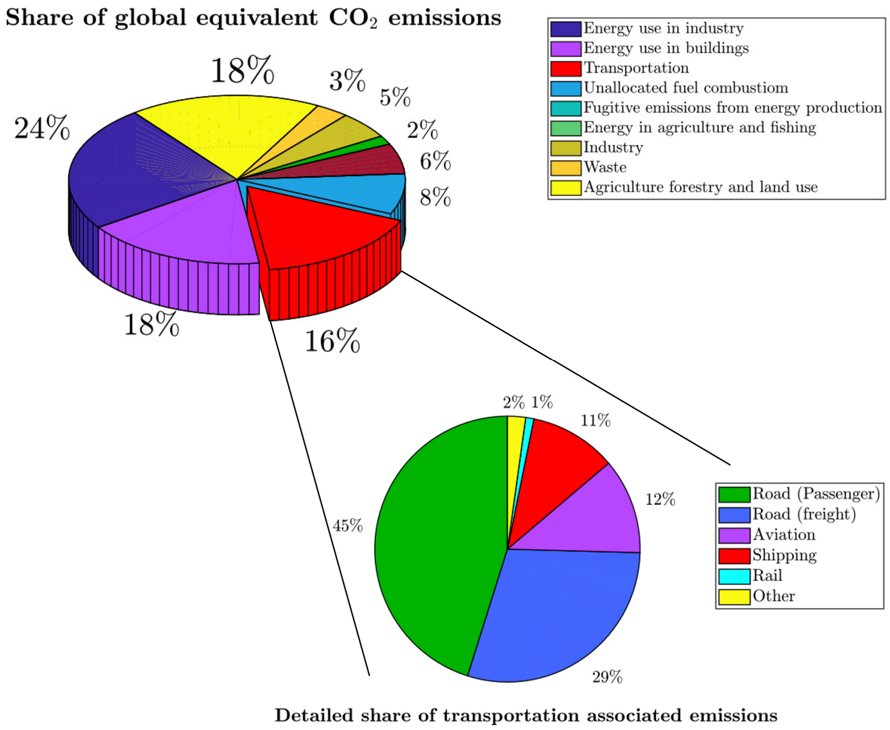
Share of global equivalent CO_2 emissions

Detailed share of transportation associated emissions

Figure 1-2: Equivalent CO_2 emissions per sector

In this context, the Spanish and French governments have recently announced a ban on short flights, as long as a train-based alternative is possible [9]. The policy is meant to fight the rising trend in flight demand, in favour of cleaner, electricity-based solutions such as rail transportation. As regulatory framework and social agents start penalising aviation high carbon-intensity, the need of a sustainable, electricity-based aviation arises [10].

1.2 Electrical machines and drives

Prior to the analysis of electricity-based aviation, a brief overview of electric machines and drives is provided. Fig. 1-4 contains a summarised view of main elements in an electric drive (in the context of electric mobility[3]). As seen in the image, several elements can be identified:

---

[3] Drives can also be fed directly from the grid. However, this is of no use for moving applications like a vehicle

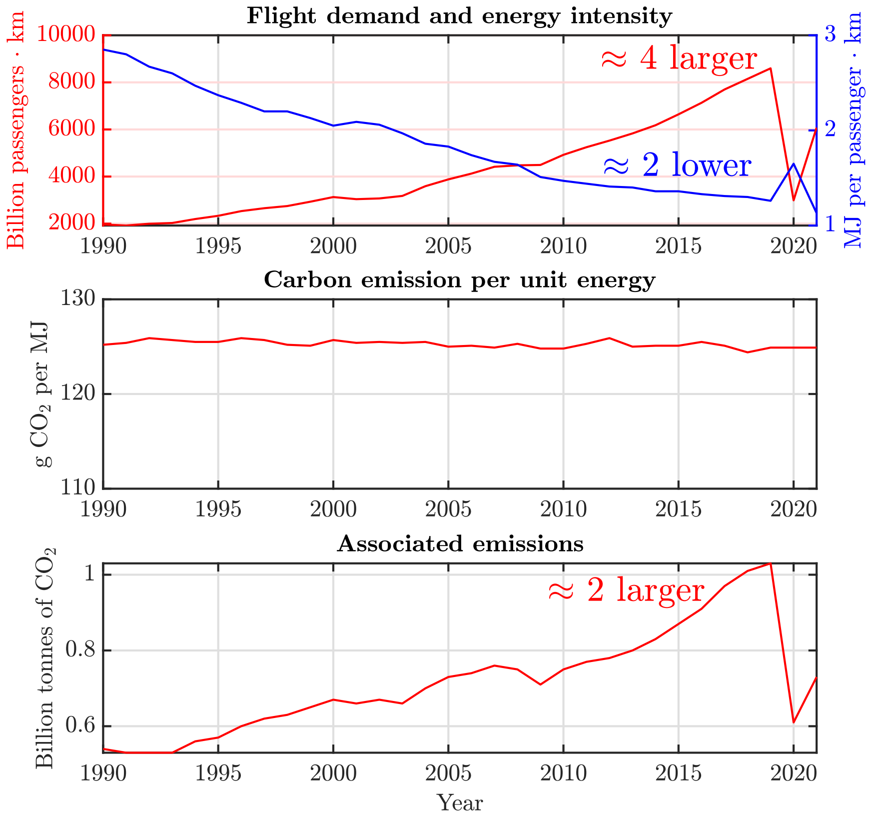

Figure 1-3: Aviation CO_2 emissions explained

- **Energy storage:** Provides energy to the system. Electro-chemical batteries are the most widespread option for electric vehicles [11].

- **Power converter:** Responsible of machine control. Often referred to as an *inverter*, since it converts battery DC voltage into AC voltage (typically 3-phase).

- **Electrical machine:** Electromechanical conversion element. The machine converts electrical power into mechanical power when working in motor mode, and vice versa when working as a generator (regenerative braking).

Present work will mostly be focused in aspects related to electrical machines. Therefore, a brief explanation on their types is provided.

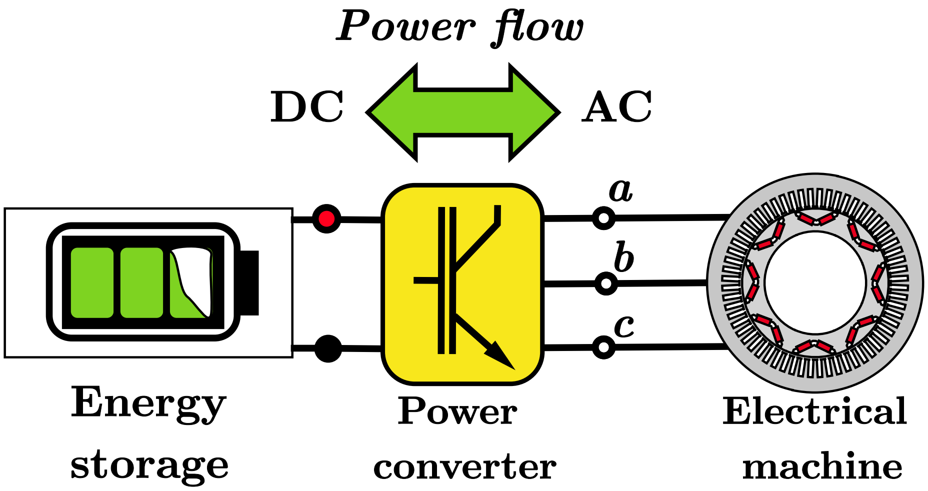

Figure 1-4: Main parts of an electric drive

1.2.1 Electrical machine types

Electrical machines, essential in converting electrical energy into mechanical energy and vice versa, are key in the industrial world. They can be broadly classified into Direct Current (DC) machines and Alternating Current (AC) machines.

DC machines were historically significant due to its simple and precise speed control and high starting torque. However, they need brushes and commutators to maintain unidirectional torque, increasing their maintenance cost. Additionally, they generally have lower efficiency compared to AC machines. Due to these drawbacks, their have been reduced over time to specific applications [12].

AC machines are typically divided into synchronous and asynchronous machines. They have displaced the DC machine due to their higher efficiency and lower maintenance [13][14]. They may be design-adapted to fit a wide range of applications, from small household devices to large industrial equipment. Additionally, manufacturing and operational costs of AC machines are generally lower due to simpler construction and widespread availability of AC power [12].
Out of the AC machines, most relevant types in the context of sustainable mobility are [15]:

- **Induction (asynchronous) machines**: Induced currents in its conductive rotor produce torque. Widely used thanks to its robustness, simplicity, and low cost, primarily in industrial and household applications [16].

- **Permanent Magnet Synchronous Machines**: Permanent magnets are placed on the rotor to create a constant magnetic field and thus torque when the stator is fed. They are known for high efficiency and performance, commonly used in electric vehicles and industrial automation.[12]

- **Synchronous Reluctance Machines**: Operates by reluctance torque with no rotor windings or magnets. This machine type is valued for its high efficiency and simplicity. Its typically incorporated in static applications due to its high volume and weight.

- **Wound Rotor Synchronous Machines**: They feature a rotor winding supplied by an external DC source, allowing for precise control of power factor and used in applications requiring high starting torque [16].

Fig. 1-7 and Table 1.1 contain, respectively, typical aspect of these machines, and their summarised characteristics [14].

	AC Machines			
	Asynchronous	Synchronous		
	IM	**WRSM**	**PMSM**	**SynRM**
Efficiency at low speeds	✓✓	✓✓	✓✓✓	✓✓
Efficiency at high speeds	✓✓✓	✓✓	✓✓	✓
Torque density	✓	✓	✓✓✓	✓
Power density	✓	✓	✓✓✓	✓
Temperature robustness	✓	✗	✗✗	✓✓
Maintenance	✓	✗	✓	✓
Torque ripple	✗	✗	✗✗✗	✓
Cost	✓	✓	✗✗	✓

Table 1.1: Summarised comparison among most used electrical machines

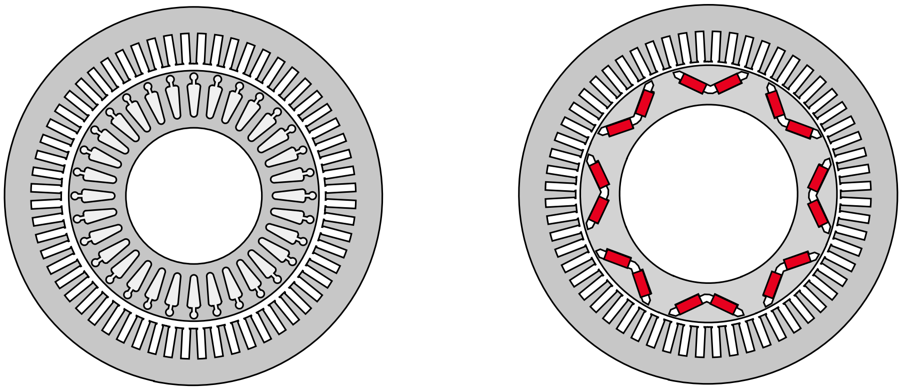

(a) IM (b) PMSM

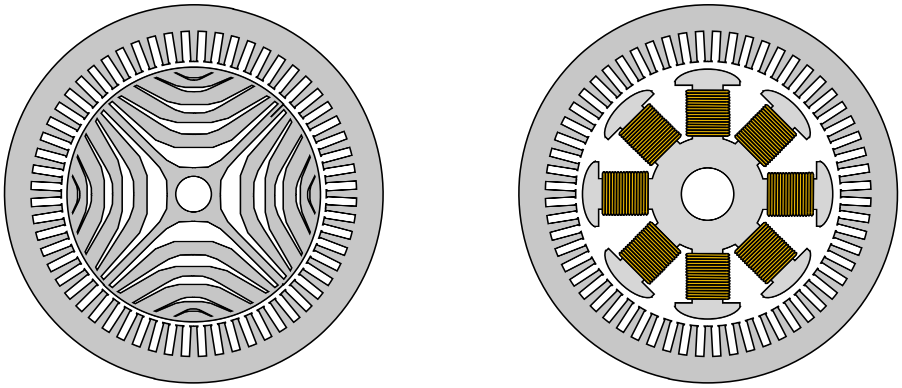

(c) SynRM (d) WRSM

Figure 1-5: Most common machines in electrical vehicles

1.3 Permanent Magnet Synchronous Machines

Rapid development of magnetic materials over the course of last century has promoted their use on electrical machines. Fig. 1-6 depicts how permanent magnets have evolved quadratically in terms of energy density [17].

For this reason, PMSMs have become the most torque and power dense kind of AC machines. These attributes combined with the development of power electronics, and control strategies, have led to a rapid integration of PMSMs in traction applications [14]. However, rare-earth magnets can limit the operation of the machine at high speeds. Induced voltage becomes too high and *field weakening* operation is needed, decreasing efficiency. Additionally, rare earth magnets are typically expensive in terms of cost, and their price tends to oscillate due to political restrictions [18].

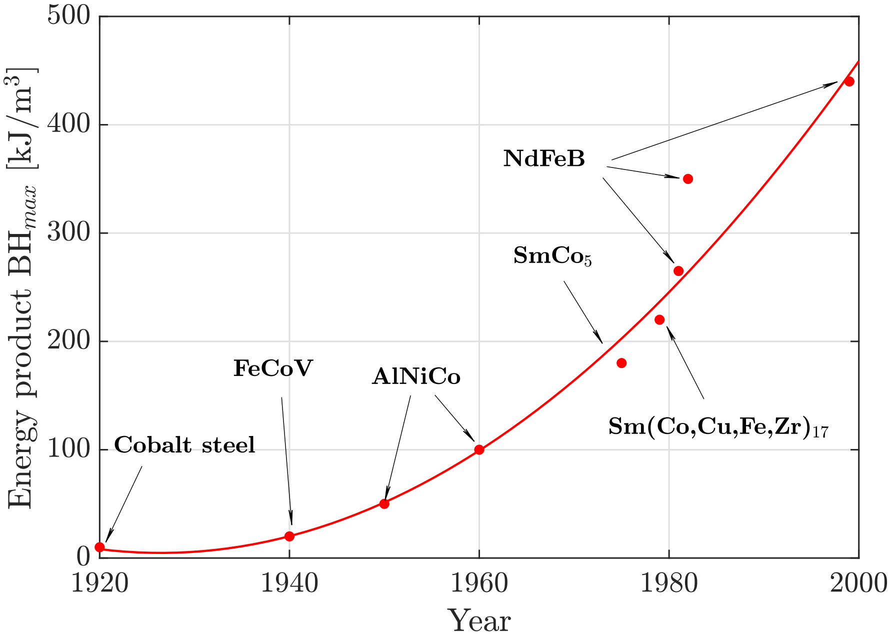

Figure 1-6: Permanent magnet materials energy product evolution

Variable Flux PMSMs (VF-PMSMs) were first proposed to solve these drawbacks in [19], and have recently gained interest in literature [18][20][21]. Key aspect of VF-PMSM is their magnetization state (MS) manipulation capability, even during machine operation. By combining proper design and permanent magnets, short current pulses can be used to reduce induced voltage [19]. Fig. 1-7a contains a conventional and a variable-flux type PMSM.

Since magnetization state of the permanent magnets can be modified, available machine torque and stator induced voltage can be controlled.Previous feature is beneficial to improve efficiency at high speeds, where torque demand is low and induced voltage may reach converter limits.

However, for this feature to be exploited, machine operating points must be known in advance, in order to adapt magnetization state to torque requirements. This may be difficult for applications such as passenger cars, but could be feasible in other applications inside transportation like railway or aircraft. Additionally, it could also be integrated into the industrial world or home appliances.

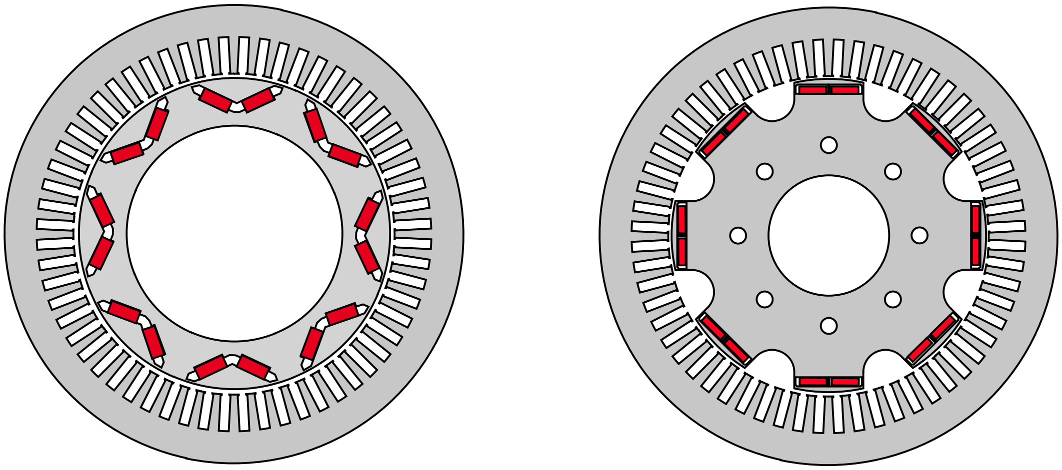
(a) Conventional (b) Variable Flux

Figure 1-7: Conventional and variable flux type PM machines

Previous consideration is illustrated in Fig. 1-8, in which power requirements for a passenger car and a commercial plane are compared. Requirements in an average passenger car depend on uncontrollable external factors, as represented by WLTP cycle[4] shown in red in the image, and is therefore difficult to know if the driver will demand torque or not. On the contrary, flight missions have a much higher degree of predictability. Flights are often summarized to takeoff, cruise, and landing. Even if reality can be more complex, predictability can still be assumed compared to other applications.

---

[4] *World Harmonized Light-Duty Vehicle Test Procedure* (WLTP) is a global standard used to address power consumption on light-duty vehicles. Developed by the United Nations in 2009, it models a representative trip in terms of linear speed for a light-duty vehicle

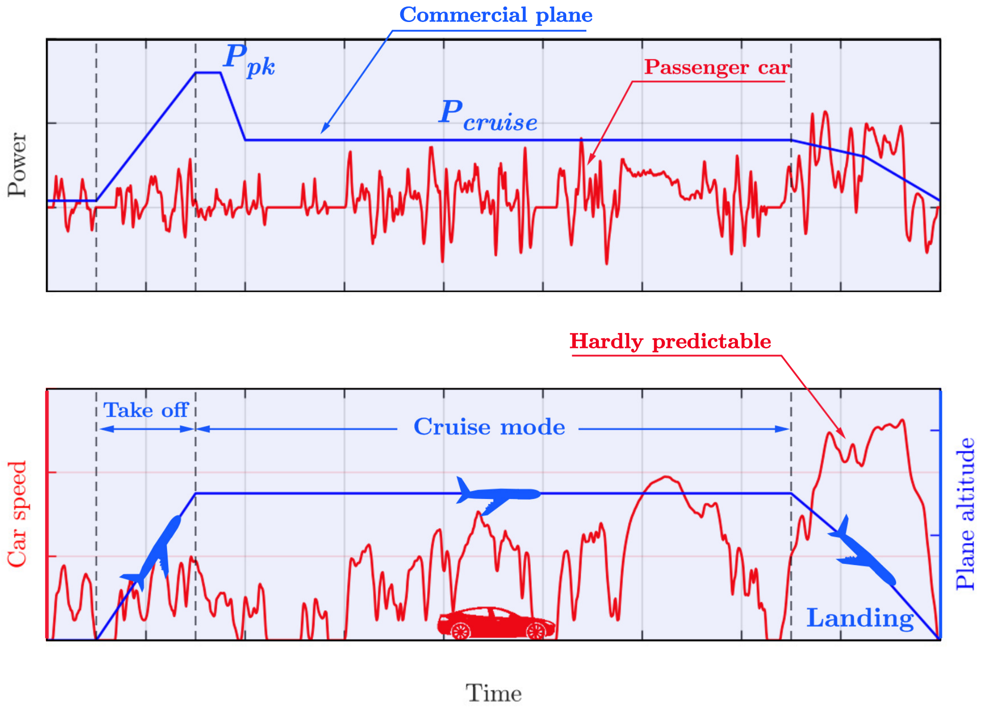

Figure 1-8: Commercial plane and average passenger car power profiles

Chapter 2

Goals and Scope

As previously stated, the integration of VF-PMSMs into some applications has the potential to improve their efficiency, thus reducing energy consumption. This adoption could therefore help in the development of more sustainable forms of transportation. To date, no commercial traction application has successfully achieved this integration[5] due to design, reliability and control challenges, that are currently under study. The following master thesis will be the starting point of a long-term project aiming to study this adoption in detail. Project is leaded and funded by Ingeteam Power Technology SA[6], and will focus in areas such as machine loss production mechanisms, optimized machine design techniques, control strategies, modulation schemes and diagnostics (i.e. thermal and magnetization state detection). All of the above will be integrated to develop a certified electrical machine for aircraft applications.

Complexity of the project requires several preliminary steps to be taken. Being the first of them to build a 25 kW test bench with a first machine prototype. This equipment will be used to assess developed knowledge during initial stages of the project, and is conceptually shown in Fig. 2-1. Then, final goal is to develop the

---

[5] Only registered commercial application for a VF-PMSM is held by Toshiba, who integrated it into a washing machine (patent US8179068B2)

[6] Ingeteam is a Spanish technology company specializing in the development of electrical equipment, motors, generators, and control systems. Founded in 1972, the company focuses on strategic sectors such as renewable energy, power generation, railway traction, marine, and the water industry.

back-to-back converter shown in the image, as well as a VF-PMSM machine prototype[7].

More specifically, and adjusting scope to available time frame for the completion of the completion of this master's thesis, objectives could be listed as follows:

- Comprehend particularities of VF-PMSM against conventional PMSM
- Use finite-element analysis software to achieve:
  - Optimized machine design based on previously developed prototypes, following electromagnetic and structural criteria. For this objective, available algorithms and methods inside this kind of software are explored.
  - Reliable efficiency characterization to predict potential impact of VF-PMSM on aircraft applications
- Perform experimental tests and use the information as feedback into finite-element simulations, to increase their reliability:
  - Power loss prediction capabilities in a known topology
  - Different magnet characterisation
  - Machine efficiency at different magnetization levels
- Combine experimental and simulation results to predict impact of VF-PMSM adoption in aircraft applications
- Build and test a *back-to-back* power converter to feed the machine in future stages of the project.

---

[7] DC source in the image feeding the converter is already available at the moment

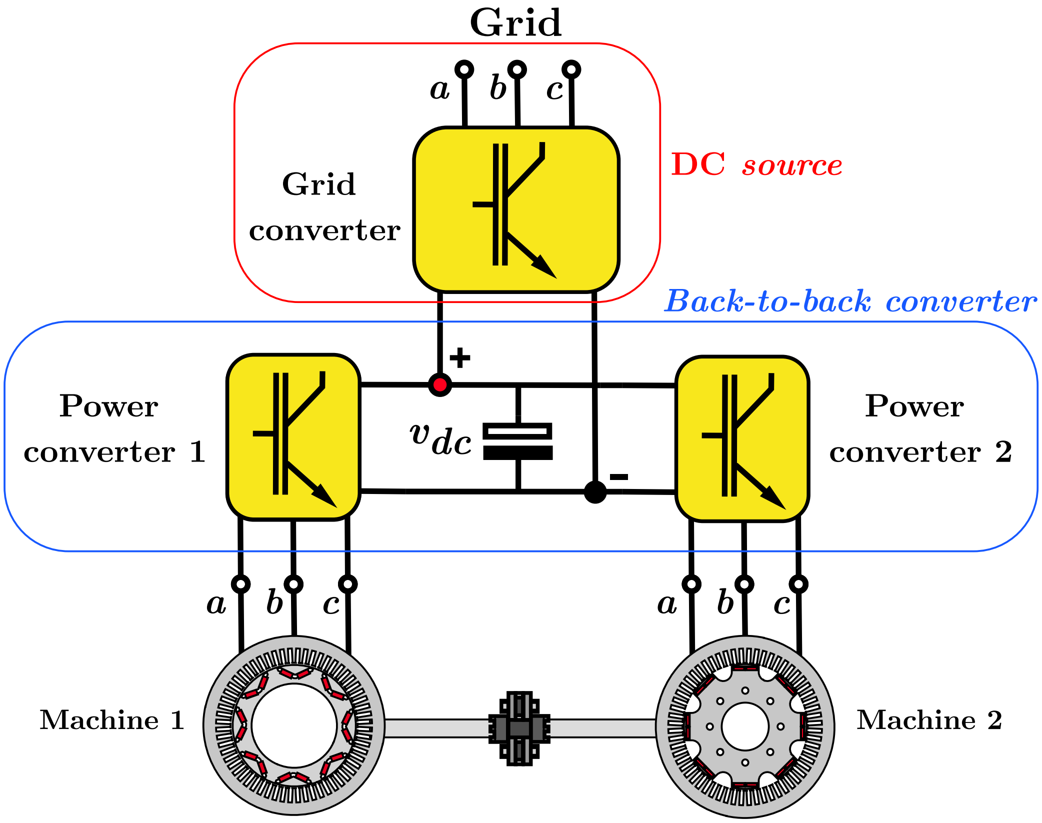

Figure 2-1: Machine prototype test bench

Chapter 3

Theoretical background

3.1 Permanent magnet machines fundamentals

All rotating electrical machines rely on the same operating principle. The interaction between stator magnetic field and rotor magnetic field will produce torque, causing rotor to spin [22]. Electrical machines may be classified according to how this fields are created. While stator magnetic field is always produced with energized windings, rotor field is not so straightforward. It can be generated through either energized windings, conducting bars, or permanent magnets. This section will cover phsycal background behind this last kind of machines.

3.1.1 Operation principle

Consider the situation in Fig. 3-1, in which a ferromagnetic rotor equipped with permanent magnets is placed inside a stator, whose teeth have been filled with copper windings forming phases a, b and c. Also, consider circulating currents to be of the following form, being I current amplitude, and ω its angular frequency.

$$\begin{cases} i_a(t) = \mathrm{I} \cdot \cos\left(\omega t\right) \\ i_b(t) = \mathrm{I} \cdot \cos\left(\omega t - \frac{2\pi}{3}\right) \\ i_c(t) = \mathrm{I} \cdot \cos\left(\omega t + \frac{2\pi}{3}\right) \end{cases} \tag{3.1}$$

Adopting the convention of the phase conductors in the figure, each current will produce a proportional magnetomotive force on its magnetic axis, a_{mag}, b_{mag}, and c_{mag} (in quadrature with the conductors according to Ampere's Law).

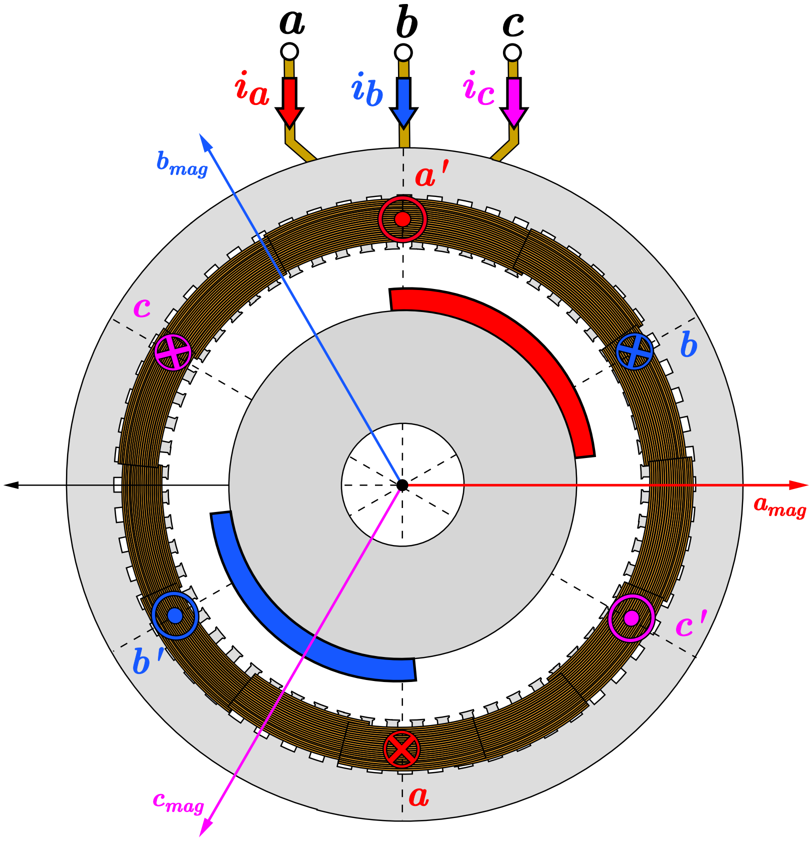

Figure 3-1: Permanent magnet machine principle of operation

Magnetic axes are $\frac{2\pi}{3}$ radians spatially shifted from each other. Therefore, it is convenient do introduce complex operator a as follows:

$$a = e^{\frac{2\pi}{3}j} \tag{3.2}$$

Where j denotes the imaginary unit. Based in Fig. 3-1, the operator allows to express the position in space of each phase magnetic axis in complex form:

$$\begin{cases} a_{mag} = 1 \\ b_{mag} = a \\ c_{mag} = a^2 \end{cases} \tag{3.3}$$

Then, resulting stator magnetomotive force in space at an arbitrary time instant t can be expressed as a function of currents [16]:

$$\overrightarrow{i_{abc}(t)} = k\left[i_a(t) + a \cdot i_b(t) + a^2 \cdot i_c(t)\right] \tag{3.4}$$

Where $\overrightarrow{i_{abc}(t)}$ is usually referred to as the current complex vector [23], and k is the transformation constant. If the following complex identities for the cosine are considered:

$$\begin{cases} \cos(\theta) = \dfrac{e^{j\theta} - e^{-j\theta}}{2} \\ \cos(\theta - \frac{2\pi}{3}) = \dfrac{a^2 \cdot e^{j\theta} - a \cdot e^{-j\theta}}{2} \\ \cos(\theta + \frac{2\pi}{3}) = \dfrac{a \cdot e^{j\theta} - a^2 \cdot e^{-j\theta}}{2} \end{cases} \tag{3.5}$$

Equation (3.4) becomes:

$$\overrightarrow{i_{abc}(t)} = k \cdot \frac{\mathrm{I}}{2}\left[3e^{j\theta} - e^{-j\theta}\cancel{(1 + a + a^2)}\right] = k \cdot \frac{3}{2} \cdot \mathrm{I} \cdot e^{j\omega t} \tag{3.6}$$

Which implies that air-gap magnetomotive force is rotating in space at the same rate as the current angular frequency. If transformation constant k is chosen as $\frac{2}{3}$, the complex vector will have the same amplitude as the currents (amplitude invariant transformation). Main conclusion to be extracted is that the circulation of a balanced three phase current system produces a rotating magnetic field at machine air gap. Rotor magnets will try to align with this field, thus creating torque.

3.1.2 Machine modelling and torque production

Machine modelling requires the introduction of the synchronous reference frame transformation for a complex vector $\vec{f}$ [16]:

$$\vec{f}_e = \vec{f} \cdot e^{-j\theta} \tag{3.7}$$

This operation will align the vector with a reference frame that is displaced by an angle θ with respect phase a magnetic axis. The rotation is of great use in synchronous machines, if a vector is rotating at rate ω and is expressed in a frame that moves at the same frequency, it will become a constant complex number.

This fact can be used to define a reference frame that is synchronized with machine rotor. Consider machine rotor displayed in Fig. 3-2.

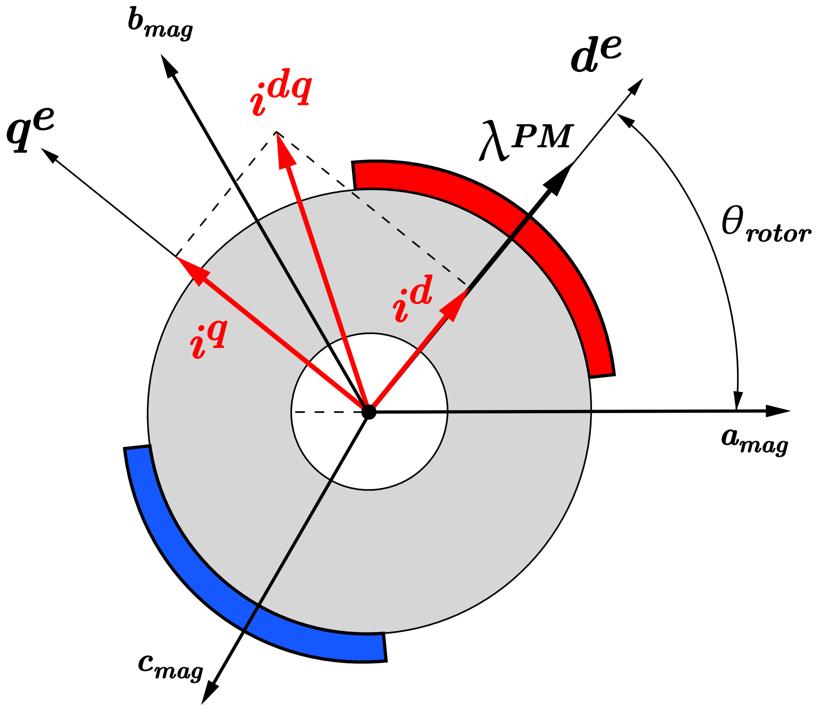

Figure 3-2: Stator current in rotor-synchronous reference frame

In the image, λ_{PM} denotes the location of rotor's north pole and is used to define its direct or d axis. Then, machine stator current can be expressed in the synchronous reference frame to become i_{dq} (where q stands for quadrature). As shown in the image, current vector may be decomposed into its real and imaginary components, namely i_d and i_q [8]. From the image, i_q can be deduced to have impact on torque production, due to its relative position with respect rotor magnetic field. On the other hand, i_d current can be used to affect rotor magnets flux linkage.

After this approach is introduced, electrical model of the machine can be derived. If each phase is considered equal with a resistance of R_s, Kirchhoff's second law states that voltage at any phase is [22]:

$$v(t) = R_s \cdot i(t) + \frac{d\lambda(t)}{dt} \tag{3.8}$$

Where λ denotes flux linked by the corresponding phase winding. The equation can be further generalized to its complex vector form yielding:

$$\overrightarrow{v_{abc}} = R_s \cdot \overrightarrow{i_{abc}} + \frac{d\overrightarrow{\lambda_{abc}}}{dt} \tag{3.9}$$

Explicit time dependence has been dropped for simplicity. If the equation is expressed in a rotor-synchronous reference frame (rotor electrical pulsation being ω_{rotor}), machine electrical model is obtained.

$$\overrightarrow{v_{dq}} = R_s \cdot \overrightarrow{i_{dq}} + \frac{d\overrightarrow{\lambda_{dq}}}{dt} - j\omega_{rotor}\overrightarrow{\lambda_{dq}} \tag{3.10}$$

Considering that rotor d and q axes inductances are not necessarily equal [22][9], they will be denoted by separate variables L_d and L_q respectively. This allows to express flux in each rotor axis as:

$$\begin{cases} \lambda_d = L_d \cdot i_d + \lambda_{PM} \\ \lambda_q = L_q \cdot i_q \end{cases} \tag{3.11}$$

---

[8] The association of d and q with real or imaginary components is dependent on the adopted convention [16]

[9] This is explained by rotor design. If magnets are placed in the surface of the rotor (SPMSM), both axes will have similar reluctance since magnet permeability is similar to that of air. However this is not true for cases in which rotor magnets are placed inside the core (IPMSM), one of the axes will have more iron on its path, thus reducing reluctance and increasing inductance

Combining (3.10) with (3.11) gives rise to the machine electrical model:

$$\begin{cases} v_d = R_s \cdot i_d + L_d \dfrac{di_d(t)}{dt} - \omega_{rotor} L_q i_q \\ v_q = R_s \cdot i_q + L_q \dfrac{di_q(t)}{dt} + \omega_{rotor} (L_d i_d + \lambda_{PM}) \end{cases} \tag{3.12}$$

Where an explicit coupling between the axes can be seen on last terms present in both equations. These velocity-dependent terms are usually referred to as crossed-terms [22], and justify the increasing induced voltage with growing speed.

Finally, electromagnetic torque (T_e) produced by the interaction of rotor and stator magnetic fields is given by 3.13 [16], in which p denotes machine pole pairs:

$$T_e = \frac{3}{2} p \left[\underbrace{\lambda_{PM} i_q}_{T_s} + \underbrace{(L_d - L_q) i_d i_q}_{T_r} \right] \tag{3.13}$$

In the equation, two terms can be identified. First term (T_s) is denoted as synchronous torque. It is dependent on i_q current due to quadrature between i_q and λ_{PM} with rotor magnetic axis, causing maximum torque to be created. Second term (T_r) depends on the difference among rotor inductances, it is typically referred to as reluctance torque [22]. When flux lines cross the rotor, a force is created to align it with the path showing the lower reluctance.

Some conclusions can be extracted from previous modelling process. First, magnet flux linkage will highly influence torque production. Secondly, it will also affect induced voltage, being its influence larger as speed increases.

3.1.3 Vector control and field weakening operation

Previous model has been taken as an advantage from control perspective [16]. Based on (3.11) and (3.13), when current complex vector is expressed in a rotor-synchronous reference frame, its components i_d and i_q can be used to modify rotor flux and torque respectively. Since control is performed by acting directly upon machine complex vectors, this approach receives the name of vector control [16]. Fig. 3-3 depicts a generalized scheme for the implementation of this strategy [23].

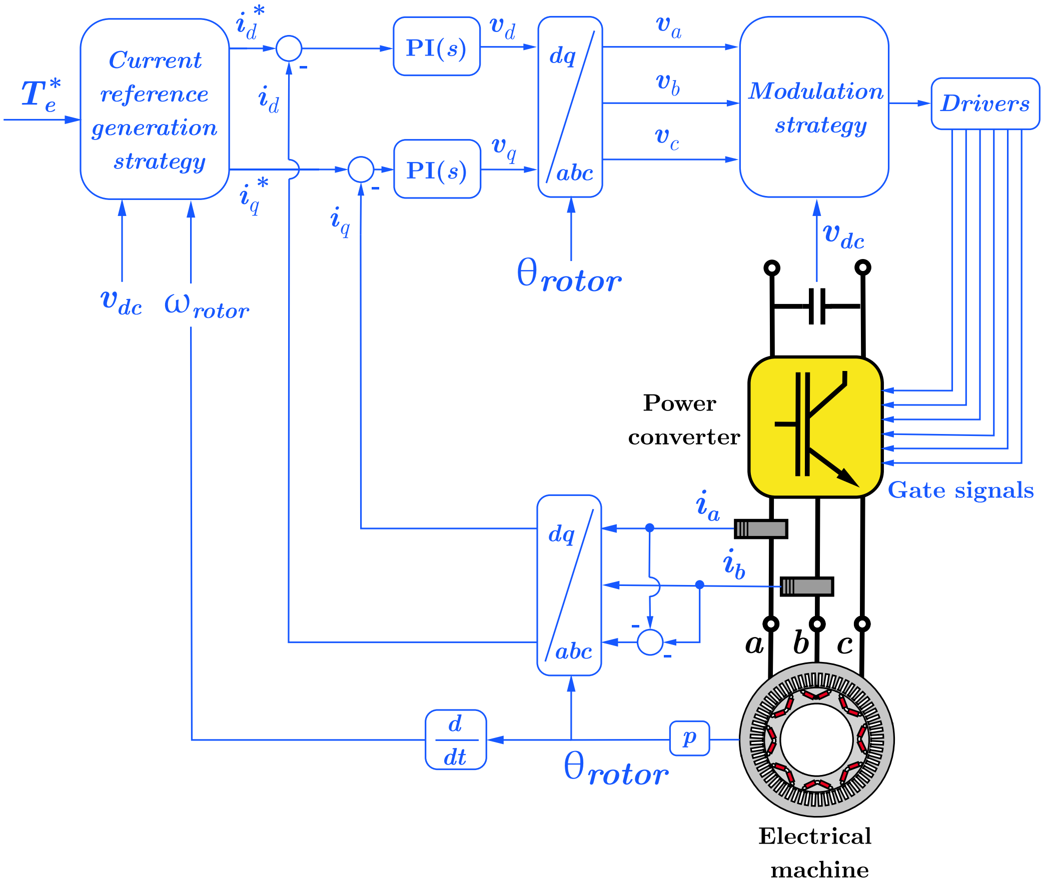

Figure 3-3: Generalized vector control scheme

Machine operation can be broadly divided into two regions: Maximum torque region and field weakening region. Fig. 3-4 displays them, together with the evolution of some of machine key variables.

To properly understand the figure, (3.12) must be examined. Note how in steady state, assuming resistive drop to be negligible, induced voltage magnitude is approximately:

$$|\overrightarrow{v_{dq}}| \approx \omega_{rotor} \cdot |\overrightarrow{\lambda_{dq}}| \tag{3.14}$$

Consequently, when speed is low, induced voltage $\overrightarrow{v_{dq}}$ is below converter voltage

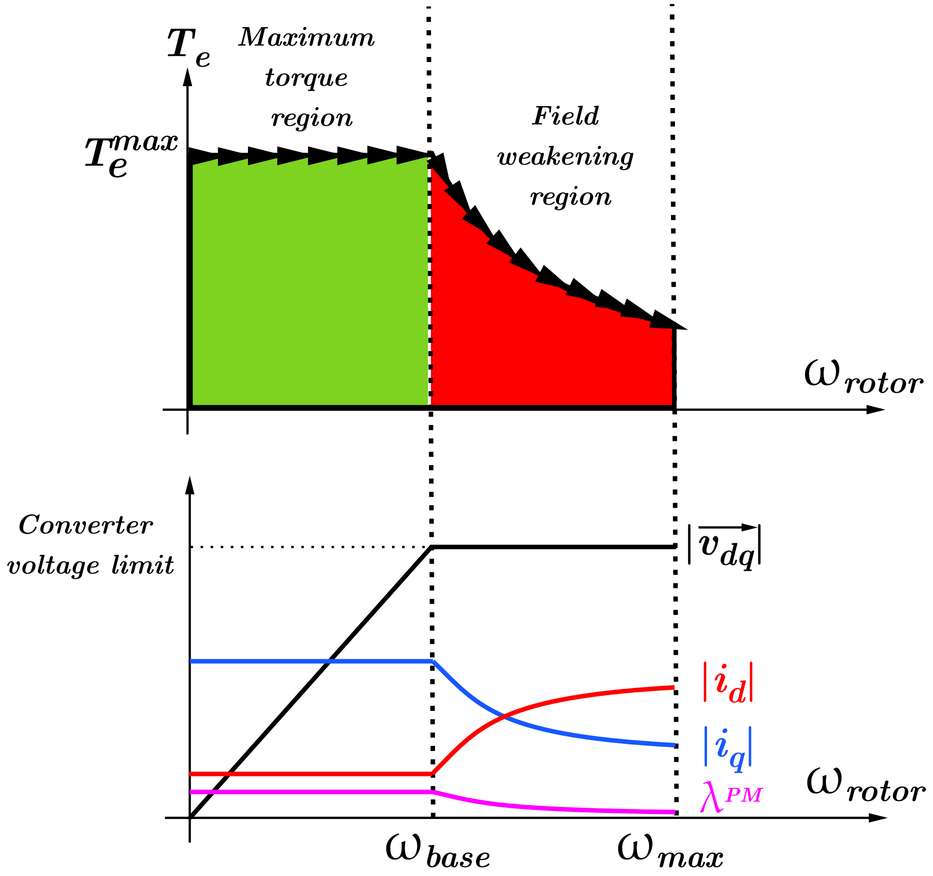

Figure 3-4: Machine operation regions

capabilities [22][10], allowing maximum torque to be produced. As speed reaches value w_{base}, induced voltage equals converter limit. In order to further increase speed, flux magnitude must decrease. For induction machines, separately-excited DC machines, and wound-rotor synchronous machines, flux can be directly modified with field current [22][23]. On the contrary, flux is generated by a permanent magnet in PMSMs, and thus can not be directly controlled. To reduce rotor magnet flux linkage λ_{PM}, a negative i_d current must be injected. Because current magnitude is kept constant to maintain input power, i_q current magnitude decreases, reducing output torque as shown in Fig. 3-4. Field weakening operation reduces machine efficiency since a portion of input power is dedicated to reduce magnet flux, instead of producing torque.

---

[10] This limit depends on adopted modulation strategy, it is generally restricted to $\frac{v_{dc}}{2}$ but it can be augmented to $\frac{v_{dc}}{\sqrt{3}}$ with *tripplen harmonic injection*

3.2 Variable-Flux machines operation

Variable-Flux PMSMs (VF-PMSM) are proposed to solve the adverse effects of field weakening operation in permanent magnet machines. This achievement will be explained in the present section.

First consideration is the definition of two separated zones for magnetic characteristic of magnetic materials. This zones are usually denoted as recoil and droop, each of them being characterised by their magnetic permeability, μ_r and μ_{droop} respectively. When joined toghether, it is said that the material is represented by means of a bilinear approximation.

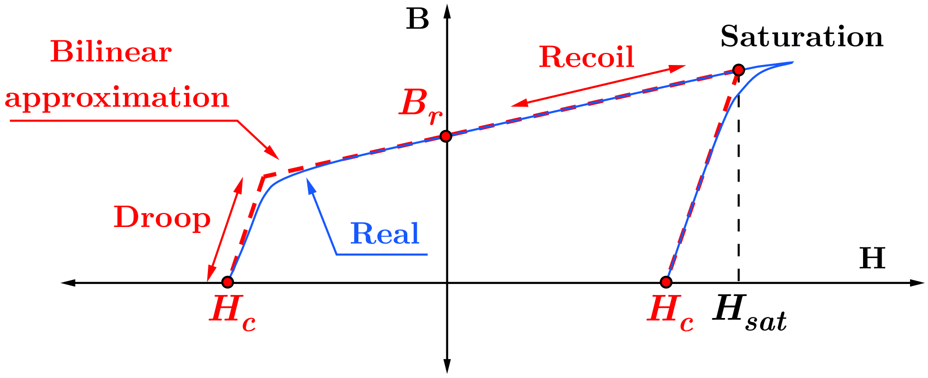

Figure 3-5: Real and bilinear characteristic of magnetic materials

After that, consider the magnetic characteristic of a hard magnetic material such as a rare-earth permanent magnet (Fig. 3-6). Since recoil permeability of rare earth magnets is almost constant, and their knee point is usually far from the origin [24], a moderate and continuous i_d current must be injected to effectively reduce magnet flux linkage.

Differences can be appreciated in Fig. 3-7, in which a high-coercitive force magnet (rare-earth, typically NdFeB) is combined with a low-coercitive force material (AlNiCo or similar). The magnetic characteristic of the mixture will have different coercitivity and remanence than original compounds. In addition, knee point will be closer to the origin, making it attainable within converter current margins. This fact is illustrated in Fig. 3-8.

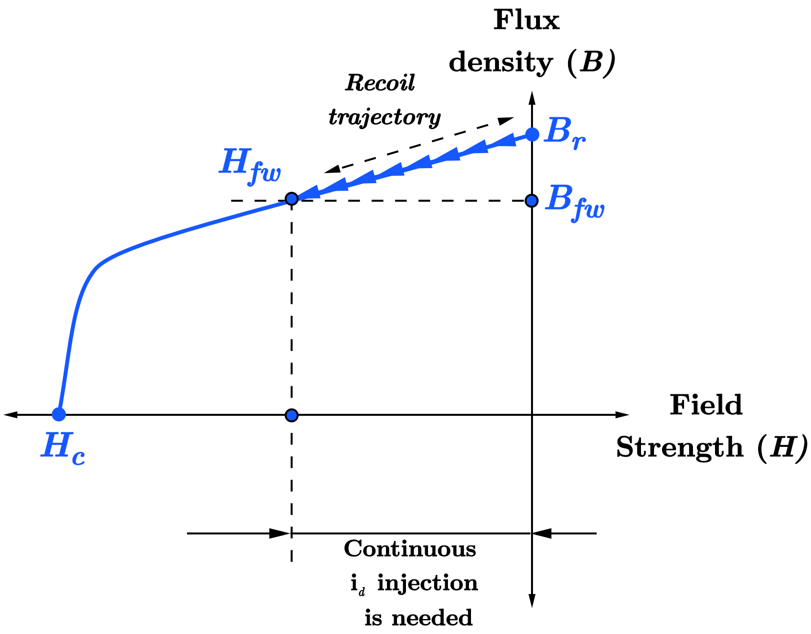

Figure 3-6: Rare-earth magnet flux linkage reduction by i_d injection

When field intensity goes beyond the knee point, the magnet will return to a lower remanence once current is removed. That is precisely the advantage of VF-PMSMs over conventional PMSMs. In this machines, a short i_d pulse can result in lower magnet flux linkage, without the need for field weakening operation to be maintained. This feature is typically exploited in high speed operation, where induced voltage may reach converter limits, and torque requirements are low. When high torque is required again, the magnets can be remagnetized with a positive i_d current pulse, following the characteristics shown in Fig. 3-9.

However this principle may be a source of trouble under high loading conditions. Since magnets are easily demagnetized, flux barriers are usually introduced in VF-PMSM designs. This is meant to prevent flux lines from the q axis to pass through the magnets as iron gets saturated. Additionally, this feature provides the machine with larger reluctance torque, as inductance difference between d amd q axis increases. The situation is depicted in Fig. 3-10.

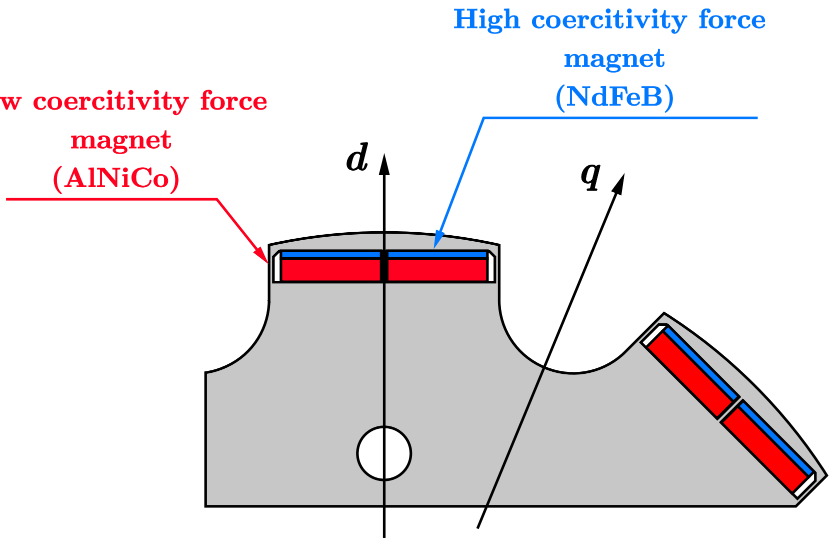

Figure 3-7: Magnets arrangement in VFPMSM

3.3 Loss production and efficiency

Present section is meant to explain main sources of power loss in electrical machines. The understanding of this phenomena is important not only when designing but also when modelling electrical machines. In fact, developed expressions will be used in further sections of the document.

3.3.1 Copper losses

Since most conductors in rotating machines are made of copper, their associated loss is typically referred to as copper loss. Copper loss can be dominant in some cases [17][25], and may be divided in two main components: DC and AC.

DC losses (P_{Cu}^{DC}) depend on winding DC resistance R_{DC} and RMS circulating current i as given by the following equation:

$$P_{Cu}^{DC} = i^2 \cdot R_{DC} \tag{3.15}$$

Where R_{DC} can be computed for a given conductor as:

$$R_{DC} = \frac{l}{\sigma \cdot A} \tag{3.16}$$

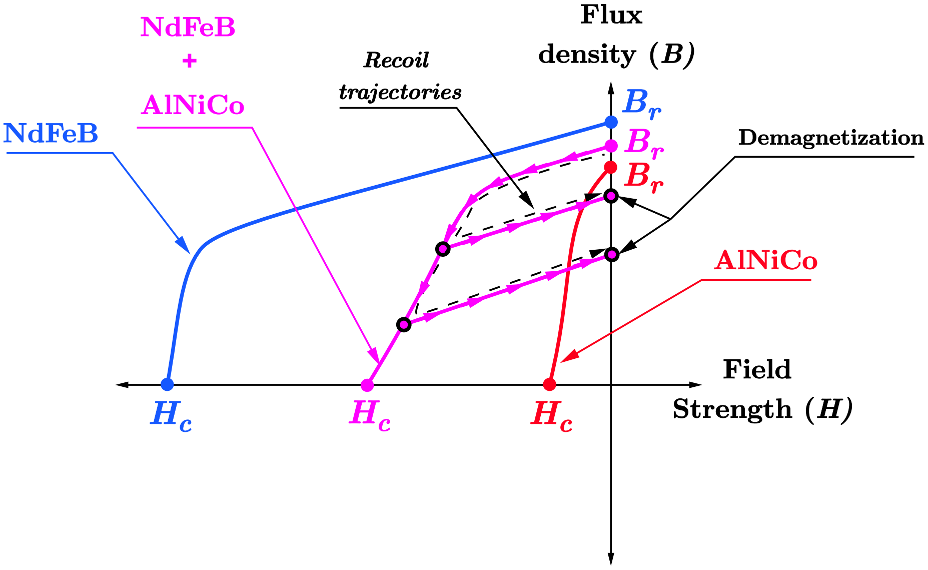

Figure 3-8: Demagnetization of combined permanent magnets

In the expression, l stands for conductor length, σ represents material conductivity, and A denotes cross sectional area. DC Copper losses are known to be highly temperature-dependent. In the design stage, operating temperature must be taken into account in order to define winding DC resistances. This is so because temperature influences DC resistance as given by (3.17).

$$R_{DC}(T) = R_{DC0} \cdot [1 + \alpha(T - T_0)] \tag{3.17}$$

Where R_{DC0} stands for initial resistance at any temperature T_0, and α represents thermal resistance variation coefficient.

Next family of losses is AC losses. Physical phenomena like skin or proximity effects will lead to an increase in effective resistance as frequency rises. In other words, two equal-amplitude but different frequency circulating currents will result in differing losses, with the higher frequency example producing larger losses. The relative importance of these phenomena is dependent on winding configuration and machine design, but literature suggests that skin effect is dominant for most frequencies and windings [26][27][28]. Consequently, an analytical model for skin effect-caused AC loss increase will be derived.

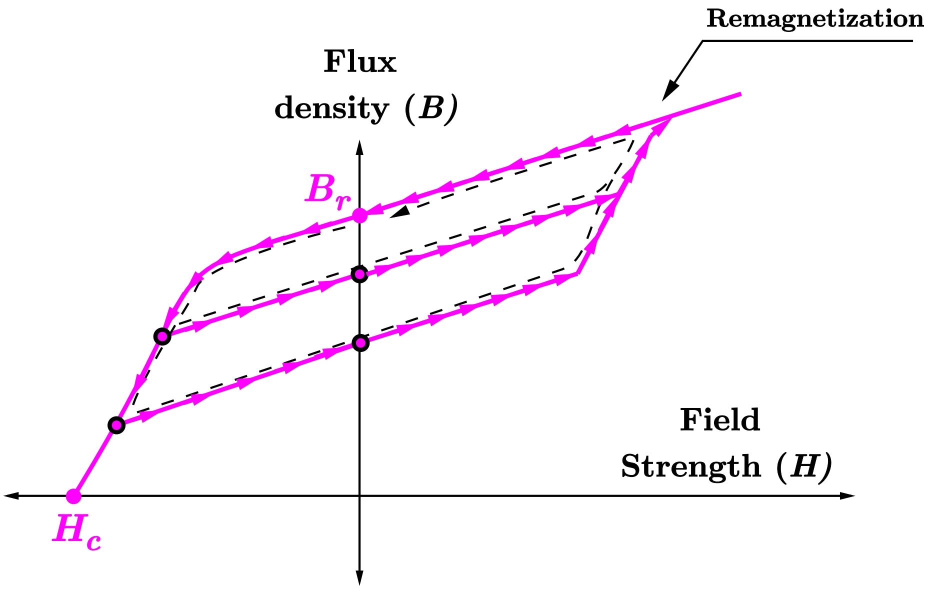

Figure 3-9: Remagnetization process

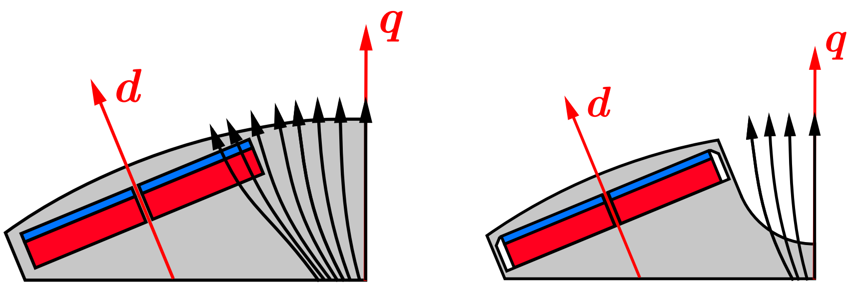

(a) No flux barrier (b) Flux barrier

Figure 3-10: Load current influence in magnetization state prevention

Consider the rectangular copper conductor shown in Fig. 3-11, placed inside a ferromagnetic material that covers three of its outer faces. A current vector $\vec{i}$ is circulating through it, causing field intensity $\vec{H}$ to be created.

Considering the ferromagnetic material permeability to be infinitely larger than that of copper or air (which are fairly similar), more flux lines will be created at the lower part of the conductor (closer to the ferromagnetic material). It will cause the impedance to be increased locally at the bottom of the conductor, modifying current density ($\vec{J}$) distribution. Let us develop an analytical expression for this current density variation among conductor height. For the derivation, consider paths formed by points 1 to 8, both of height equal to dy.

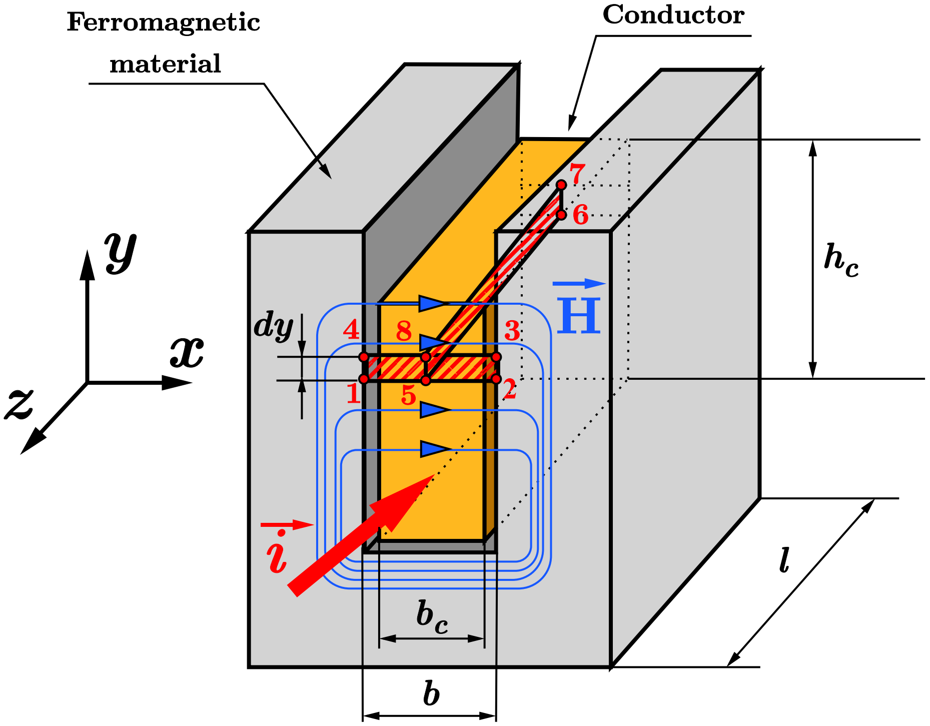

Figure 3-11: AC Currents in a conductor

From the figure, in which conductor height is denoted by h_c, conductor width is denoted by b_c, and slot width is represented by b, generalized Ampere's Law can be applied to closed path 1-2-3-4-1 in the figure.

As the ferromagnetic material is assumed infinite in permeability, $\vec{H}$ only component is located in the x axis with the figure convention, thus yielding [17]:

$$\begin{gathered}\oint \vec{H} \cdot \vec{dl} = \iint_S \vec{J}\, dS \\ H \cdot b - \left(H + \frac{\partial H}{\partial y} dy \right) \cdot b = J \cdot b_c \cdot dy\end{gathered} \tag{3.18}$$

From the above equation, partial derivative of field intensity with respect height is obtained as:

$$-\frac{\partial H}{\partial y} = \frac{b_c}{b} \cdot J \tag{3.19}$$

Next, Faraday's induction law can be applied at closed path 5-6-7-8-5 in the figure, (4.2) being obtained. In the equation, vector E denotes electric field.

$$\begin{aligned} \oint \vec{E} \cdot \vec{dl} &= \frac{\partial}{\partial t} \iint\limits_S \vec{B}\, dS \\ -E \cdot l + \left(E + \frac{\partial E}{\partial y} dy\right) &= \frac{\partial}{\partial t} \iint\limits_S \vec{B}\, dS \end{aligned} \tag{3.20}$$

From which:

$$\frac{\partial E}{\partial y} = \frac{\partial B}{\partial t} = -\mu_0 \frac{\partial H}{\partial t} \tag{3.21}$$

If this last equation is combined with generalised Ohm's law (in which σ_c stands for conductor conductivity):

$$\vec{J} = \sigma_c \cdot \vec{E} \tag{3.22}$$

The following three identities in phasor form can be obtained, where μ_0 denotes vaccuum permeability, j stands for the imaginary unit and ω is AC current angular frequency.

$$\begin{cases} -\dfrac{\partial \underline{H}}{\partial y} = \dfrac{b_c}{b} \underline{J} \\ -\dfrac{\partial \underline{E}}{\partial y} = -j\omega\mu_0 \underline{H} \\ -\dfrac{\partial \underline{J}}{\partial y} = -j\omega\mu_0\sigma_c \underline{H} \end{cases} \tag{3.23}$$

If last equation is differentiated with respect height y and combined with top equation, current density differential equation for height is obtained as:

$$\frac{\partial^2 \underline{J}}{\partial y^2} - j\omega\mu_0\sigma_c \frac{b_c}{b} \underline{J} = 0 \tag{3.24}$$

The equation has a solution of the form:

$$\underline{J} = C_1 \cdot e^{(1+j)\cdot\alpha y} + C_2 \cdot e^{-(1+j)\cdot\alpha y} \tag{3.25}$$

Where α is the inverse of the so called *skin depth*[11], its value being given by:

$$\alpha = \sqrt{\frac{\omega \sigma_c b_c}{2b}} \tag{3.26}$$

This constant has units of m^{-1} and can be turned to dimensionless if multiplied by conductor height:

$$\xi = \alpha h_c = h_c \sqrt{\frac{1}{2} \omega \mu_0 \sigma_c \frac{b_c}{b}} \tag{3.27}$$

Constants C_1 and C_2 can be computed with appropriate boundary conditions to be equal to:

$$C_1 = C_2 = \frac{j \omega \mu_0 \sigma_c}{(1+j) b \alpha \left(e^{(1+j)\alpha h_c} - e^{-(1+j)\alpha h_c} \right)} \tag{3.28}$$

Once current density as a function of height is known, losses can be integrated for the entire conductor as:

$$P_{AC} = \int_0^{h_c} = (J \cdot b_c \; dy)^2 \cdot \frac{1}{\sigma b_c dy} = \frac{b_c \cdot l}{\sigma_c} \int_0^{h_c} J^2 dy \tag{3.29}$$

The factor by which DC losses have to be multiplied in order to represent AC losses increase is then equal to:

$$k_R = \frac{R_{AC}}{R_{DC}} = \frac{b_c^2}{I^2} \int_0^{h_c} \underline{JJ^*} dy \tag{3.30}$$

Which can be approximated to multiple circular conductors inside the slot to yield [17]:

$$k_R \approx 1 + 0.59 \frac{z_t^2 - 0.2}{9} \cdot \xi^4 \tag{3.31}$$

In the equation, z_t stands for conductor layers. The above equation will be used through the thesis to approximate the effect of AC losses inside machine windings.

---

[11] Skin depth is usually considered as the distance from conductor surface, at which current is still circulating

3.3.2 Iron losses

Alternating magnetic fields in electrical machines are also a source of losses in its magnetic cores. Similar to winding resistive losses, which are referred to as copper losses because of its composition, magnetic core losses are typically denoted as iron losses.

Machine magnetic circuit is subject to two families of losses: hysteresis losses and eddy current losses. First kind is related to the magnetic nature of the medium, and can be described by means of material B-H characteristic. Eddy current loss is explained by parasitic currents being induced in the cores. Therefore, this loss is related with core dimensions and electrical parameters.

Hysteresis loss can be addressed by considering a magnetizing curve like the one shown in Fig. 3-12. As seen in 3-12a, when the material is first magnetized, field intensity will go from H_1 to H_2. Following the material B-H characteristic, positive energy per unite of volume is being given to the magnetic system, as field density increases from B_1 to B_2. This energy, with the notation of the figure, can be computed as [17]:

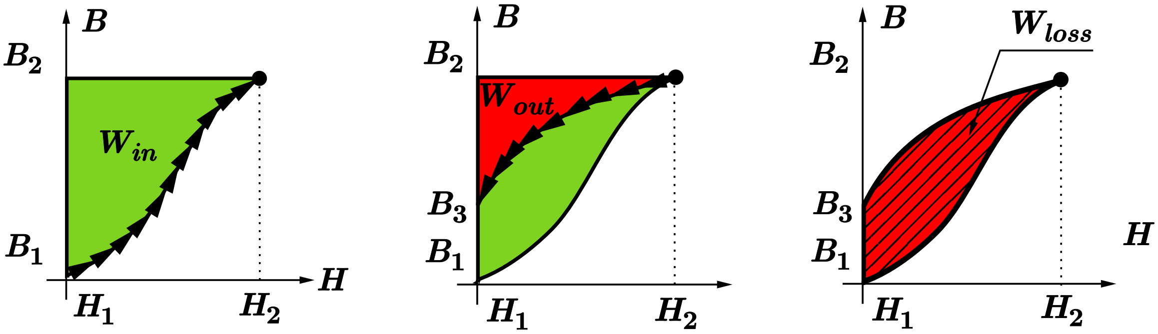

(a) Field is applied (b) Field is removed (c) Energy is lost

Figure 3-12: Energy loss process due to hysteresis

$$W_{in} = \int_{B_1}^{B_2} H dB \tag{3.32}$$

Once external field is removed, flux density evolves from B_2 to B_3 due to its hysteretic nature. Contrary to the magnetization process, energy per unit of volume is being returned by the magnetic system as given by:

$$W_{out} = \int_{B_2}^{B_3} HdB \tag{3.33}$$

On aggregate, hysteresis loss is computed as a line integral. Note that the obtained energy is expressed in units of volume, to obtain total energy, multiply by volume V.

$$W_{hys} = V \cdot \oint HdB \tag{3.34}$$

For alternating quantities, power may be obtained as the product of energy and frequency, this being the reason why hysteresis losses are considered to vary linearly with frequency:

$$P_{hys} = f \cdot W_{hys} \tag{3.35}$$

Empirical expressions are typically used to approximate this phenomena. An example is provided in (3.36), where η and n are material constants, and B_{max} stands for flux amplitude.

$$P_{hys} \approx f \cdot \eta \cdot B_{max}^{n} \cdot V \tag{3.36}$$

On the other hand, eddy currents are the result of induced voltages in the cores due to Faraday's Law. These voltages will create currents that will oppose changes in the flux. This effect can become dominant in solid objects, leading to machine cores being thinly laminated. To provide a physical explanation, consider the solid core in Fig. 3-13. In the core, of width w, height h, and lamination thickness d, an alternating flux $B = B_{max} \cdot \sin(\omega t)$ is passing perpendicular to its surface.

Maximum flux in an arbitrary rectangular region of width x will then be equal to:

$$\phi = 2h \cdot x \cdot B_{max} \tag{3.37}$$

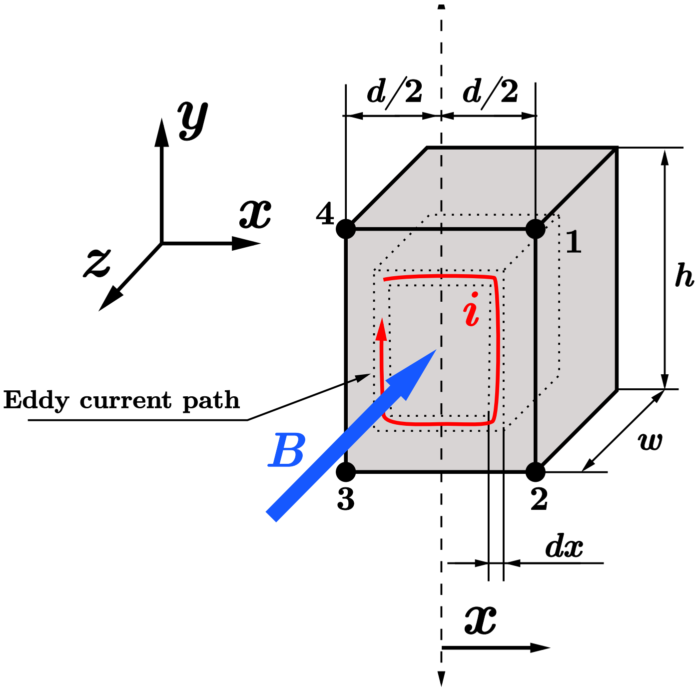

Figure 3-13: Solid ferromagnetic core subject to alternating flux B

According to Faraday's Law, when region width d is significantly lower compared to height, induced RMS voltage is equal to:

$$E = 2hx\frac{\omega B_{max}}{\sqrt{2}} \tag{3.38}$$

Next, resistance of the path must be computed. If lamination thickness d is negligible with respect height h, it can be approximated to:

$$R = \rho\frac{l}{s} \approx \frac{2h\rho}{wdx} \tag{3.39}$$

In which l stands for the length of the path for the circulating eddy current. Joining last two expressions, an equation for a differential circulating current is obtained:

$$dI = \frac{2\pi f B_{max} wx \cdot dx}{\sqrt{2}\rho} \tag{3.40}$$

Differential power loss is obtained from multiplying current and voltage:

$$dP_{eddy} = E \cdot dI = \frac{(2\pi f B_{max})^2 \cdot whx^2}{\rho} dx \tag{3.41}$$

Then, integrating in the positive current direction, total loss is obtained:

$$P_{eddy} = \int_0^{\frac{d}{2}} dP_{eddy} = \frac{(2\pi f B_{max})^2}{\rho} wh \int_0^{\frac{d}{2}} x^2 dx \tag{3.42}$$

Since core volume is equal to, $V = whd$, the integral becomes [17]:

$$P_{eddy} = \frac{V \cdot (\pi f B_{max} d)^2}{6\rho} \tag{3.43}$$

Main conclusion to be extracted from the expression is frequency quadratic dependency, and lamination thickness cubic dependency. The analytical expression may differ from experimental results, causing empirical polynomials to be developed.

In most analytical approaches, both hysteresis and eddy current loss components are joined together, to form expressions of the type:

$$P_{Fe} = \underbrace{k_h \cdot B^{\gamma} \cdot f^{\alpha}}_{\textbf{Hysteresis}} + \underbrace{k_e \cdot B^{\theta} \cdot f^{\beta}}_{\textbf{Eddy currents}} \tag{3.44}$$

Where k_h and k_e are material constants, as well as γ, α, θ, β [29]. Exponents α and β are commonly chosen as 1 and 2 respectively, based in previous analytical considerations. However, this may not be accurate enough in some cases. To adapt these dependencies to discrete calculations such as finite-element analysis (FEA) software, material manufacturers offer loss density tables as a function of flux and frequency (shown conceptually in Fig. 3-14). It is convenient to express these dependencies as volume-independent in order to ease its implementation in FEA software.

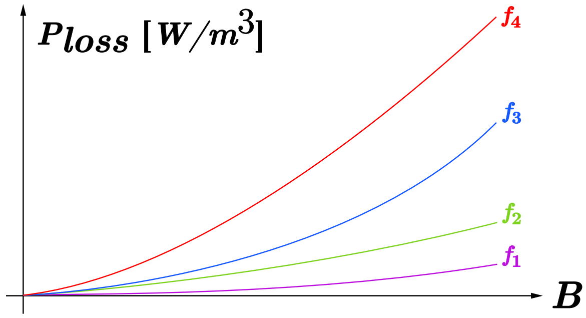

Figure 3-14: Typical loss specific coefficients as a function of flux and frequency

3.4 Optimized design algorithms

Optimization is a widely utilized concept in contemporary electrical machine design. The aim of the optimization process is typically related to enhancing performance, extending lifespan, or reducing cost. Given that electrical machines are fundamental components in the industrial world, maximizing their performance is often a primary focus [30]. Recent advancements and trends in mathematical tools, linked to enhanced computer simulation capabilities, have facilitated the integration of optimization techniques into the design of electrical machines [31].

Two families of optimization techniques can be distinguished:

- Parametric optimization
- Topology optimization

In parametric optimization, design variables (rotor radius, tooth width, skew angle, nominal current...) are specified, and an algorithm explores a large number of possible values and combinations for each of the parameters. Objective functions will be evaluated for each of the possibilities and the designer will select optimum cases based on application requirements [32]. Therefore, this technique imposes a parametric definition of some design variables. Fig. 3-15 depicts this reasoning with an example in which magnet length is optimized following this approach. Parametric optimization has the advantage of being simple and reliable. However, obtained shapes can only be as complex as the designer experience allows to.

Machine topology is fixed, and the designer must be able to select most adequate variables to be modified.

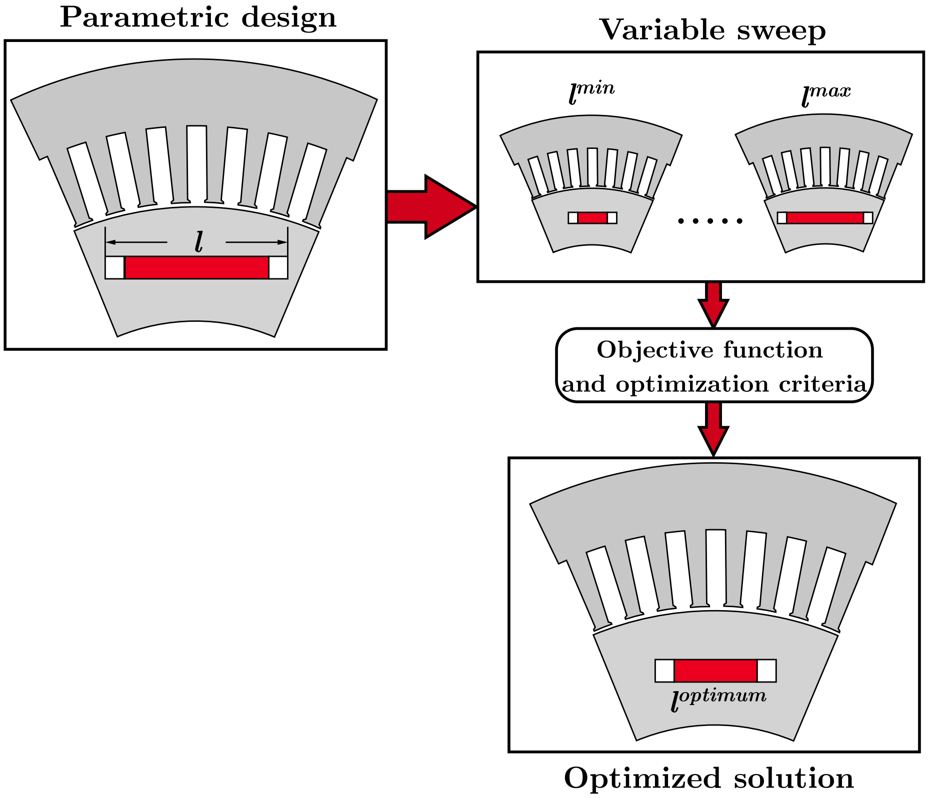

Figure 3-15: Parametric optimization workflow

On the other hand, topology optimization works differently, allowing for complex geometries to be obtained. Instead of changing previously defined parameters (related or not to machine geometry), the algorithm decides best material for every machine element[12]. This is considered as a change in machine topology rather than just geometry, since optimal design may be significantly different from the initial case. Fig. 3-16 provides an example for this reasoning. In the image, some parts of the machine are enclosed within a design region, then, an algorithm will alter the material composition inside that enclosure. Typically, the method is configured to decide between two materials for every element (iron and air in the figure), similar to parametric approach, simulating a large number of cases helps reaching an optimum solution.

---

[12] Both parametric and topology optimization methods are implemented in FEA software, in which an element stands for a mesh element inside the model.

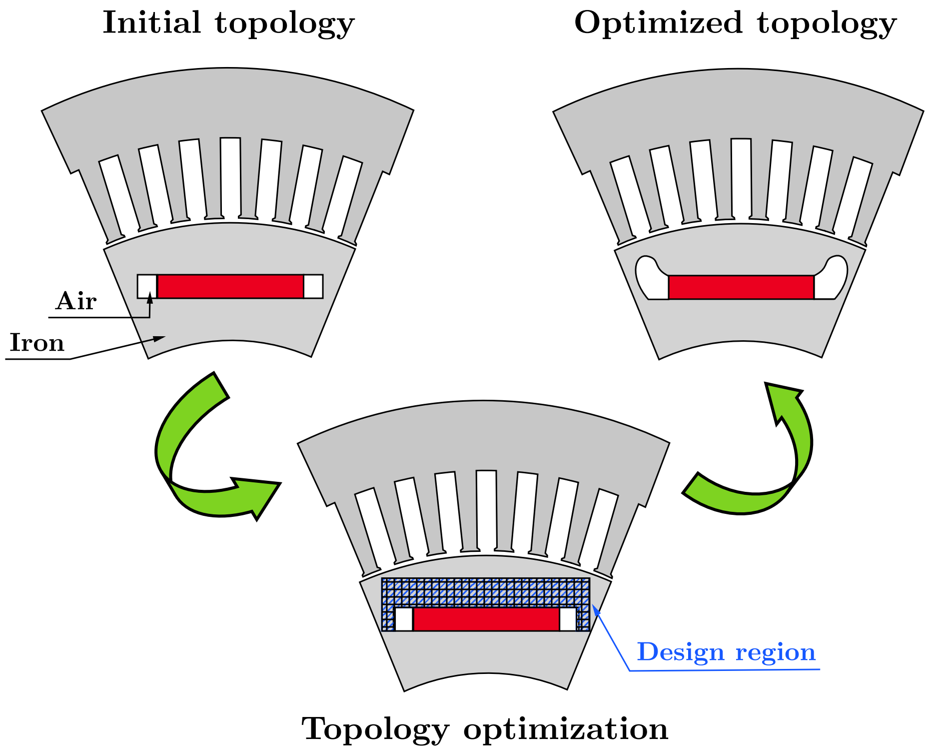

Figure 3-16: Topology optimization workflow

Main concern with this algorithm is related with solution feasibility in mechanical terms. Even if optimum, obtained topology may be impossible to manufacture or inconsistent with mechanical constraints. To solve this issue, *Normalized Gaussian Network* approach is proposed [31]. This method ensures obtained solutions to be smooth and feasible to manufacture, its fundamentals will be explained with the aid of Fig. 3-17. Consider a rotor slot with two magnets, made of materials A and B respectively, and modelled by a finite-element mesh. Since both magnets are included in the design region, the algorithm has to choose optimum material for each of their elements. To do this, several Gaussian distributions with center located at points (μ_x, μ_y) and standard deviation σ are placed within the region. Any Gaussian distribution G_k can thus be described in the xy plane as follows:

$$G_k(x, y) = \frac{1}{2\pi\sigma^2} e^{\frac{(x-\mu_x)^2+(y-\mu_y)^2}{2\sigma^2}} \tag{3.45}$$

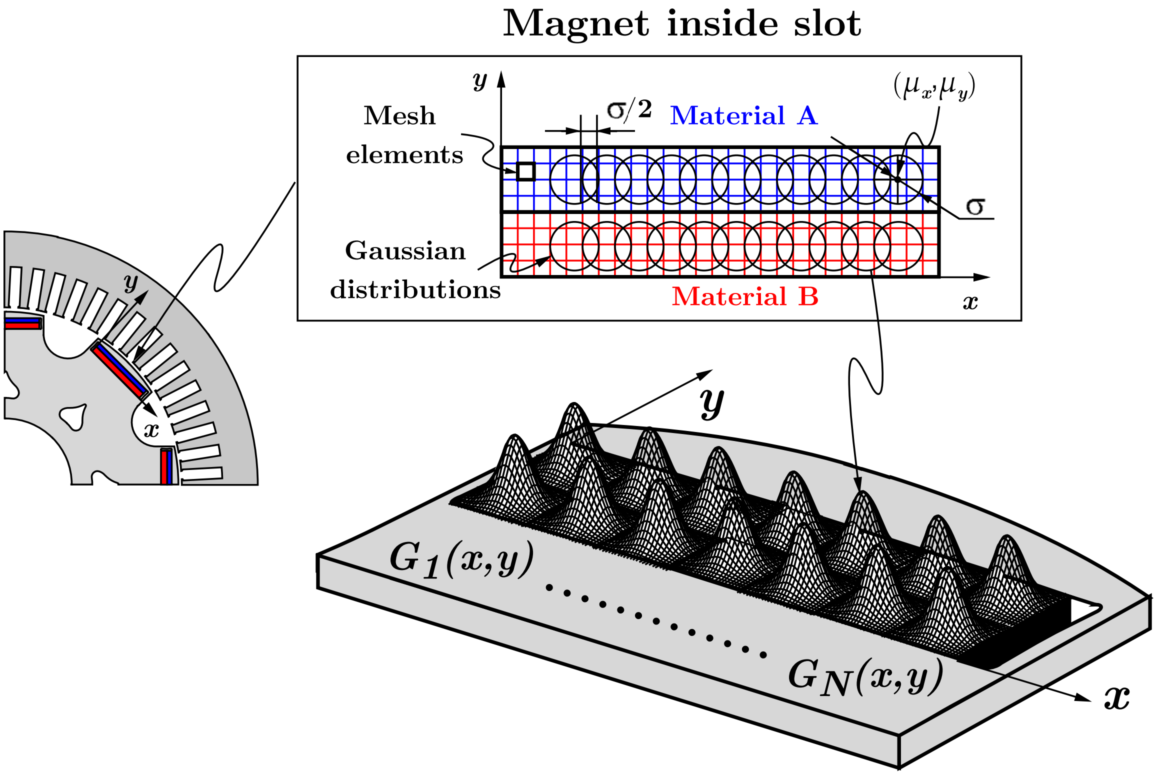

Figure 3-17: Topology optimization using Normalized Gaussian Network (NGNet)

The algorithm will normalize each of this distributions as given by (3.46), in which N stands for total number of distributions inside the region.

$$\|G_k\| = \frac{G_k}{\sum_{i=1}^{N} G_i} \tag{3.46}$$

This information is merged to develop the status function $S(x, y)$, defined for every (x, y) element as follows:

$$S(x, y) = \sum_{k=1}^{N} w_i \cdot \|G_i\| \tag{3.47}$$

In the expression, w_i denotes the weight vector. Status function determines the state of an element located at (x, y) as explained in (3.48)

$$\begin{cases} S(x, y) > 0 \Rightarrow \text{Material A} \\ S(x, y) < 0 \Rightarrow \text{Material B} \end{cases} \tag{3.48}$$

Usage of Gaussian distributions reduces the significance of points as they move from the center of the bell, promoting the creation of smooth and feasible shapes. The algorithm will iterate over weight vector w_i in order to find best material for each element. Fitness of a weight vector belonging to iteration k (w_k) is be evaluated according to:

$$f_k = \sum_{j}^{N_{obj}} f_j^{obj}(w_k) \cdot p_j \tag{3.49}$$

Where N_{obj} denotes number of objective functions and p_j stands for relative weight of objective function f_j^{obj} within the global optimization process.

Finally, topology optimization can also rely on genetic algorithms in order to shift from one iteration to another. Fig. 3-18 contains a summarised scheme on this family of algorithms. As depicted in the image, an initial population of solutions is generated (typically in a random manner). Each element is evaluated according to (3.49) and best cases are used to generate *children* solutions. Next generation is composed by best children and best solutions from previous population.

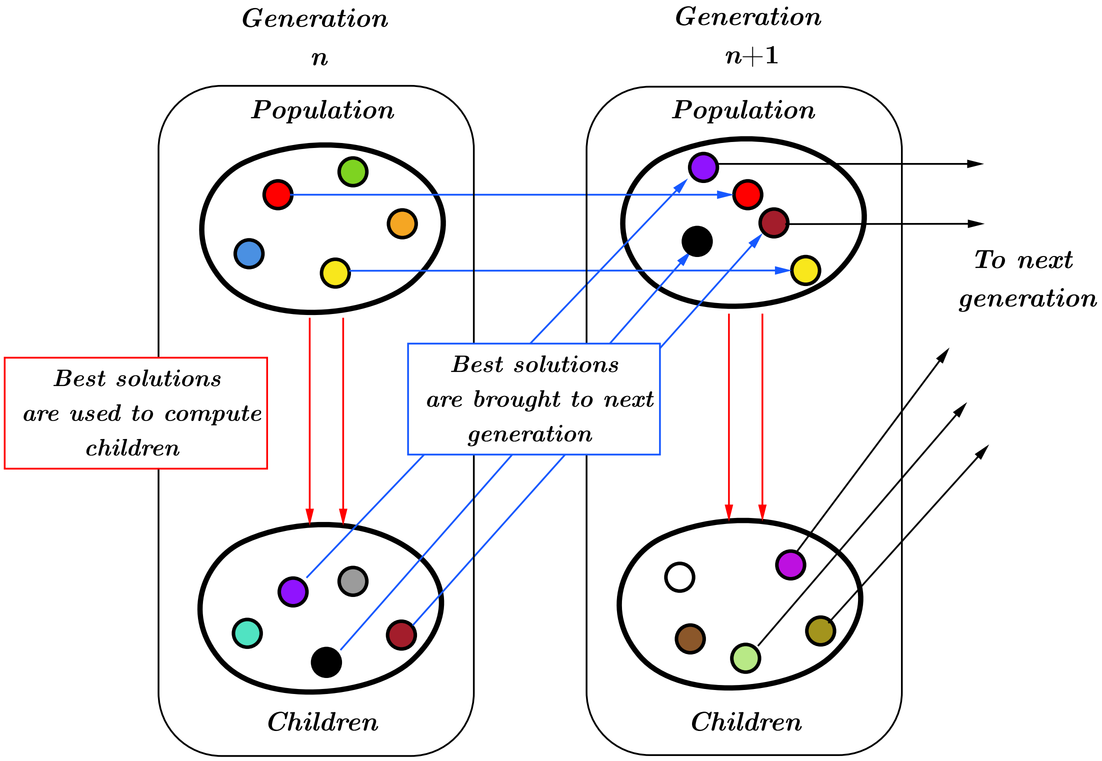

Figure 3-18: Conceptual scheme of genetic optimization algorithms

Chapter 4

Experimental results

Following chapter will cover the developed work towards the objectives that were stated in Chapter 2. More specifically, it will go through experimentally obtained results, with its appropiated explanation.

4.1 Iron loss estimation capabilities

Following section is meant to get a closer look at FEA iron loss estimation capabilities, since discrepancies among FEA and experimental data have been widely reported in literature [29][33][34]. To address this problem, a simple experiment is carried out. Obtaining an accurate loss measurement that isolates iron contribution is hard with complicated geometries like the ones found in electrical machines. Therefore, the test is performed on a ferromagnetic toroid, due to its simple geometry. This approach has been proposed in literature to isolate iron losses [29][33].

Consider the setup in Fig. 4-1, in which two copper windings of N_{turns} are placed in a toroid of average length l and cross section A. Additionally, a resistor $R_{measure}$ is connected to one of the windings to estimate circulating current with its voltage drop[13].

---

[13] Resistance tolerance must be low for the estimation to be accurate

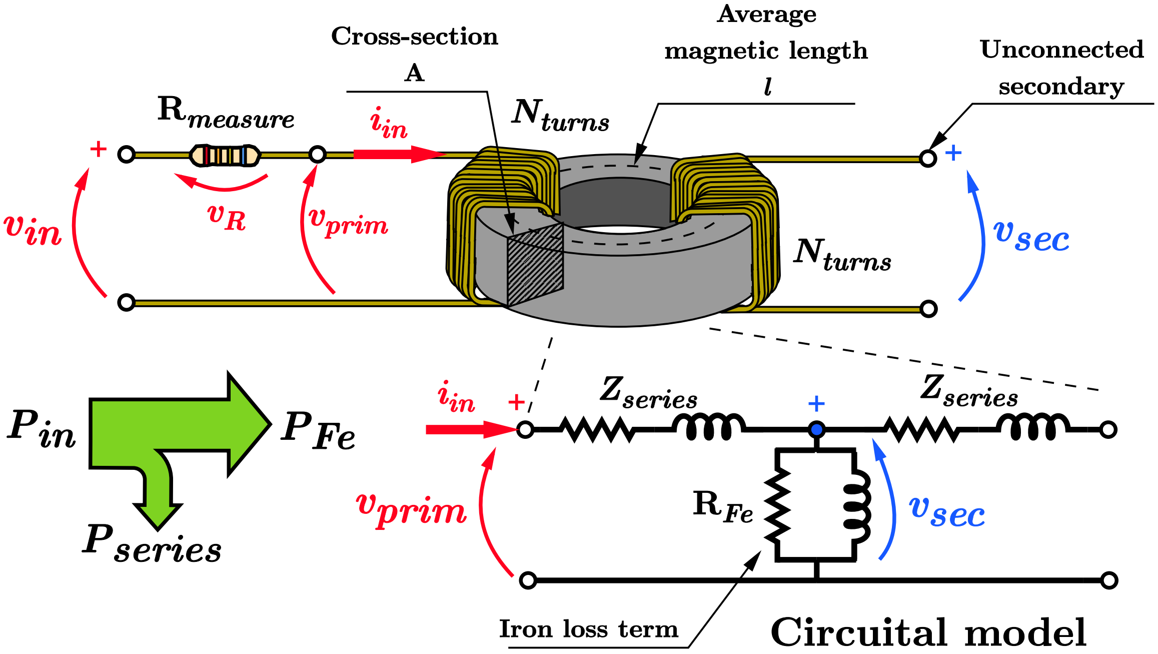

Figure 4-1: Experimental loss measurement explained

When input voltage v_{in} is fed into the primary winding, current i_{in} will circulate, creating magnetic field strength as given by Ampere's Law (4.1), in which a uniform field distribution must be assumed[14].

$$\oint_l H(t) \cdot \vec{dl} = N \cdot i_{in}(t) = H(t) \Rightarrow \frac{N \cdot i_{in}(t)}{l} \tag{4.1}$$

Field intensity in the core will translate to a magnetic flux (φ) that will link the secondary coil, thus inducing voltage (v_{sec}) according to Faraday's Law (4.2), in which B denotes flux density.

$$v_{sec}(t) = N_{turns} \frac{d\varphi(t)}{dt} = (N_{turns} \cdot A) \frac{dB(t)}{dt} \Rightarrow B(t) = \frac{1}{N_{turns} \cdot A} \cdot \int_0^t v_{sec}(t)\ dt \tag{4.2}$$

From the equations, it can be deduced that both flux density and field strength can be estimated from measuring voltage and current in the toroid. In order to decouple the influence of circuit series impedance, secondary coil is left unconnected. This assumption is based in the circuital model shown in Fig. 4-1 [35], as no current is circulating through secondary impedance (Z_{series} is of equal magnitude in both

---

[14] This is a feasible assumption due to the simplicity of the geometry

windings due to the equal number of turns), no voltage drop will be present. This enables the direct measurement of the induced voltage v_{sec} at secondary terminals.

To measure losses, note that the toroid is not providing any useful work. This implies that all its power consumption from the source is core power loss. As previously mentioned, only iron losses (P_{Fe}) are of interest in this case.

$$P_{Fe} = P_{in} - P_{series} \tag{4.3}$$

Therefore, denoting the primary current as i_{in}, it can be stated from the circuital model that:

$$P_{Fe}(t) = v_{sec}(t) \cdot i_{in}(t) \tag{4.4}$$

The test will be carried out with the aid of a signal generator, whose frequency will be varied. Averaged value of instantaneous power will be computed for an integer number of cycles to obtain iron losses. The described setup is shown in Fig. 4-2.

When the experiment is carried out at constant input voltage and increasing frequency, measured voltage and current take the shape in Fig. 4-3. Test frequencies range from 100 Hz to 5 kHz. Obtained fundamental current is recorded for every measure, results being shown in Fig. 4-4. This information will be used as an input to FEA simulations, since they are usually current-fed.

After the tests, the toroid is modelled in JMAG-Designer FEA software as shown in Fig. 4-5. Manufacturer offers a magnetic characteristic for the material that is introduced in the model. Once simulations are run, obtained flux magnitude is compared with flux estimated by (4.2) in Fig. 4-6. It can be seen in the image that the estimation accuracy decreases with frequency, going from 98.6% accuracy at 100 Hz to 85.9% at 5 kHz. This discrepancy may be explained by the frequency-dependent nature of B-H curve.

To support this hypothesis, an experimental B-H curve is derived and compared with manufacturer data. Additionally, this information can also be used to compute losses following (3.33).

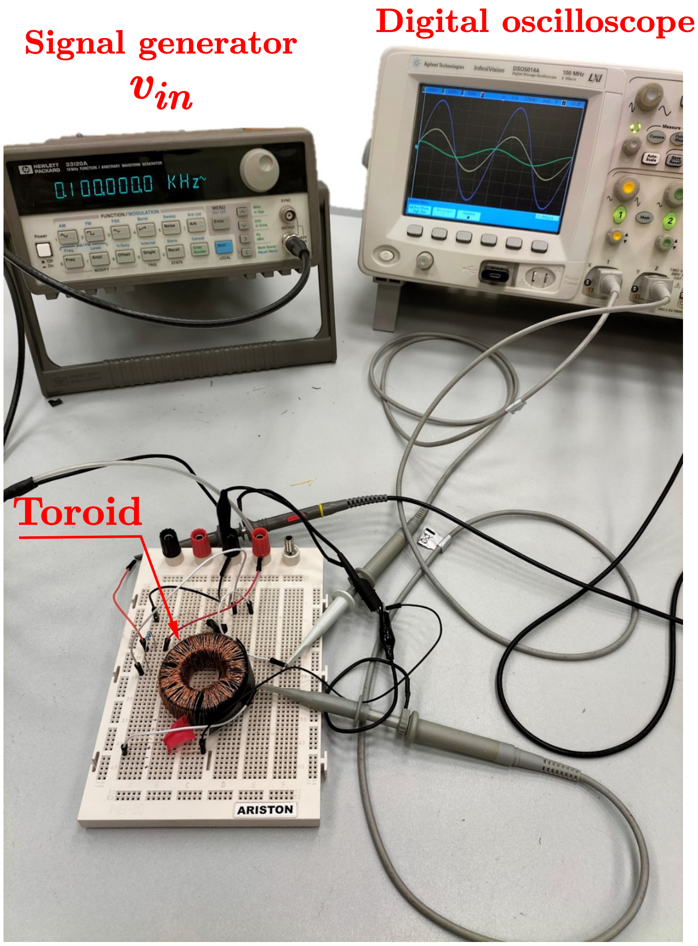

Figure 4-2: Experimental setup for toroid iron loss measurement

Fig. 4-7 shows measured B-H curve at different frequencies. In the image, solid black line represents manufacturer specified characteristic, while red area indicates the measured area for the loop trajectory. It can be seen from the image that the curve departs from manufacturer data as frequency increases. This loss in permeability can explain the discrepancy between FEA estimated flux and measured flux. Losses will be related with red area in the image, and their increasing tendency can be seen in the figure.

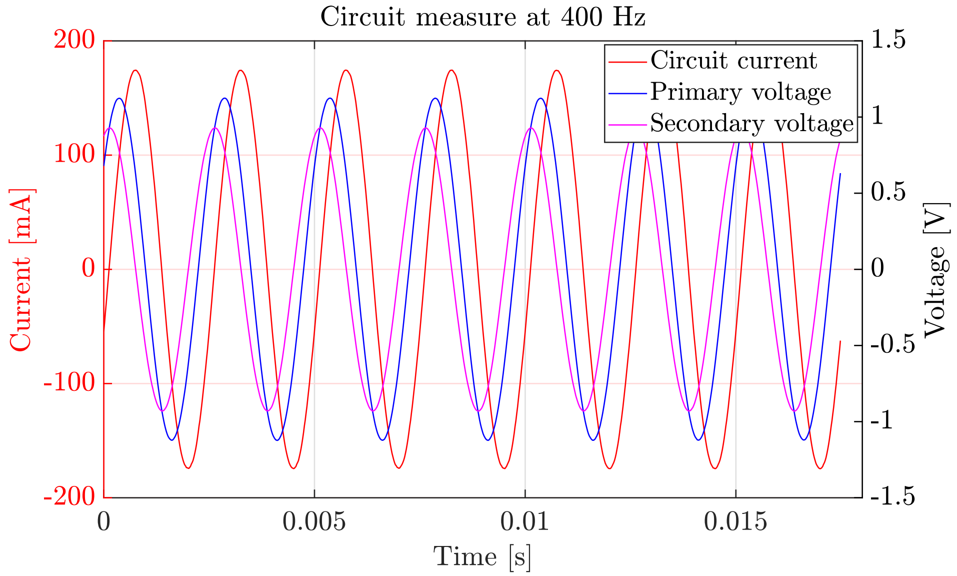

(a) V_{in}=10V 400Hz

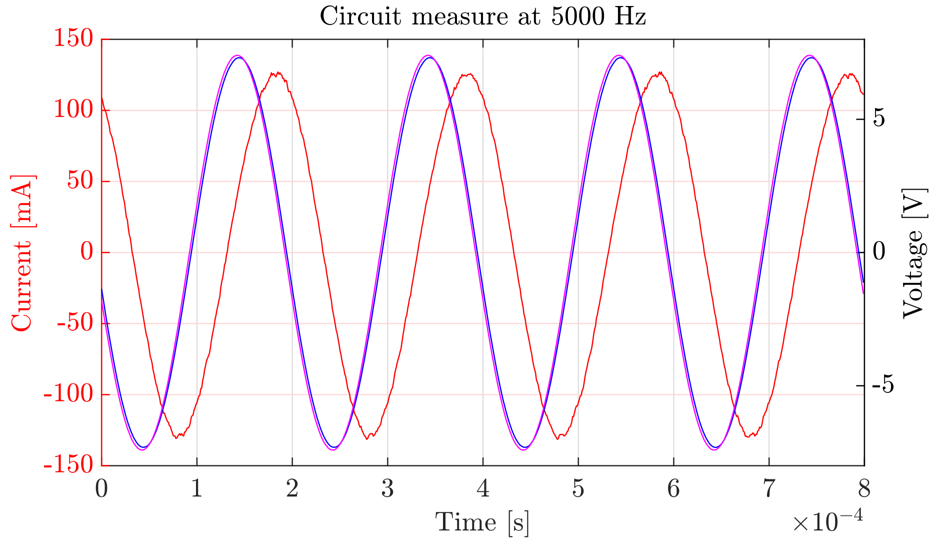

(b) V_{in}=10V 5000Hz

Figure 4-3: Circuit measure at different frequencies

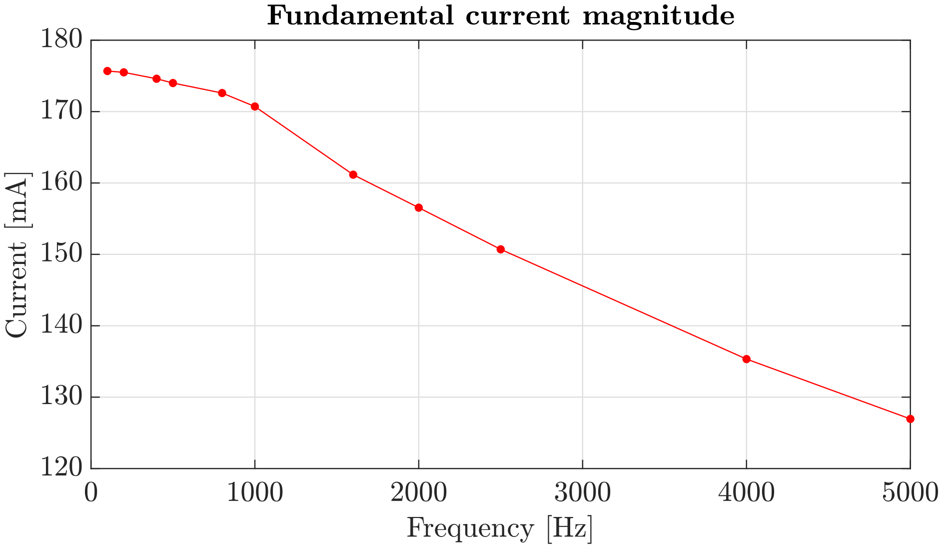

Figure 4-4: Obtained current amplitude for different frequencies

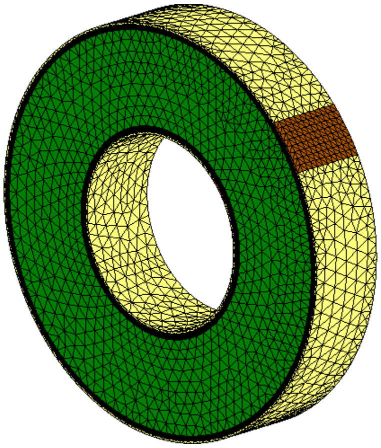

Figure 4-5: Toroid model in FEA simulation

Material magnetic characteristic is modified with frequency as shown conceptually in Fig. 4-8. This effect has been reported in literature [33] and is often attributed to eddy currents opposing flux to be created. This implies that the computation of losses could be done entirely using area inside hysteresis loops, since it would consider both hysteresis and eddy current effects at the same time.

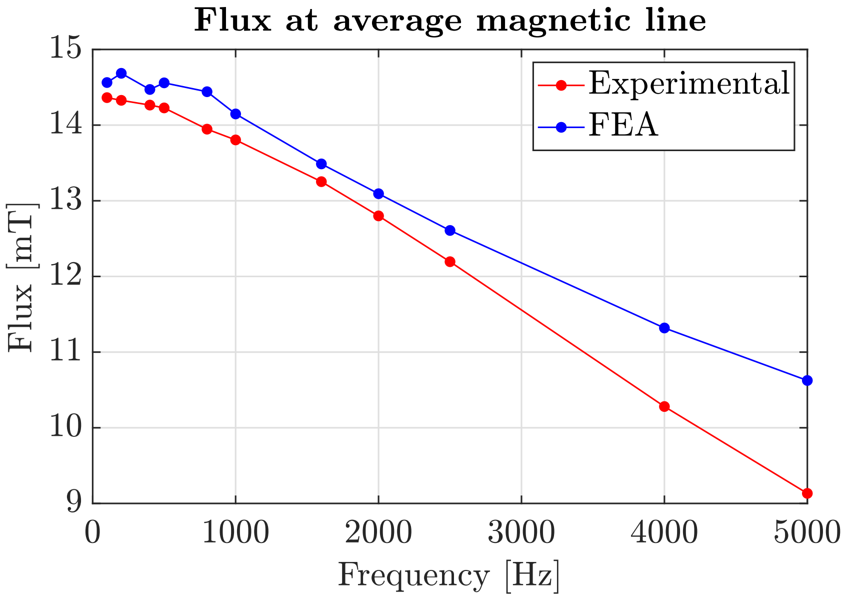

Figure 4-6: Measured and simulated flux densities for the toroid

To validate this hypothesis, several methods to estimate losses will be compared with measured values. Measured power loss is computed for each frequency of period T as follows:

$$P = \frac{1}{T} \int_0^T i_{in}(t) \cdot v_{sec}(t)\ dt \tag{4.5}$$

Losses accounting for series impedance can also be computed if primary side voltage is used instead. This procedure will also be performed on FEA obtained variables. FEA software also offers a dedicated iron loss solver based in (4.6), it will also be used for the comparison.

$$\begin{cases} P_{hys} = \displaystyle\sum_{i=1}^{n_{elem}} k_h \cdot f_{fund} \cdot |B|^{\alpha} \cdot v_i \\ P_{eddy} = \displaystyle\sum_{i=1}^{n_{elem}} \left[\sum_{k=1}^{N_{freq}} k_e \cdot f_k^2 \cdot |B|^{\beta} \right] v_i \end{cases} \tag{4.6}$$

In the estimation, v_i denotes the volume of each element in the mesh. One key consideration about the equations is the fact that hysteresis losses are only evaluated at flux fundamental frequency, while eddy current losses are added over the entire frequency spectrum. In order for this estimation to be accurate, constants k_h and k_e

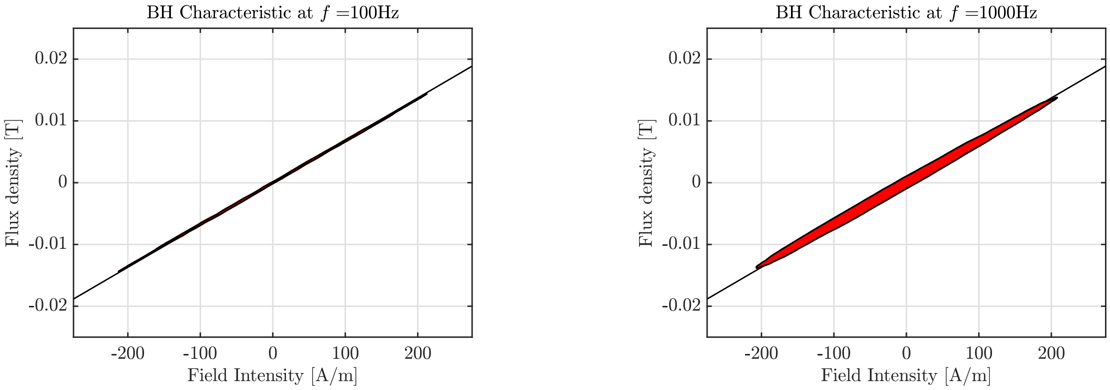

(a) V_{in}=10V 100Hz (b) V_{in}=10V 1000Hz

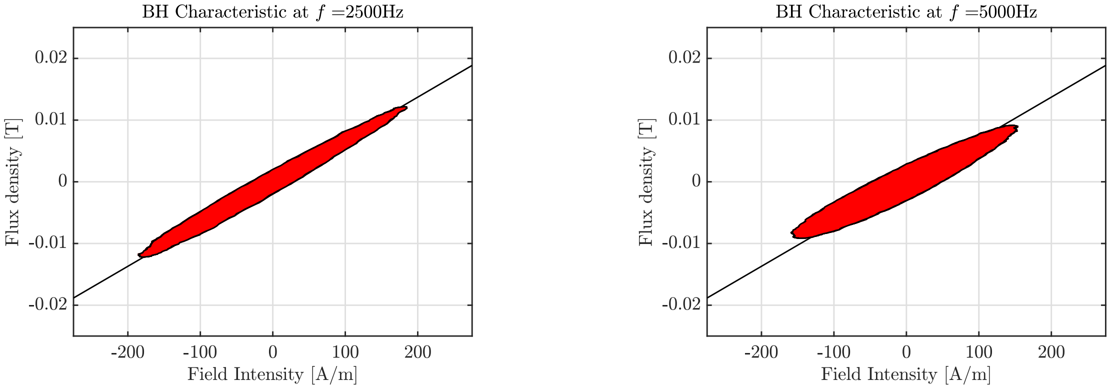

(c) V_{in}=10V 2500Hz (d) V_{in}=10V 5000Hz

Figure 4-7: Measured magnetic characteristic at different frequencies

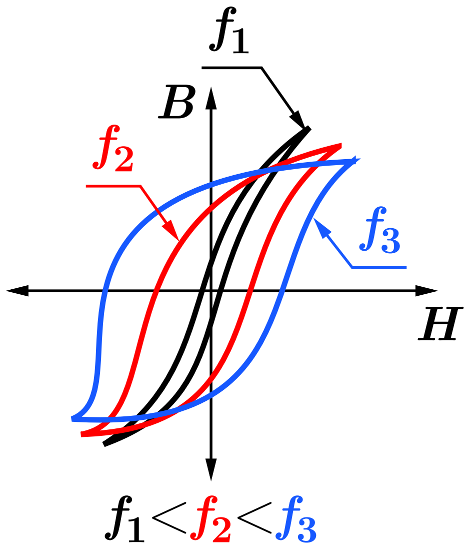

Figure 4-8: Frequency influence on material magnetic characteristic

must be obtained from experimental data. Consequently, a polynomial fit of degree 2 is computed and shown in Fig. 4-9, from which the two coefficients can be obtained.

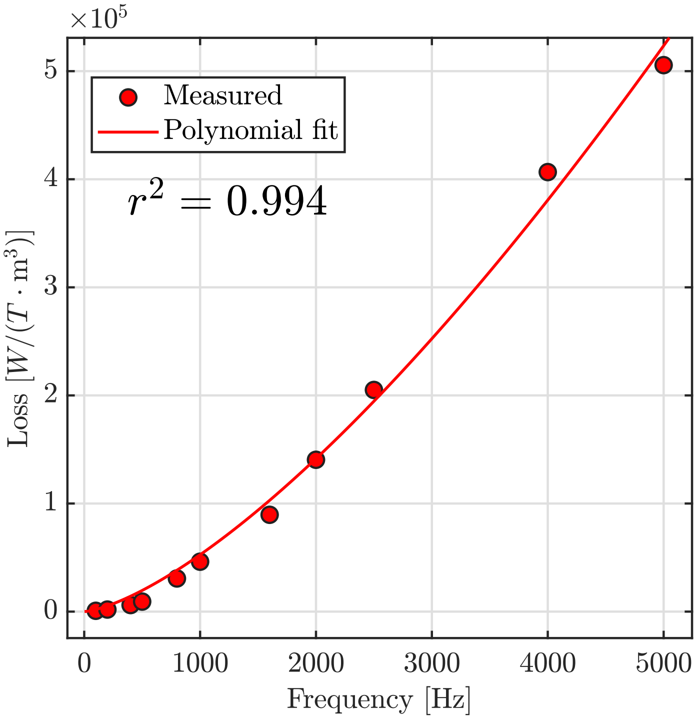

Figure 4-9: Polynomial fit on measured toroid loses

When the simulation is run, obtained power losses using different methods are shown in Fig. 4-10. From the image, it can be deduced that using FEA results to determine losses with electrical parameters as given by (4.5) is not accurate for frequencies above 800 Hz. However, dedicated FEA iron loss solver offers relatively accurate results when material experimental data is available. In order to make this results reliable, correction coefficients would be needed.

Flux estimated in Fig. 4-6 may cause the lack of accuracy of both FEA loss estimation methods. For the electrical estimation, note that induced voltages are dependent on flux (Faraday's Law), and for the dedicated solver, flux magnitude is explicitly appearing in the estimation (see (4.6)). On the other hand, the consideration of hypothesis in Fig. 4-8 yields much more accurate results. It can be seen that estimating losses with hysteresis area offers excellent results for all frequency range. As previously stated, this can be attributed to the fact that measured B-H characteristic takes into account the effects of eddy currents in the material. Therefore, curve deformation shown in Figures 4-7 and 4-8 may be responsible for both FEA inaccuracy and area-based estimation accuracy. Classical approaches shown in Section 3 compute hysteresis and eddy current losses separately. This is so because both analysis are thought for a static magnetic characteristic of the material. As a conclusion, a dynamic representation of material magnetic characteristic may result in an accurate iron loss estimation, some of them have been proposed under the name of the dynamic Jiles-Atherton model [33][34].

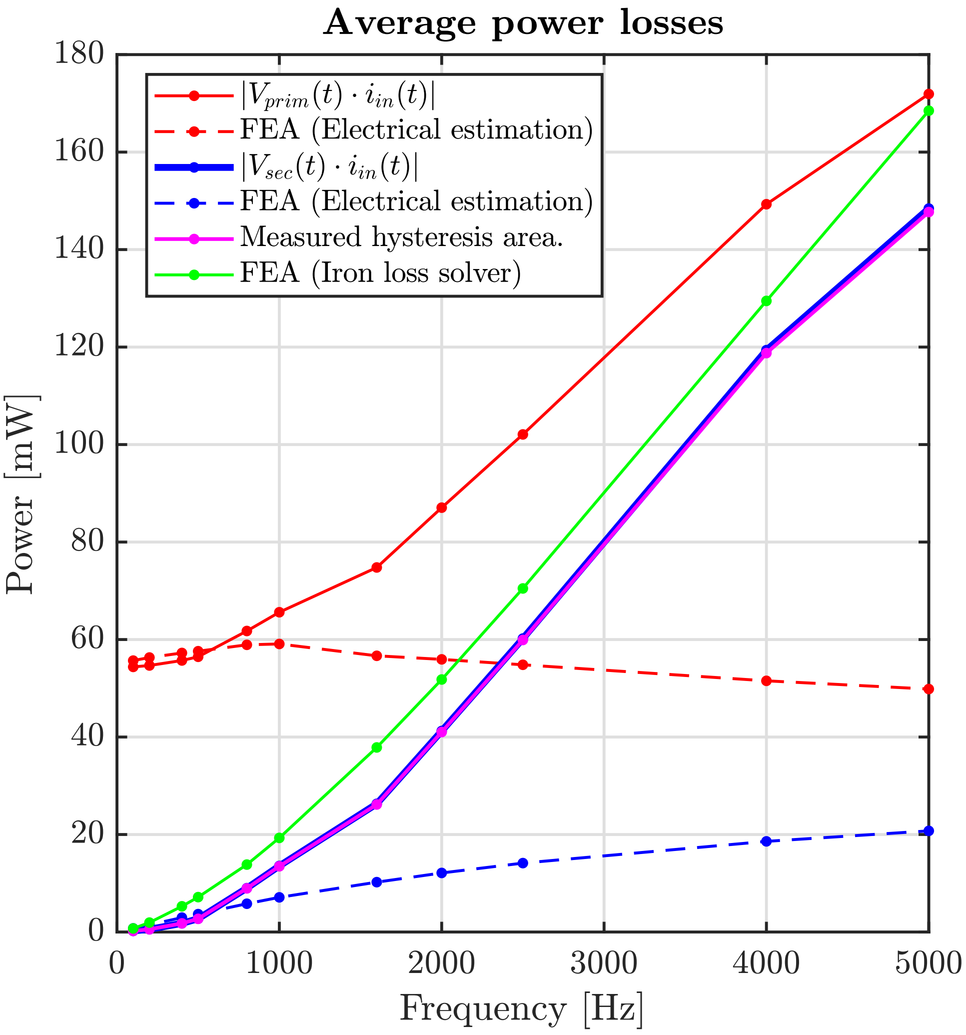

Figure 4-10: Iron loss estimation methods compared

4.2 Magnetic materials characterization

This section is dedicated to the study of magnetic characteristic for different families of permanent magnets. Goal of the section is to visualize the impact of different magnet combinations, while getting accurate information to introduce into simulation models.

As stated earlier in the document, magnets are typically characterised by means of their B-H curve. During present work, this information is obtained using the equipment in Fig. 4-11, able to record flux measures for different operating temperatures.

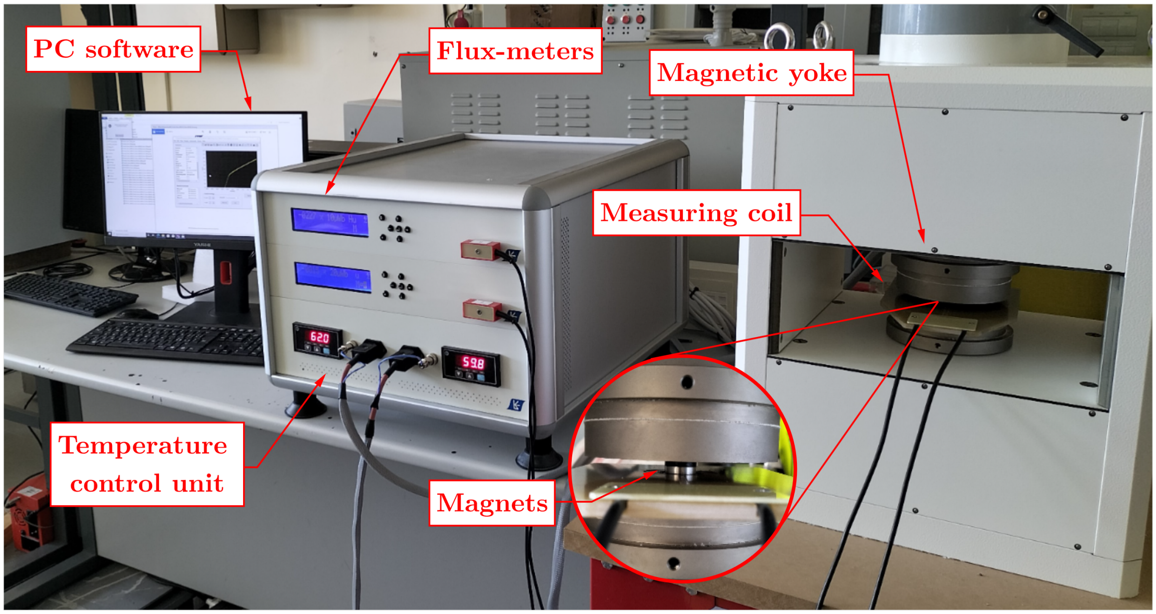

Figure 4-11: Magnet characterization experimental setup

When described equipment is used for different magnets, results in Fig. 4-12 are obtained. In the image, proportion of each material is specified between parenthesis at figure legend.

From Fig. 4-12, some conclusions about material mixtures can be extracted, specially in the context of VF-PMSM.

- Adding AlNiCo5 to NdFeB magnets brings knee point of the mixture closer to the origin. This reduces demagnetization requirements in terms of current.
- Recoil and droop permeabilities are highly affected by the inclusion of AlNiCo5, both when mixed with NdFeB and Ferrite.

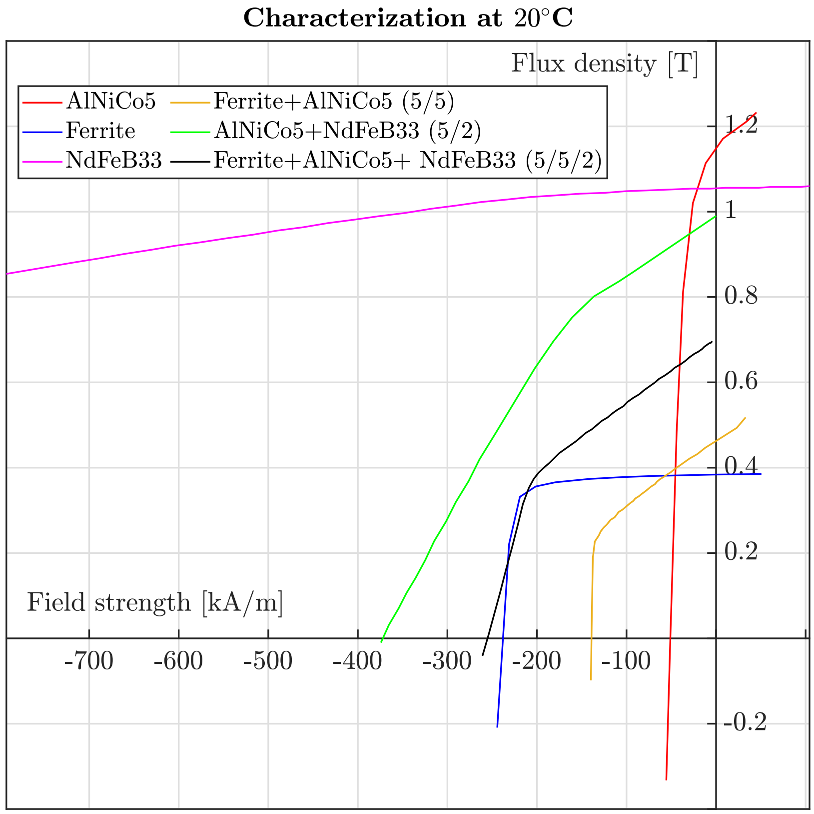

Figure 4-12: Different magnets experimental characterization

- Ferrite addition into mixtures can increase droop permeability but shows little effect on recoil permeability

Additionally, Fig. 4-13 shows how the inclusion of AlNiCo5 causes recoil trajectory after demagnetization (μ_{rec}) to be different from initial recoil permeability (μ_{rec_0}). This difference is measured and incorporated into future simulations when using material mixtures, due to its importance when studying demagnetization.

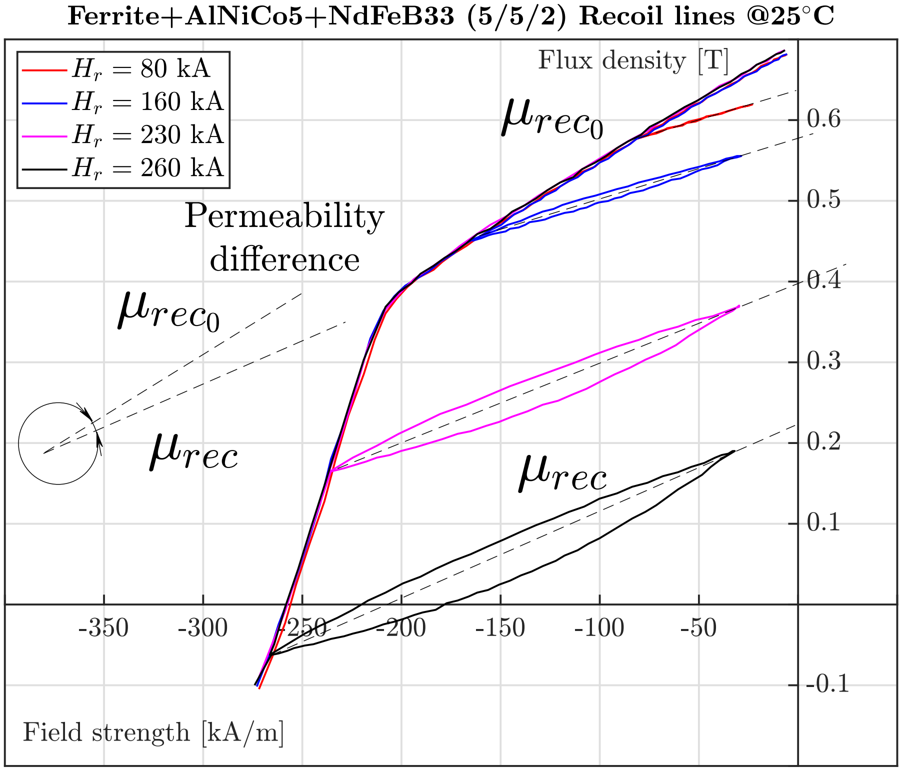

Figure 4-13: Recoil characteristic for pemanent magnet mixture composed of NdFeB, AlNiCo5 and ferrite

4.3 Test-bench results

As stated in thesis objectives, it is desired to characterize VF-PMSM efficiency at different magnetization levels. Obtained results are thought to provide correction for simulation values, in order to increase their reliability. This section will cover the procedure for experimental efficiency determination.

A summarised diagram for the setup is shown in Fig. 4-14, while its actual implementation is shown in Fig. 4-15. As seen in the image, test machine will be mechanically coupled to an auxiliary machine working in speed control. Then, by controlling current (and thus torque) following the scheme shown in Fig. 3-3, test machine can be operated in any desired point of the torque-speed characteristic.

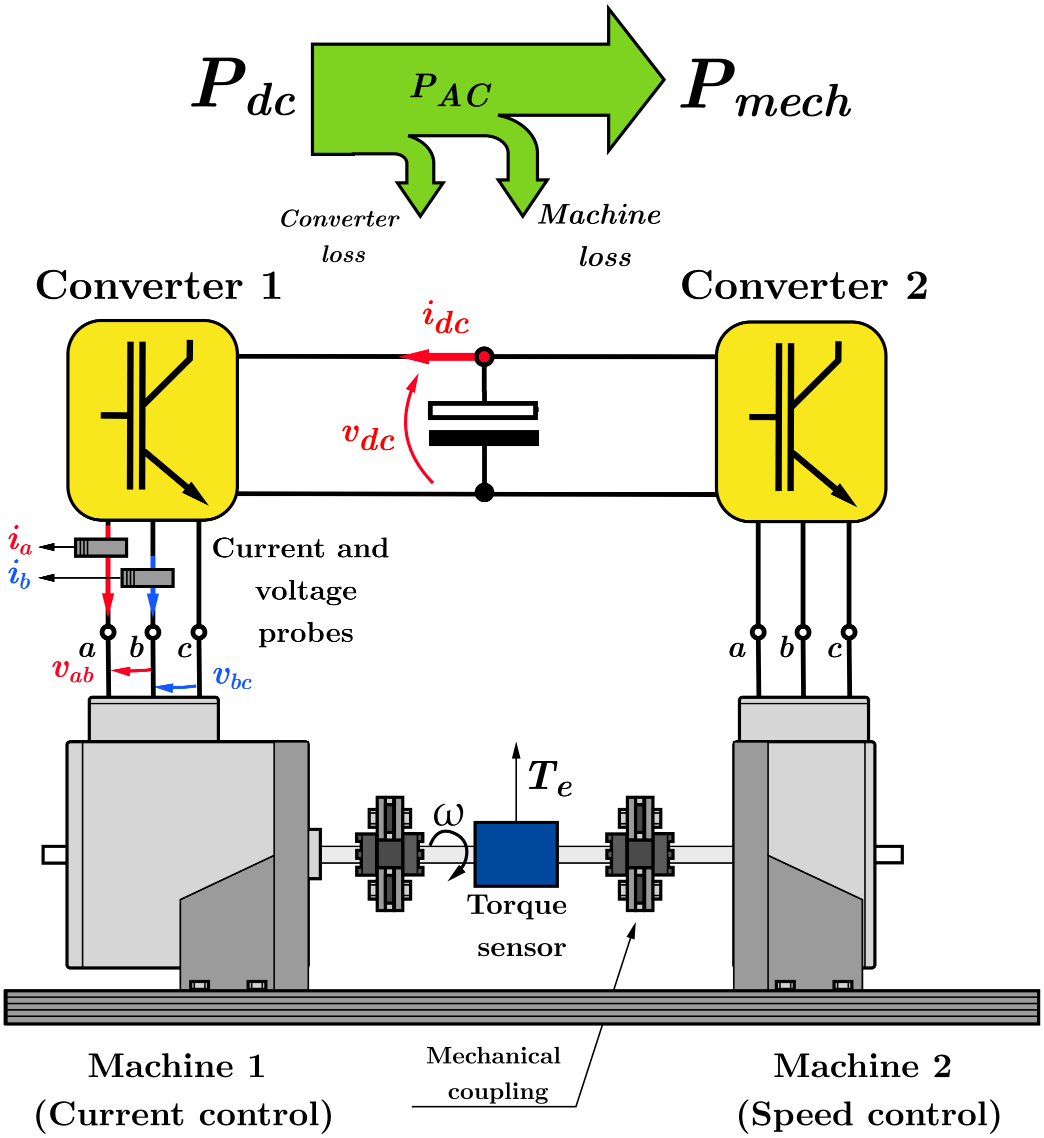

Figure 4-14: Diagram for efficiency experimental determination setup

From the scheme in Fig. 4-14, three power measures will be available for the tests:

- DC Power input into converter 1 (P_{dc})
- AC Power in test machine input terminals (P_{ac})
- Mechanical power at machine shaft (P_{mech})

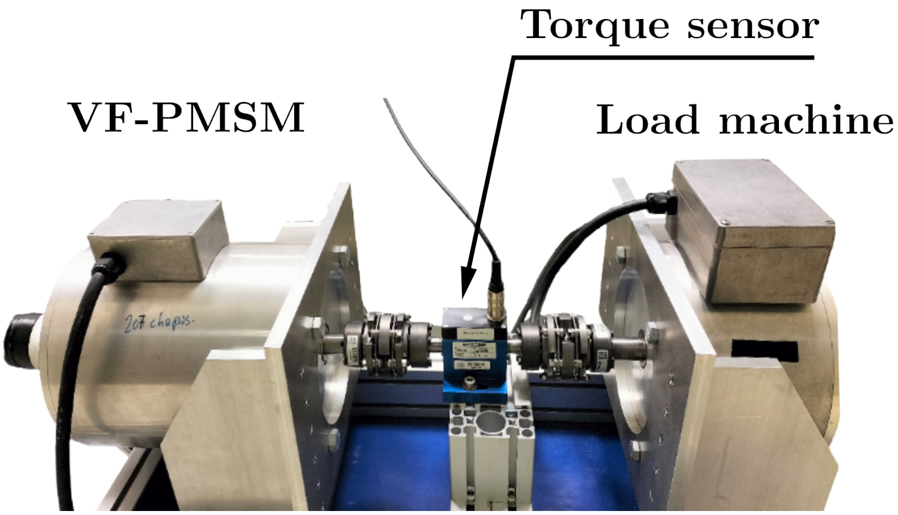

(a) Test bench

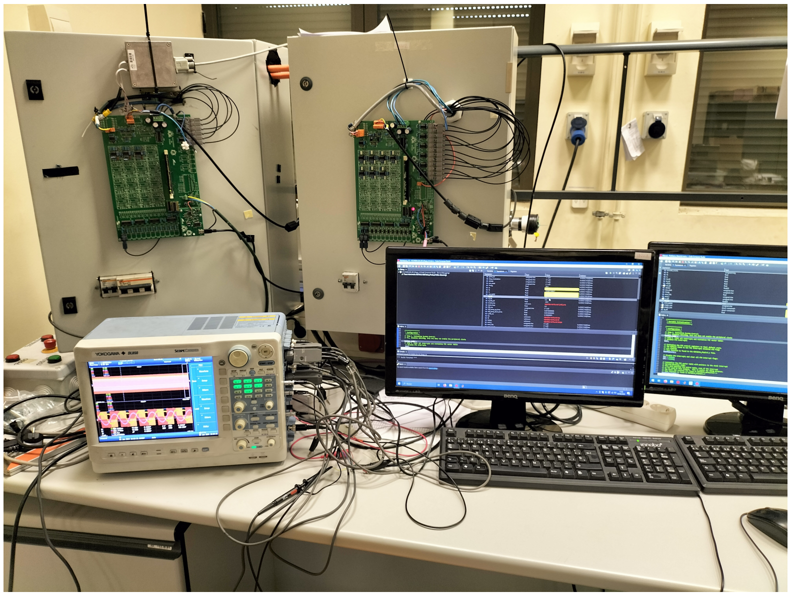

(b) Power converters and measurement equipment

Figure 4-15: Experimental setup for machine efficiency measures

For a given measure, each of these terms is computed as:

$$\begin{cases} P_{dc} = \dfrac{1}{T}\displaystyle\int_0^T v_{dc} \cdot i_{dc} \, dt \\ P_{ac} = \displaystyle\sum_{j=a,b,c} v_j \cdot i_j \cdot \cos(\varphi_j) \\ P_{mech} = \dfrac{\omega_r}{T}\displaystyle\int_0^T T_e \, dt \end{cases} \tag{4.7}$$

Where:

- v_{dc}: DC-Link voltage as measured in Fig. 4-14
- i_{dc}: DC-Link current as measured in Fig. 4-14
- v_{abc}: Fundamental machine phase voltages (RMS), computed from line voltages in Fig. 4-14
- i_{abc}: Fundamental machine line currents (RMS)
- φ_{abc}: Phase shift between fundamental voltages and currents of a given phase
- ω_r: Rotor mechanical angular speed
- T: Electrical period for AC variables (synchronism period)
- T_e: Exerted machine torque

Then, efficiency for both the converter and the machine can be computed as P_{ac}/P_{dc} and P_{mech}/P_{ac} respectively. Measures will be taken at three different speeds: 500 RPM, 1000 RPM and 1500 RPM. Current will be injected directly in the q axis.

Considered machine for the tests will be the one in Fig. 4-16, whose main ratings can be found in Table 4.1.

Rated power [kW]	1.8
Rated speed [RPM]	1500
Rated current [$\mathbf{A}_{pk}$]	11
Number of slots	60
Pole pairs	4

Table 4.1: VF-PMSM parameters

Fig. 4-17 depicts instantaneous and average power at the DC side when machine is rotating at 1000 RPM while consuming 15 A in its q axis. Next, Fig. 4-18 and 4-19 show AC variables for the same measure. While current sinusoidal nature becomes evident in sight of the figure, voltages are measured at the terminals of a switching

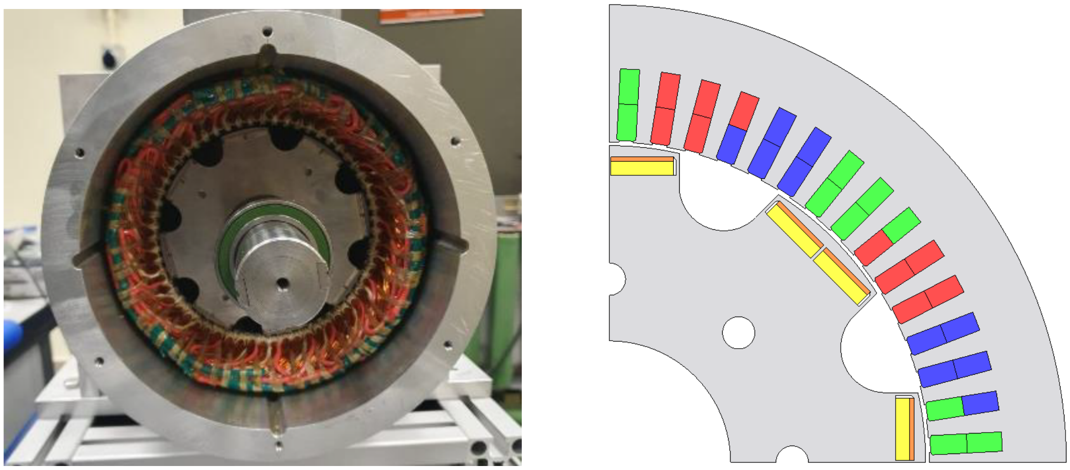
(a) Actual machine (b) FEA Model

Figure 4-16: Initial VF-PMSM prototype

converter, hardening the identification of their fundamental component.

For this reason, Fig. 4-20 depicts fundamental components of phase U voltage and current, in which an inductive power factor is identified. Finally, machine torque is shown in Fig. 4-21.

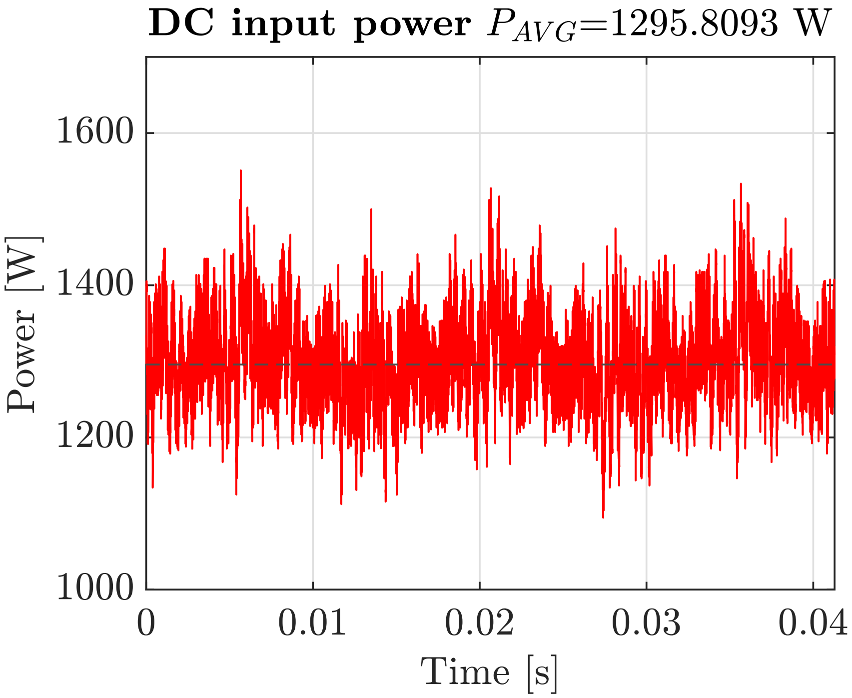

Figure 4-17: Measured power at DC side for i_q=15 A at ω_r=1000 RPM

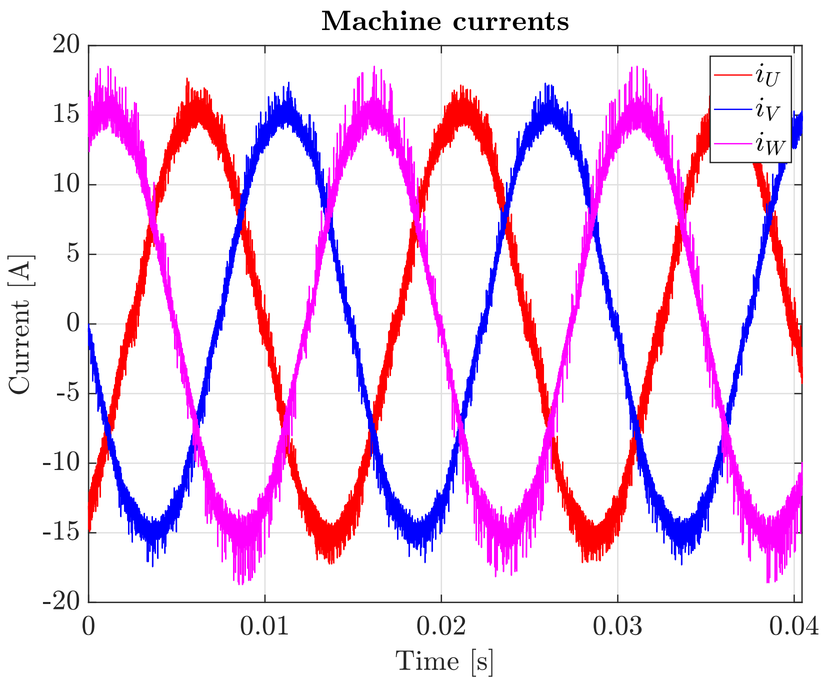

Figure 4-18: Measured machine currents for i_q=15 A at ω_r=1000 RPM

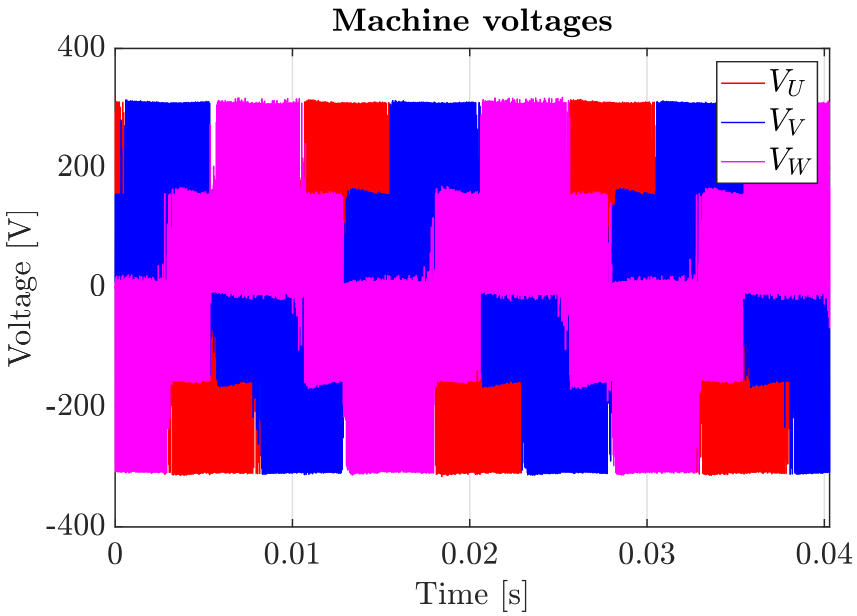

Figure 4-19: Machine phase voltages for i_q=15 A at ω_r=1000 RPM

To properly represent mechanical losses inside the simulation model, the test machine is also operated at no-load. When current-controlled machine is not exerting any torque, speed-controlled machine must only overcome its mechanical losses. Since they are typically considered to depend linearly on speed, a linear fit is com-

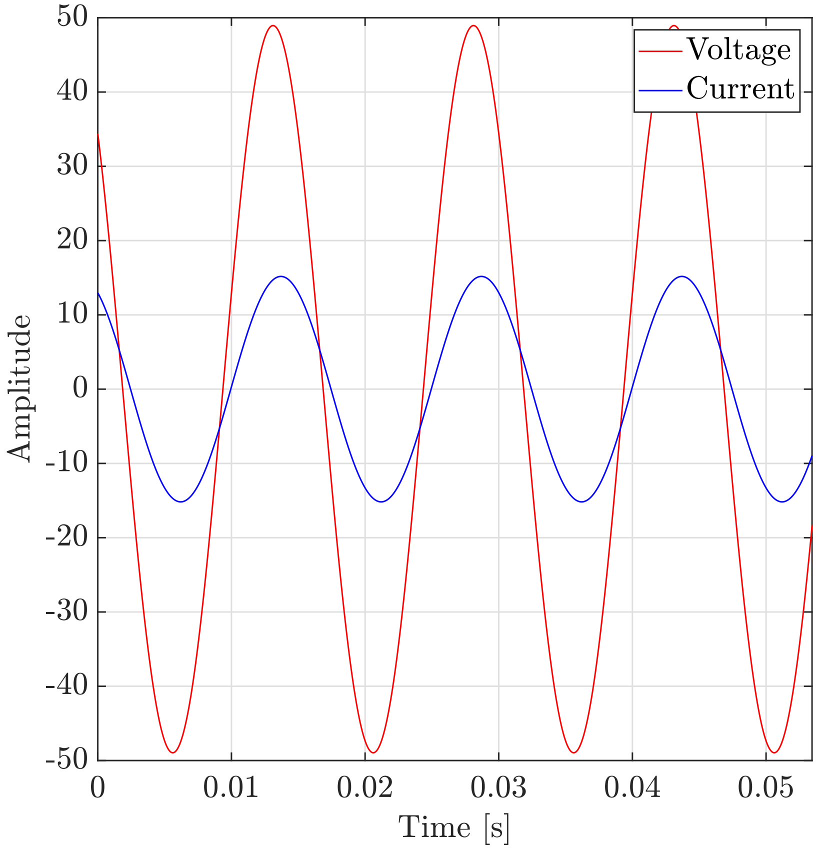

Figure 4-20: Fundamental voltage and current at phase A for i_q=15 A at ω_r=1000 RPM

puted with laboratory measures as shown in Fig. 4-22.

Fit quality is reasonably good and a loss coefficient of 71.39 W/kRPM is obtained.

As mentioned earlier in the document, MS manipulation is achieved with short i_d current pulses like the one shown in Fig. 4-23. Resulting MS after a pulse is then estimated by measuring no-load induced voltage. The ratio between fundamental components is taken as MS level. All of the described procedures and measures are followed for two magnetization states: 100% and 75%

After the completion of the tests, obtained efficiency results are shown in Fig. 4-24 from which an interesting conclusion can be extracted: efficiency gap between different MS gets reduced as speed increases, specially for low torque values.

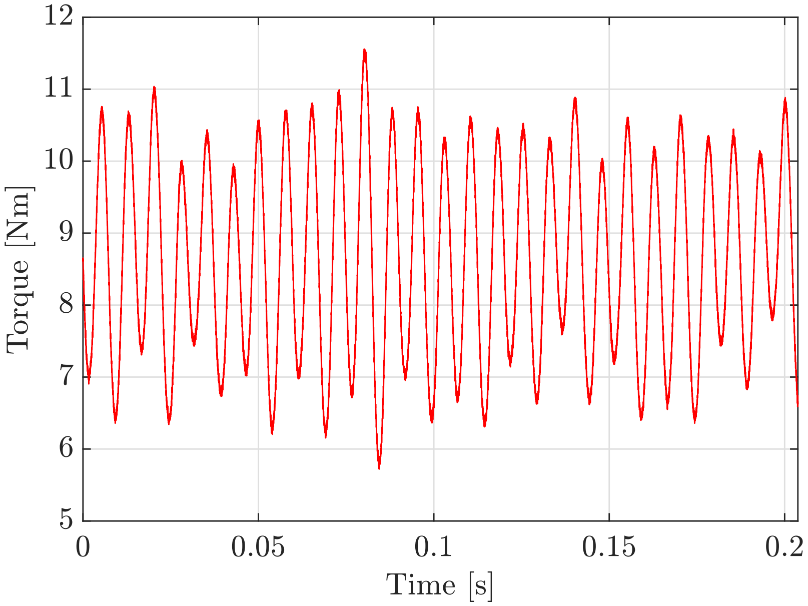

Figure 4-21: Measured machine torque for i_q=15 A at ω_r=1000 RPM

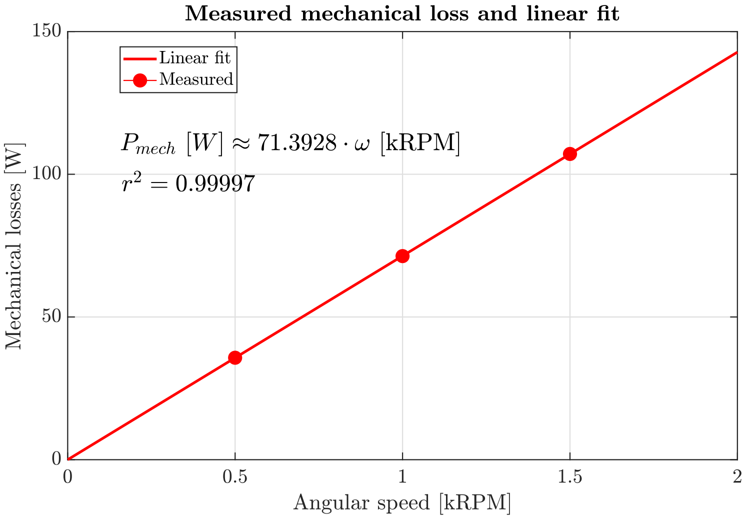

Figure 4-22: Measured mechanical losses

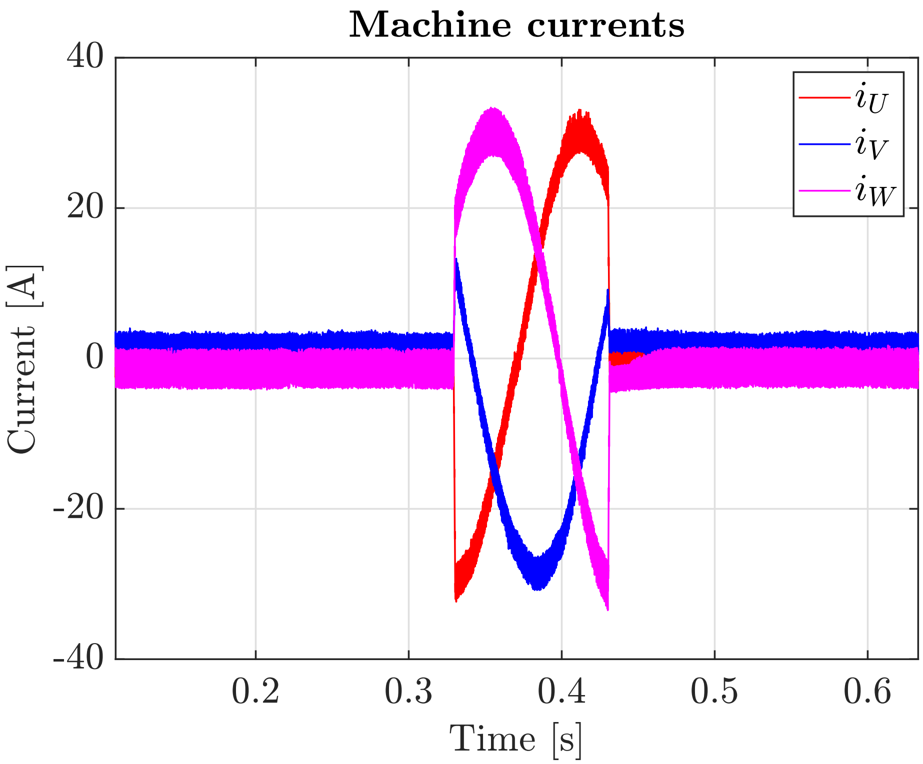

Figure 4-23: Measured current during demagnetization pulse i_d =-30 A at ω_r = 100 RPM

4.4 Power converter

Power converter mentioned in Chapter 2 was built and tested at low load. It is organized as conceptually shown in Fig. 4-25, in which main elements and features can be identified. Actual implementation of the power converter can be seen in Fig. 4-26. The converter is thought to be controlled using a *Hardware In The Loop* (HIL) platform, but tests could not be carried out due to a lack of time.

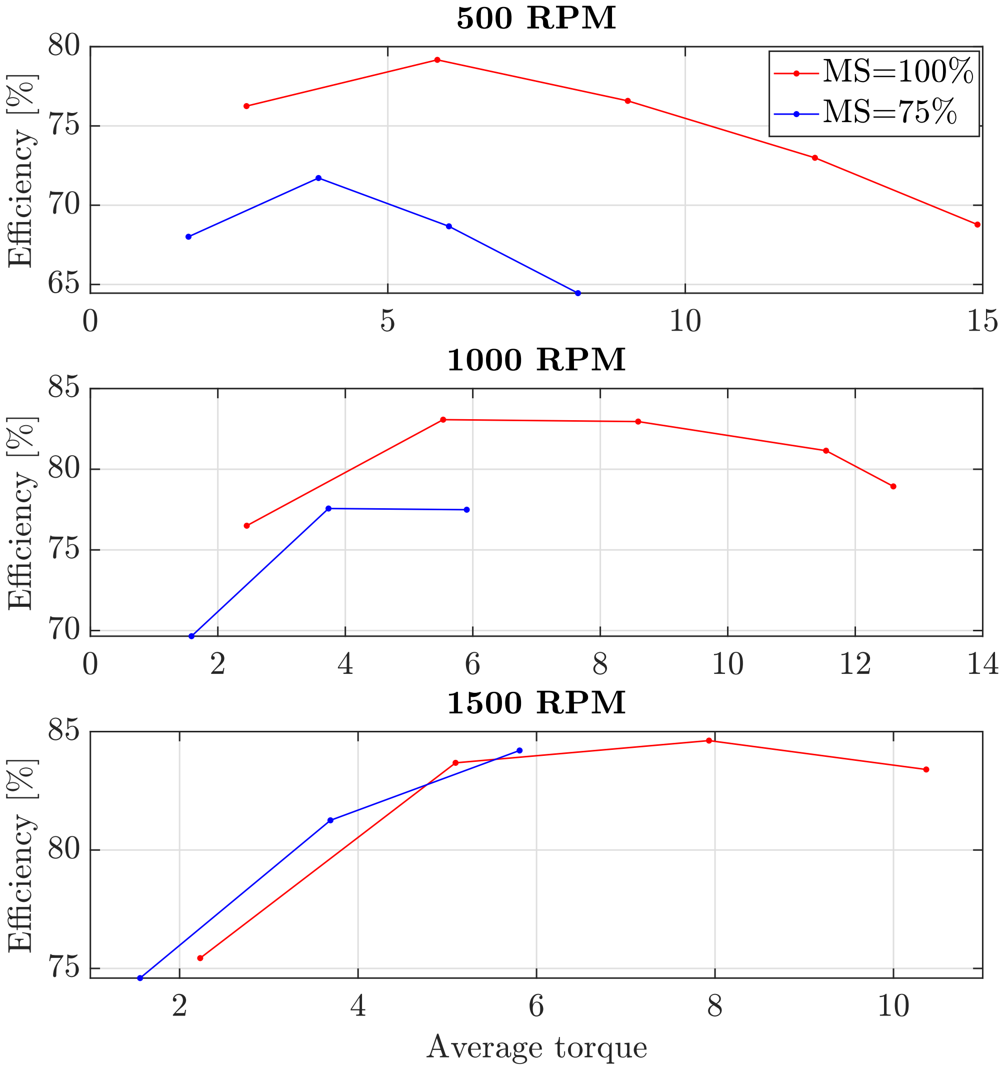

Figure 4-24: Measured efficiencies during test bench experiments at different magnetization states

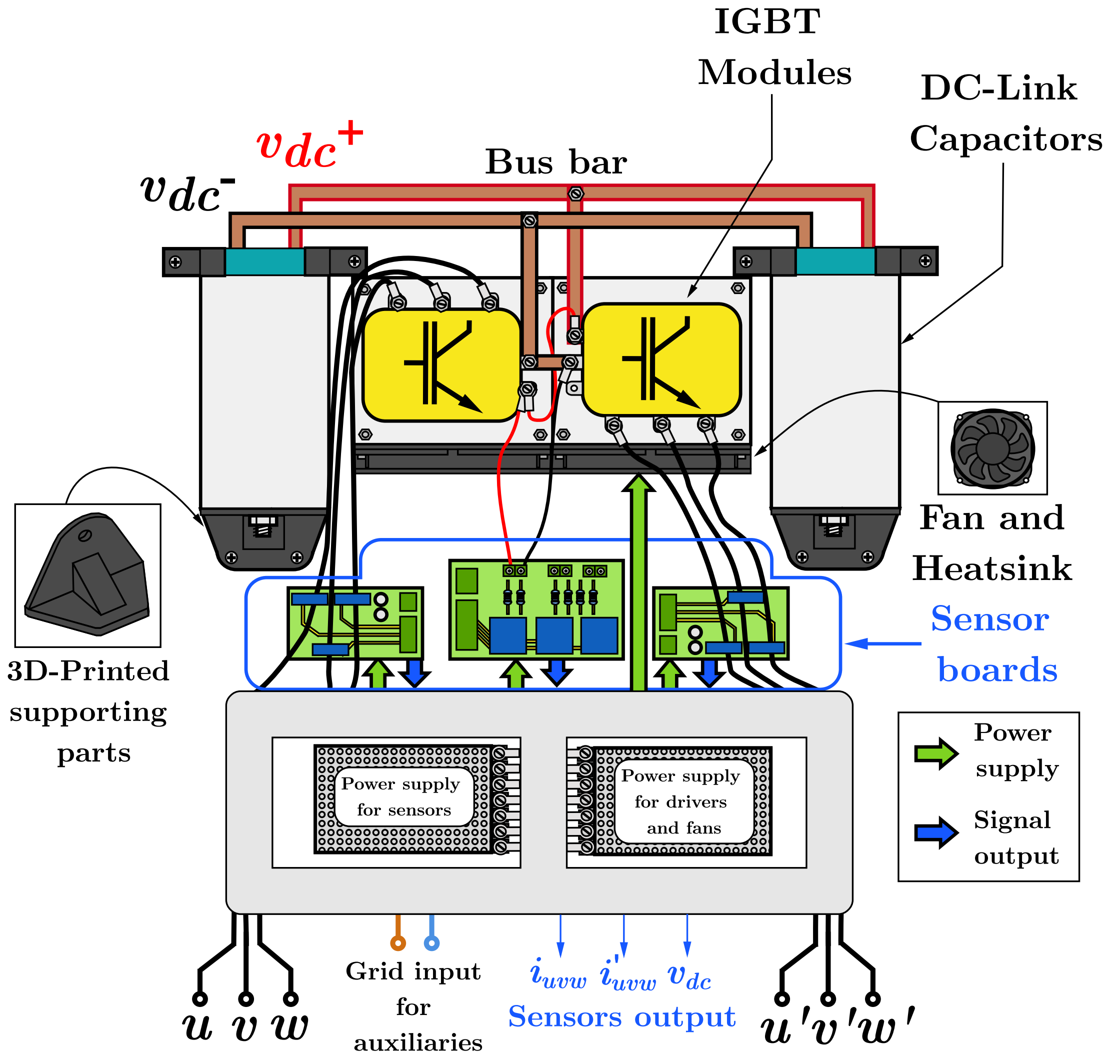

Figure 4-25: Conceptual scheme of the power converter

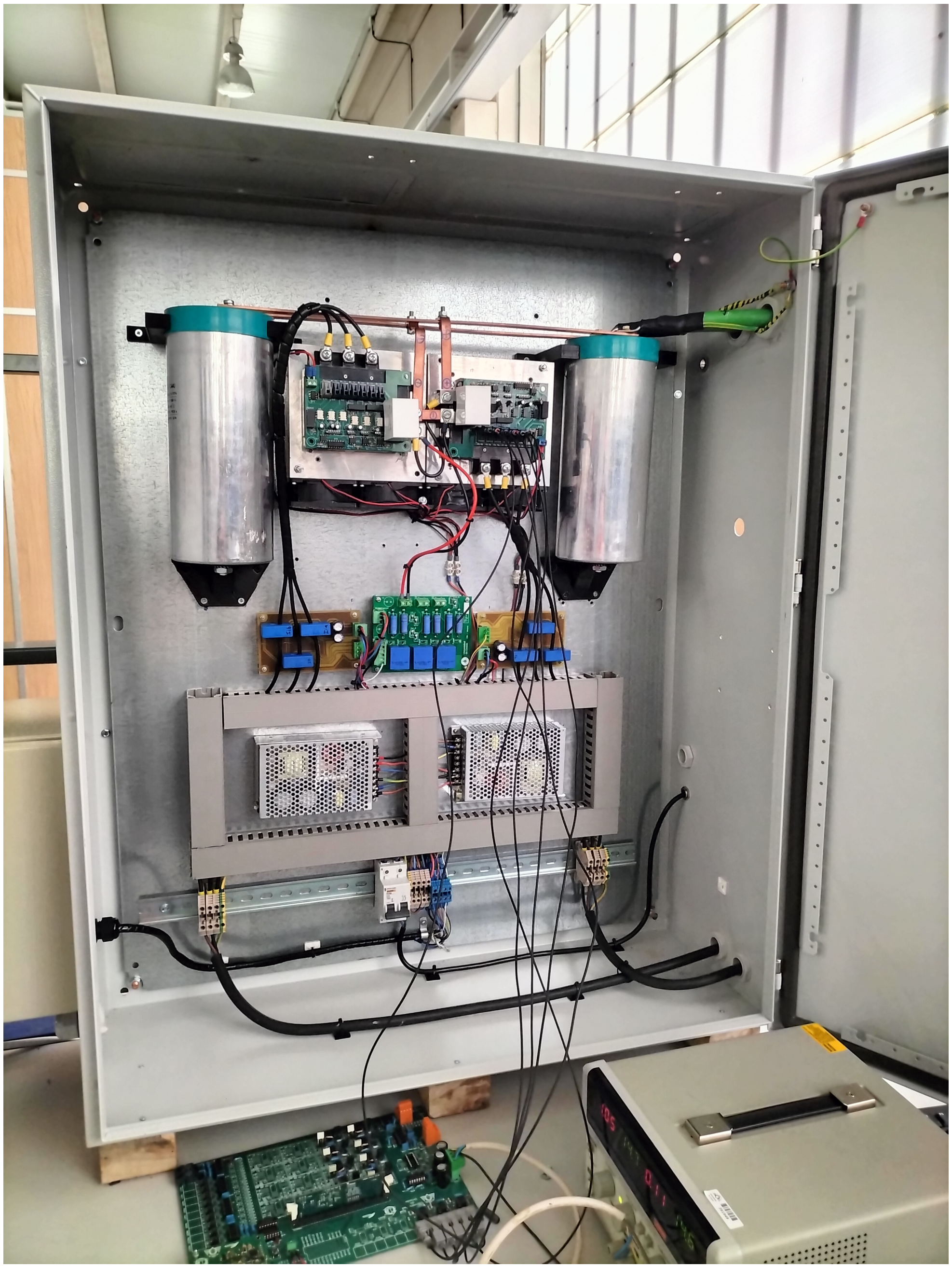

Figure 4-26: Developed *back-to-back* converter during preliminary tests

Chapter 5

Finite-element simulation results

Experimental data obtained in previous section is used to run FEA simulations. This simulations are mainly thought to estimate potential savings when using VF-PMSM in an aircraft application. In addition, an optimized machine design is also proposed using this software.

5.1 Energy saving for a flight profile

As mentioned in previous sections, typical flight missions have a high degree of predictability and simplicity when compared with other applications [36][37]. With the adoption of VF-PMSM, this feature can be exploited to save energy, being the goal of the section to validate this hypothesis.

Fig. 5-1 contains a summarised flowchart of the followed procedure. First step is to consider a short-range flight profile , and to analyze power requirements during the flight. Next, a reliable efficiency map of the adopted machine must be developed. Finally, power requirements based on flight information are joined with machine efficiency map to yield optimum operating points, and associated energy consumption.

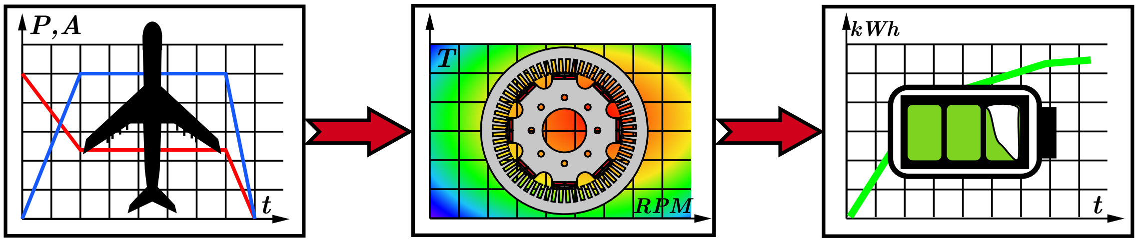

Flight profile information **Machine efficiency map** **Energy consumption**

Figure 5-1: Methodology for energy savings determination

Since the goal of the section is to identify potential benefits of MS manipulation in short flights, the method will be applied to the following cases:

- Machine with fixed magnetization state during the entire flight
- Machine with modified magnetization state at specific points

5.1.1 Proposed flight profile

First task is the proposal of a short-range flight profile. As shown in [37], typical flight profiles can be summarised by three stages: ascending, cruise mode, and landing. They are noticeably different in terms of power requirements, as rated power is only needed during ascending phase. Fig. 5-2 (Ellaborated with data in [36][37]) contains a summarised power profile for a short flight, that will be used throughout the section. Note that an interesting conclusion can be extracted from the graph, specially when considering VF-PMSM adoption. If the machine is operated at controlled constant speed, it could be deduced that fewer torque is needed during cruise and landing phases of the flight. If less torque is needed, magnet flux linkage can be modified to reduce losses. It can be considered that machine magnetization state is reduced after the takeoff is finished.

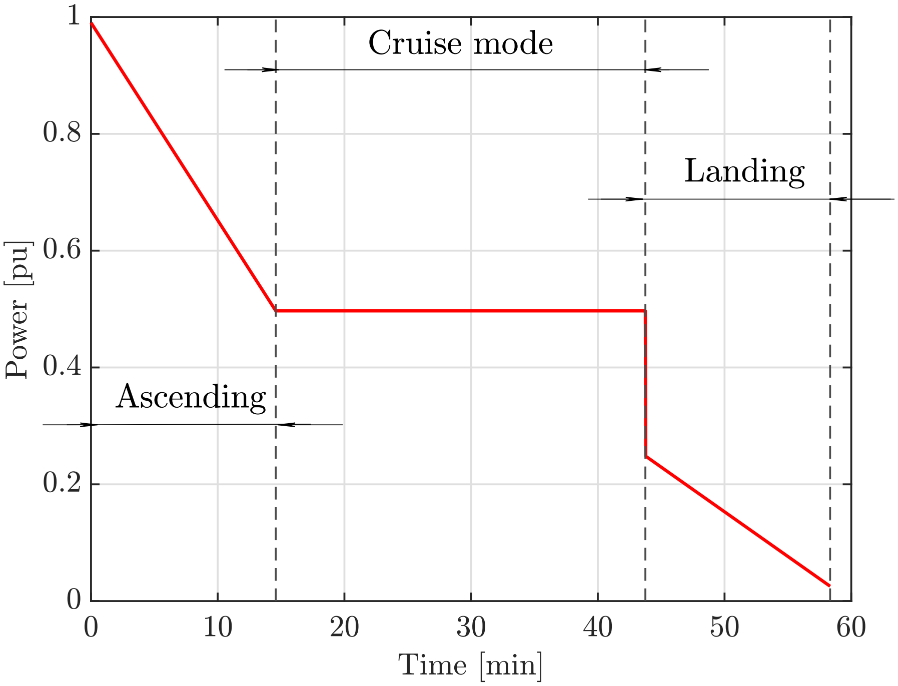

Figure 5-2: Simplified flight profile

5.1.2 Efficiency map development

Next task to accomplish is the development of an accurate efficiency map for the electrical machine. The map will be obtained by means of FEA software, because experimental characterisation can not provide good resolution in the whole torque-speed characteristic. However, early parts of the document justified the need of experimental correction in FEA models. These two imply that simulation results and models must be fed with experimental results to be trustworthy.

The approach is summarised in Fig. 5-3. In previous chapter, experimental efficiency measures were obtained for a set of points within torque-speed characteristic. Then, next step is to run a simulation for the entire machine characteristic in FEA software. After that, results from simulations and laboratory measures are compared in order to obtain correction coefficients. Finally, this coefficients are linearly extrapolated to the entire curve, increasing efficiency map reliability.

Considered machine design throughout the section will be the one in Fig. 4-16.

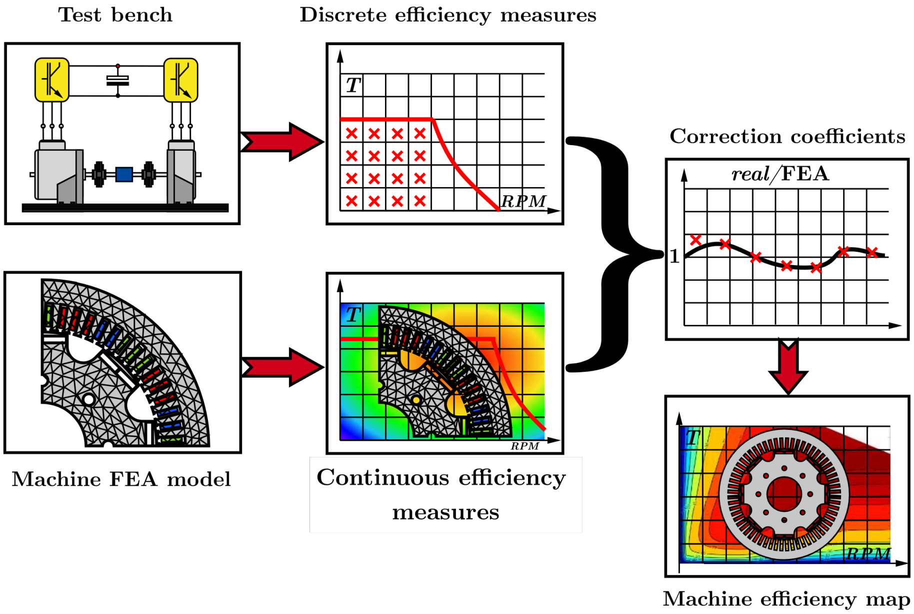

Figure 5-3: Efficiency map development scheme

Next step is to run a simulation accounting for the entire torque-speed map. Key aspect to consider prior to the simulation launch is loss modelling configuration. Copper losses will consider DC and AC effects as explained by (3.31) discussed in Section 3. For iron losses, (4.6) introduced in Section 4.1 is used, loss coefficients in the equations are provided by machine cores manufacturer and depicted in Fig. 5-4. Finally, mechanical loss are configured to be linear according to fit in Fig. 4-22.

After described simulation is run, obtained efficiency map is shown in Fig. 5-5 for the case of fully-magnetized magnets. If simulation is repeated for a MS of 75%, experimental and simulation results can be compared. Fig. 5-6 contains simulated and experimental data for ω_r=500 RPM. It can be noted from the image that the simulations are not accurate enough to predict efficiency values within an acceptable range. However, difference among magnetizing states and efficiency evolution with torque values seems reasonably similar. For this reason, it is believed that the discrepancy could be solved by considering correction coefficients.

This procedure primary flaw is the lack of defined experimental efficiency values

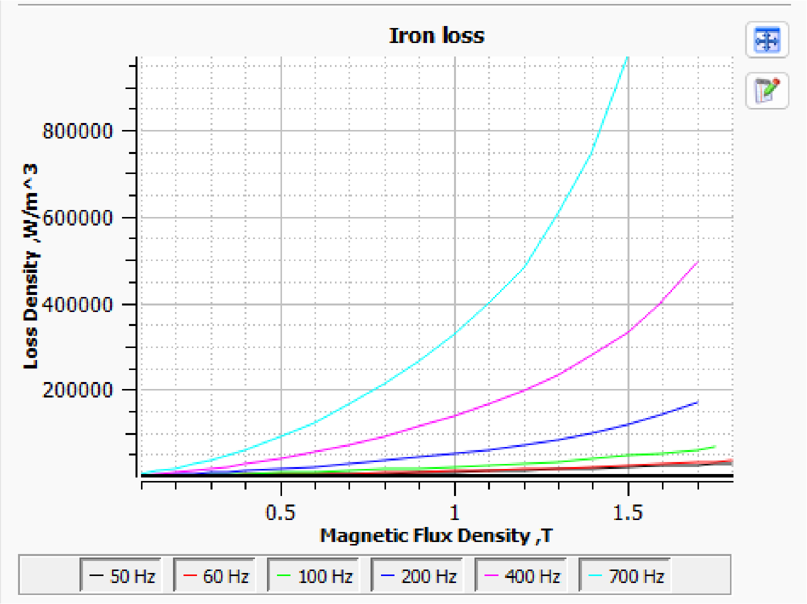

Figure 5-4: Iron-loss manufacturer data for machine laminated sheets

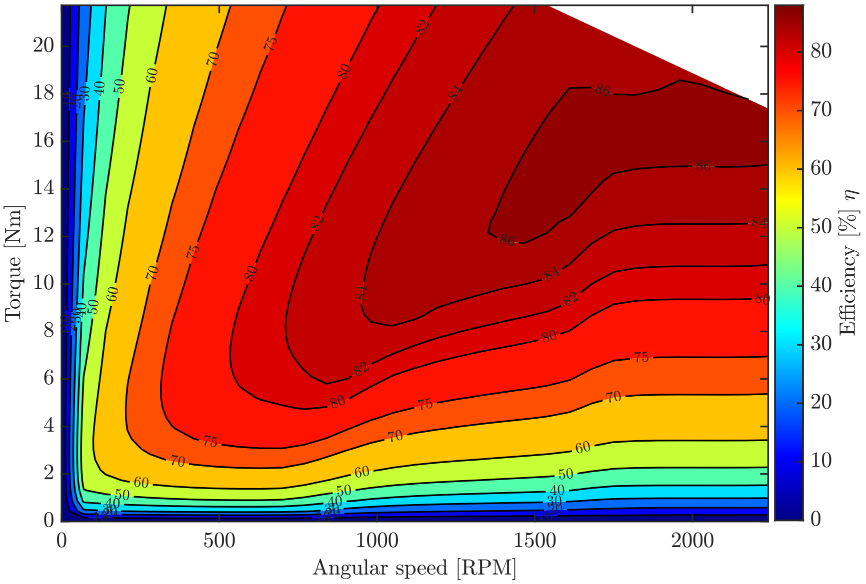

Figure 5-5: Simulated efficiency map for 100% MS

across the whole torque range. Fitting curves can be used to solve this problem.

Based on the curve shapes found in Fig. 5-6, experimental data can be approximated with a Weibull distribution of the type in (5.1), where T_e stands for machine

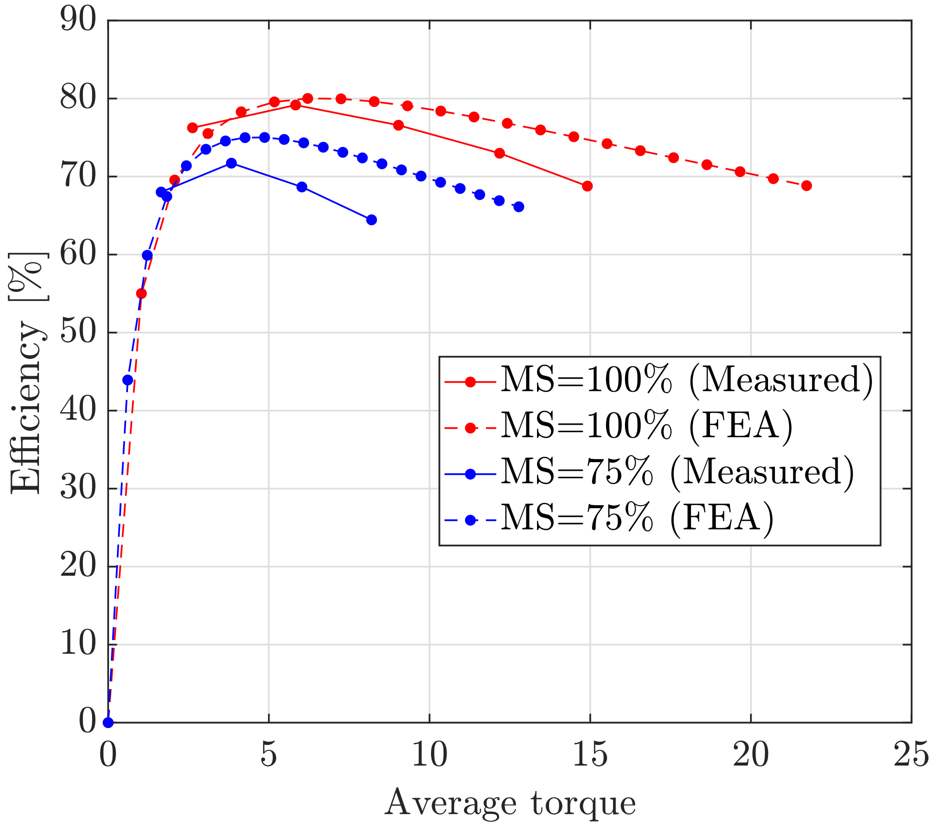

Figure 5-6: Measured and simulated efficiencies for changing load at ω_r=500 RPM

average torque and a, b, c, d and k are fitting parameters.

$$\eta_{pu} \approx \frac{a}{b} \cdot \left(\frac{T_e}{d}\right)^a \cdot e^{\left(\frac{-T_e}{c}\right)^k} \tag{5.1}$$

An example of the fit is provided in Fig. 5-7 for experimental data measured at 100% MS and ω_r=500 RPM. Fits are computed for all experimental measures and the ratio between real and FEA efficiencies is shown in Fig. 5-8. Apparently, FEA estimation is more robust against velocity changes when magnetization is higher. These values are introduced in previously computed efficiency maps in order to increase their reliability (correction coefficients for speed values different from the ones in Fig. 4-24 are obtained by linear interpolation[15]).

---

[15] This feature is implemented by default in JMAG-Software

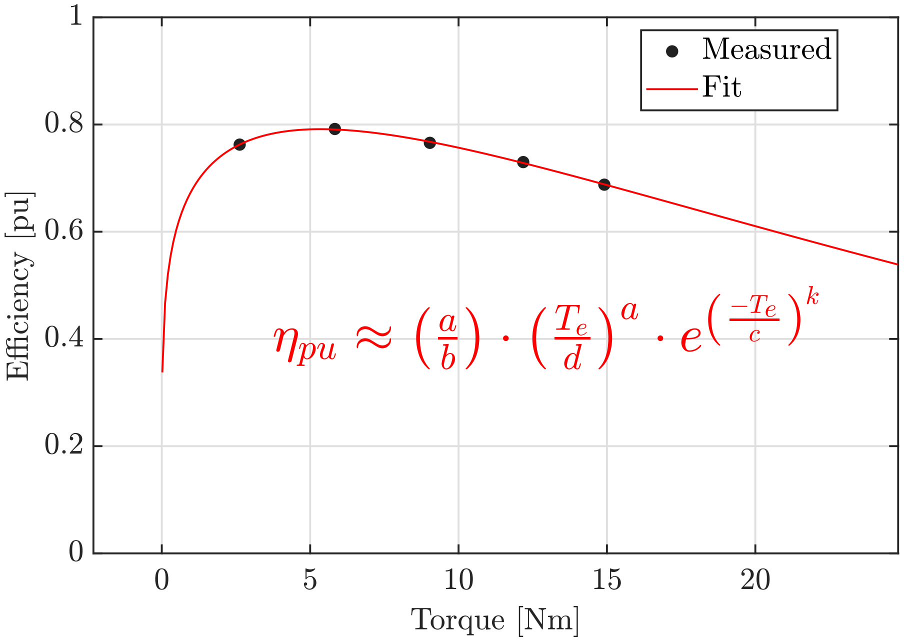

Figure 5-7: Fitting curve for experimental efficiency measures

5.1.3 Efficiency increase and energy savings

After the speed profile is defined and the efficiency map for the machine is available for two different MS, attainable energy savings for a scaled case can be estimated.

At the current stage of the project, it is desired to operate the machine at constant speed during the flight [38][16].
This implies that machine operating point will move vertically on the efficiency map (for a given angular speed), which can be exploited to maximize energy savings if machine power and speed are known.

Angular speed found at machines propelling aircraft falls in the range of 0.8 and 1 pu, while developed power has two defined values of 0.5 and 1 pu according to the profile in Fig. 5-2 [36][39]. This is incorporated in Fig. 5-9, in which dashed white lines mark speed limits while solid blue lines represent power isolines. Top subfigure represents machine efficiency curves for 100% MS, and bottom image accounts for

---

[16] Aerodynamic *drag* and *lift* forces are affected by wing *angle of attack* , this enables the machine to work at constant speed and torque while controlling aircraft speed.

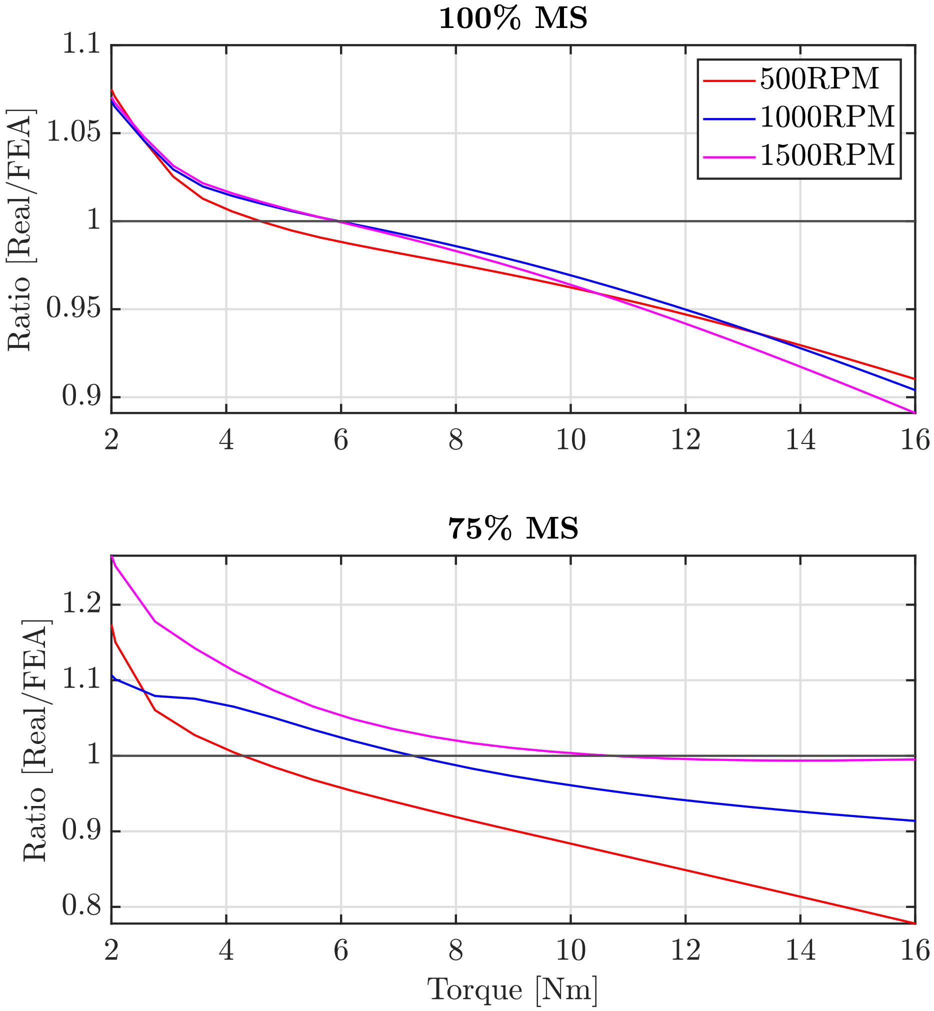

Figure 5-8: Correction ratio for different speeds and magnetization states

the ratio between 100% MS efficiency and 75% MS efficiency. It is used to determine two machine operating points as follows:

- **Takeoff:** Obtained where nominal power isoline meets a maximum efficiency contour at the MS 100% curve.

- **Cruise:** Previous step will determine rotational speed. Operating point for cruise stage is found in the MS75% efficiency curve, where speed from previous point meets 0.5 pu power isoline.

From the figure, it can be noted that the ratio between the two efficiencies is below

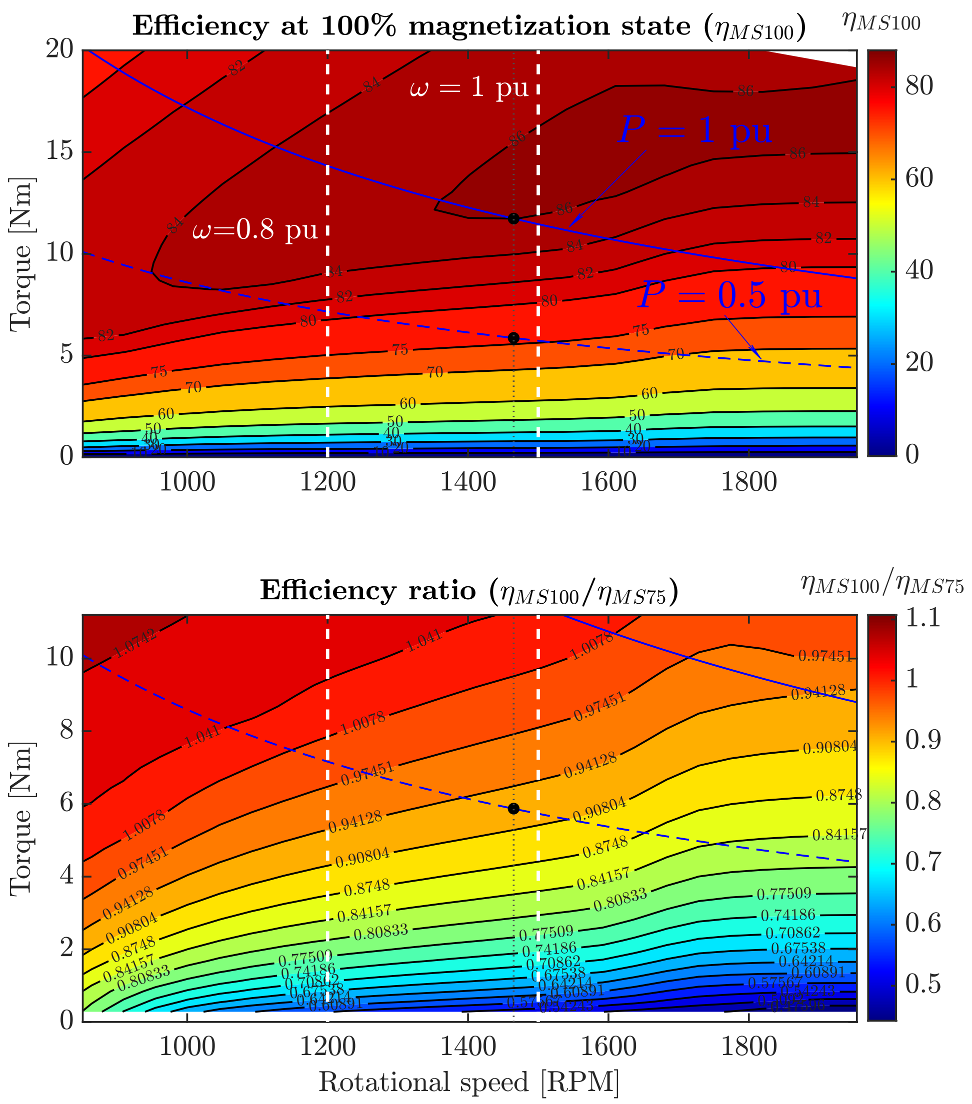
Efficiency at 100% magnetization state (η_{MS100})

Efficiency ratio (η_{MS100}/η_{MS75})

Figure 5-9: Efficiency increase considering flight profile

1 for the entire P=0.5 pu isoline. The image can be used to conclude that a demagnetized machine is more efficient at lower torque values and high speeds. The difference could be explained (among others) by flux amplitude dependency of iron losses. As seen in Section 3, iron losses will be affected by flux density at every element. Since the magnets are exhibiting a lower remanence, iron cores will show less losses.

Efficiency ratio takes a value of 92% in the selected point at the bottom of Fig. 5-9. Then, 8% less losses will be present during cruise mode, which is the longest part of the flight. However, ratio among efficiencies will be further decreased during landing, where power is reduced to an almost null value. Fig. 5-10 provides the time evolution of efficiency ratio when flight profile in 5-2 is considered. In the computation of energy consumption, magnetization state manipulation has been neglected due to its low value for the test machine [40].

A summary of the results is contained in Table 5.1, in which it is relevant to remark that the results are provided for a low-power prototype. If the same results were extrapolated to a higher power machine, considering an estimate of 50,000 short flights per year [9] and an average energy price of 100.18 €/MWh [41], 230.94 € could be saved yearly per machine kW. This figure yields economic savings in the order of thousands of euros, obtained solely by a proper modification of machine magnetization state.

	MS Manipulation?		
	No	**Yes**	**Difference**
Average efficiency [%]	74.81	80.97	+6.16
Consumed energy [kWh]	1.095	1.012	-0.083

Table 5.1: Energy savings results

5.2 Machine prototype design optimization

To evaluate control strategies, loss models, MS manipulation schemes, or any other relevant knowledge, a prototype electrical machine is needed. This part of the document will cover its design stage. The design will be based on an existing prototype shown in Fig. 4-16, whose parameters can be found in Table 4.1. New prototype will modify some of its features to improve its performance and fix its issues.

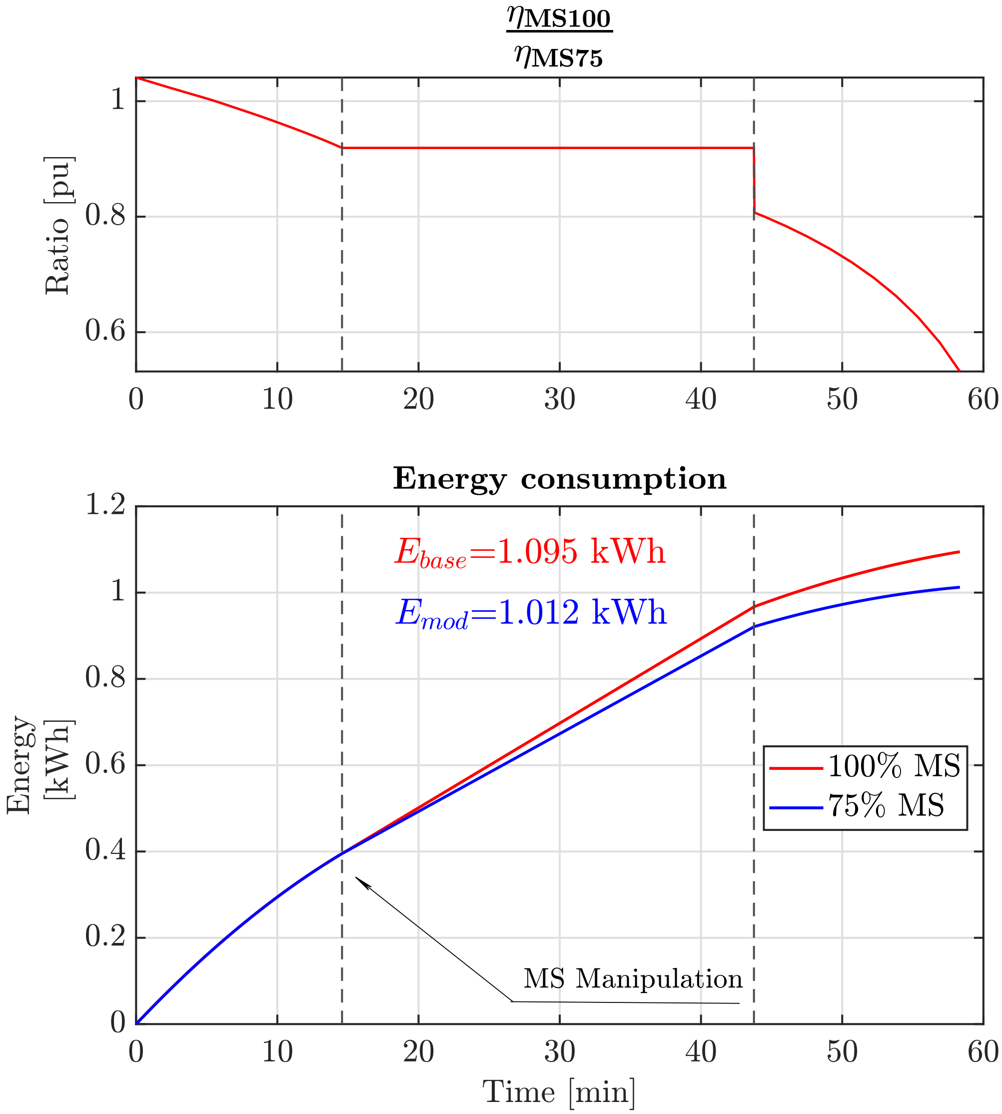

Figure 5-10: Energy savings for the simulated profile

5.2.1 Rotor design

The first issue with respect to the initial machine geometry is the existence of segmented magnets, separated with a slot as shown in Fig. 5-11. Due to the variable-flux nature of the machine, tests are usually performed at different temperatures, magnetization states or materials. This implies that magnets are frequently removed and reinserted into the machine in between tests. The existence of these slots hardens magnets manipulation and will therefore be removed as shown in the same figure.

Additionally, live (chamfered) corners are also complicating magnet removal and will thus be modified for next design.

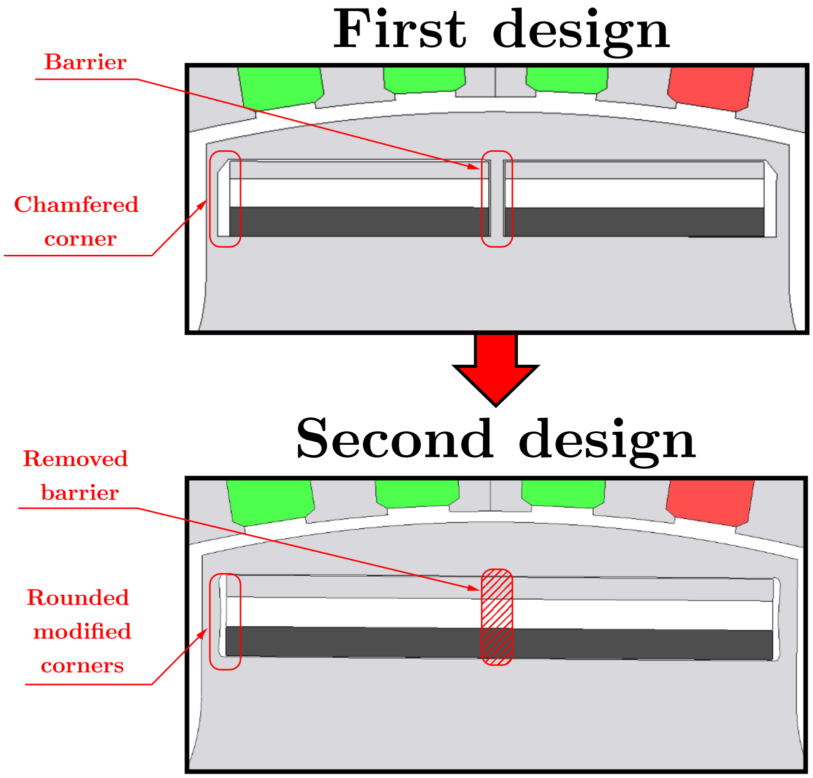

Figure 5-11: Rotor magnet slot modifications

Next modification involves an electromagnetic simulation at rated load. Note from Fig. 4-16 that original design contains holes close to rotor shaft. These material removal is justified to reduce loss and improve air circulating trough the core. However it can be seen in Fig. 5-12 that the area around the holes shows little to no flux density. This area is not contributing to the electromagnetic performance of the machine, and is adding weight. In consequence, this holes will be enlarged following flux lines to reduce machine weight as shown in Fig. 5-13, in which same simulation has been launched.

Finally, any design modification has to be verified in a mechanical domain simulation. It must be ensured that centrifugal forces do not cause an excessive deformation on machine rotor. This criteria will be measured by means of Von Misses stress, which must be kept below material maximum limit (240 MPa). Corner dimensions will be

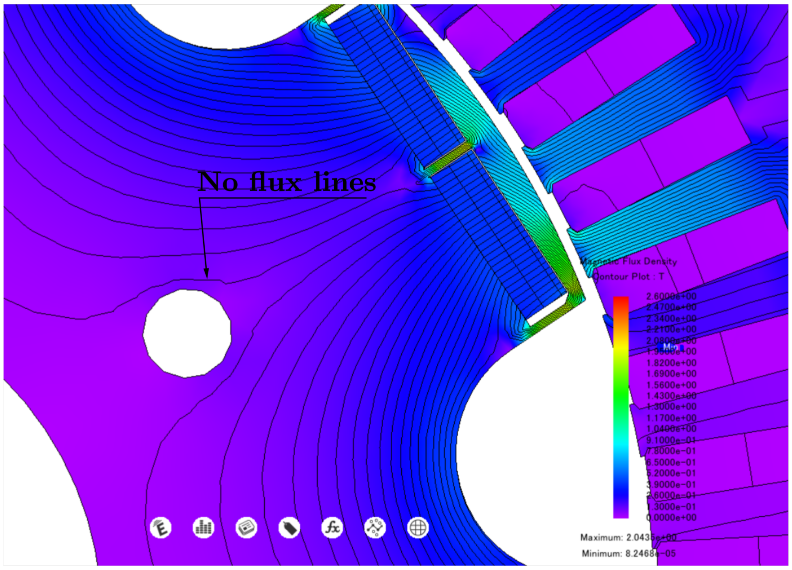

Figure 5-12: Flux lines around machine holes under rated load

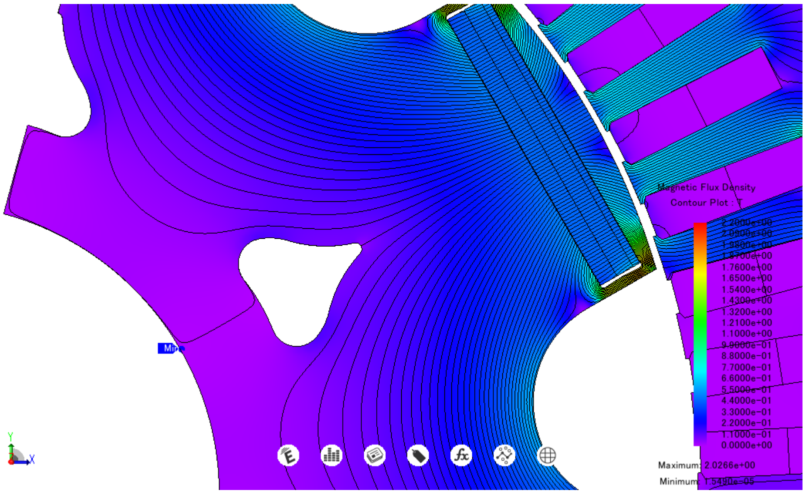

Figure 5-13: Flux lines around machine hole under rated load in modified design

selected to ensure they do not exceed this limit. Because centrifugal force causing the deformation is dependent on angular speed, maximum yield stress is addressed at very high rotating conditions. Results are shown in Fig. 5-14, in which special attention is paid to the corners (most critical part). From the image, obtained maximum yield stress at 9500 RPM is 231.2 MPa, thus validating machine design modifications.

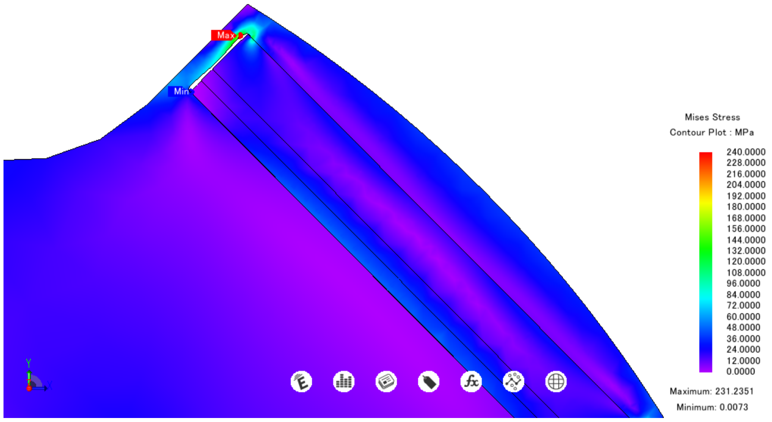

Figure 5-14: Modified design mechanical verification for centrifugal forces at 9500 RPM

5.2.2 Magnet arrangement optimization

As explained in Section 3.4, parametric and topology optimization techniques can be used to enhance machine design. Present section shows how this approach can help to improve magnet arrangement in a variable-flux machine. While series and parallel are most commonly cited magnet topologies in VF-PMSMs [20], present work aims to find another possibility using topology optimization. Once that a suitable topology is identified, a parametric optimization is run to further improve obtained design.

Starting point is the topology shown in Fig. 5-15, in which 40% of the magnet slot is filled by NdFeB magnet, while the rest is occupied by AlNiCo5.

A Gaussian network is built to fill the design region as depicted in Fig. 5-16. Distributions are programmed to intersect at half their radius (standard deviation), this practice is reported to yield better optimization results [31].

The algorithm is run for 50 generations with a population size of 25. For the

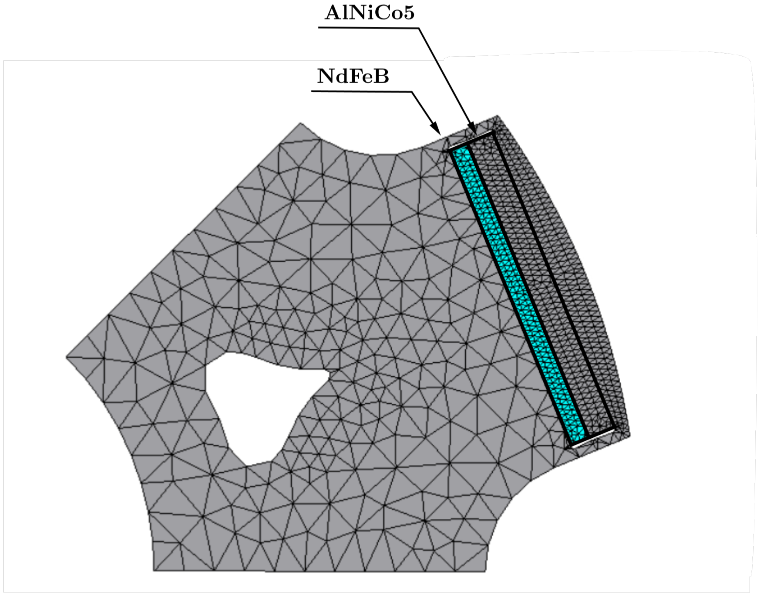

Figure 5-15: Input initial topology for the NGnet optimization

objective function, average torque and torque ripple are considered. The first function will be maximized, while the second will be minimized.
Once the simulation is run, obtained results are the ones in Fig. 5-17, in which 4 generations in different stages of the optimization are shown. Note how dispersion among individuals is reduced as generation number increases.

However, results face two inconveniences: obtained torque ripple is too high[17], and manufacturing feasibility is not ensured for all results. To illustrate this last challenge, consider the topologies in Fig. 5-18. Both belong to last generations and have reasonably good results in terms of average torque and ripple. However only the one in Fig. 5-18b is feasible in practice. In fact, the idea of having AlNiCo5 on slot sides, with NdFeB on the center is found on multiple cases among solutions. This topology combines high average torque with low ripple and manufacturing feasibility. For this reason, case in Fig. 5-18b is kept for the parametric optimization stage.

Reason to run a parametric optimization is related with MS manipulation. To reduce computation time, previous simulation did not consider that the MS of the magnets needs to be changed without excessive current. Since parametric optimiza-

---

[17] This can be attributed to the selection of relative weight for each objective functions.

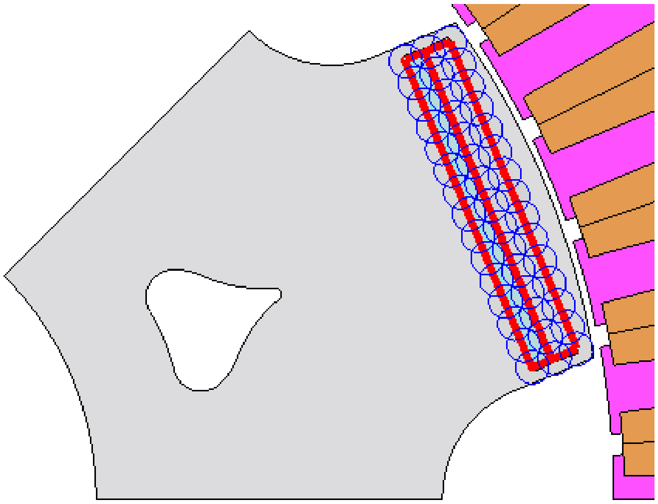

Figure 5-16: Gaussian network in initial machine geometry

tion can be faster now topology is dictated by previous algorithm, MS manipulation capability is covered following a parametric approach.

First step is to set design variables as depicted in Fig. 5-19. Then, multiple simulation cases are configured, every new case will modify these parameters, and evaluate machine design in terms of average torque, torque ripple, and remagnetization capability. This last aspect is quantified as follows:

- Machine initial MS is reduced by setting AlNiCo5 magnets as demagnetized. Their initial remanence is 30% of their nominal value.
- BEMF in this situation is measured, its fundamental component is computed and denoted by $v_{initial}$.
- A short remagnetizing i_d pulse of 6 pu (66 A) is commanded
- BEMF is measured again and its fundamental component is denoted by v_{final}
- Remagnetization capability is given by:

$$\Delta \text{MS}\% = \frac{v_{final} - v_{initial}}{v_{initial}} \tag{5.2}$$

The workflow is illustrated in Fig. 5-20. In which two separate simulations are

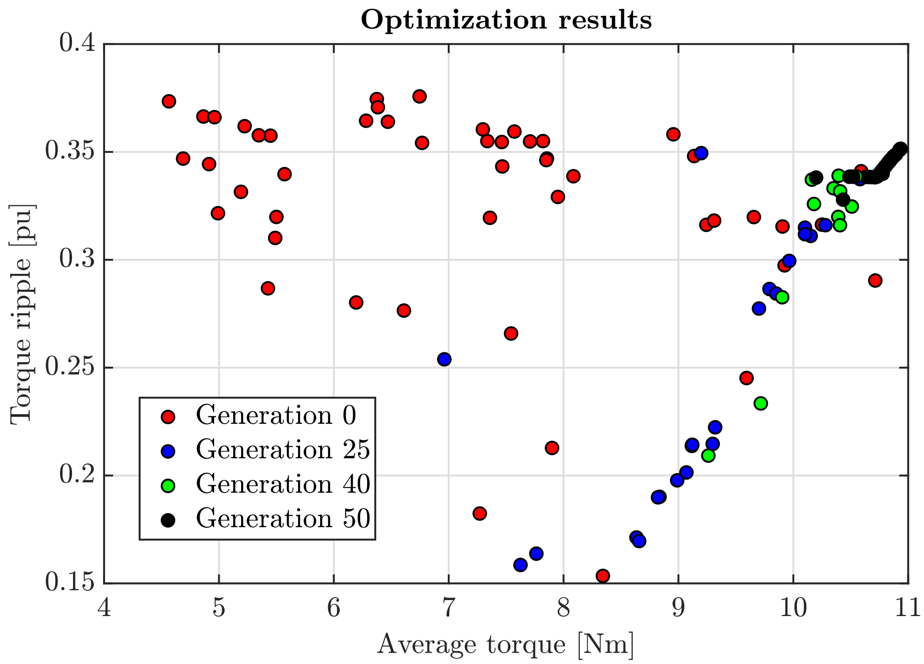

Figure 5-17: Topology optimization results for different generations

identified, first one is performed at rated load to evaluate torque and second one is performed under no load to estimate MS with BEMF.

Previous procedure yields the results in Fig. 5-21, from which several conclusions can be extracted. Increasing AlNiCo5 on slot sides (l_m) has a negative impact on average torque, because rare-earth magnet content of the machine is decreased. On the contrary, this modification improves remagnetization capability, as low-coercitivity magnet content is augmented. Also, note how the intersection between remagnetization capability and average torque occurs at lower torque values as NdFeB on slot center (h_m) is increased. Torque ripple seems to exhibit a cyclic pattern, in which a clear monotony can not be identified. However, local minimums are present for specific values of l_m. This minimums seem to be located close to the intersection between average torque and remagnetization capability. From this analysis, highlighted case in the image is selected, since it coincides with a local minimum on torque ripple, and the leftmost intersection between average torque and remagnetization capability.

Torque output for both the initial and the optimized design is compared in Fig.

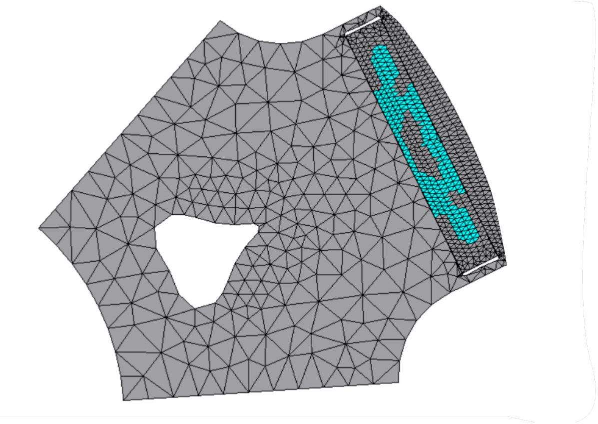

(a) Not feasible

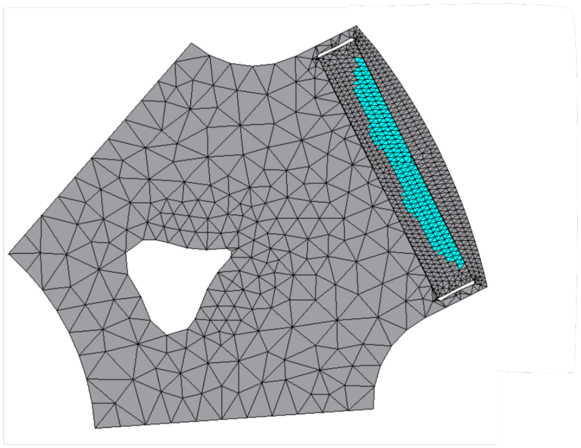

(b) Feasible

Figure 5-18: Some obtained topologies after NGnet optimization

5-22, in which the machines have been fed with rated current at their quadrature axis. Average torque has been increased from 9.01 Nm to 9.44 Nm and ripple has been reduced from 13.47% to 9.40%. In sight of previous figures, the optimization can be concluded as beneficial in terms of torque performance.

Finally, it must be verified that the machine can be demagnetized and remagnetized with short current pulses that do not take excessive values. This situation is illustrated in Fig. 5-23, in which a demagnetizing pulse of 3 pu is followed by a remagnetizing pulse of 6 pu. The image shows induced BEMF at nominal speed under no load. Fundamental component before the pulses is taken as 100% MS. After the

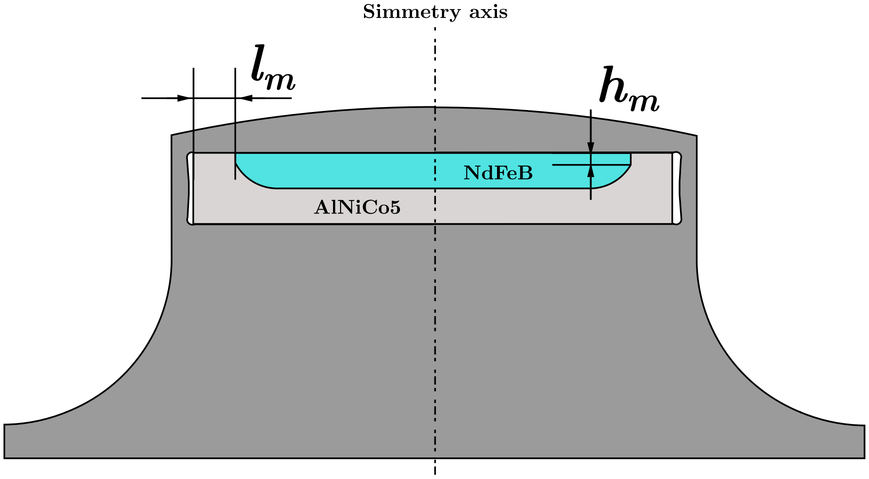

Figure 5-19: Parametric definition of optimized topology

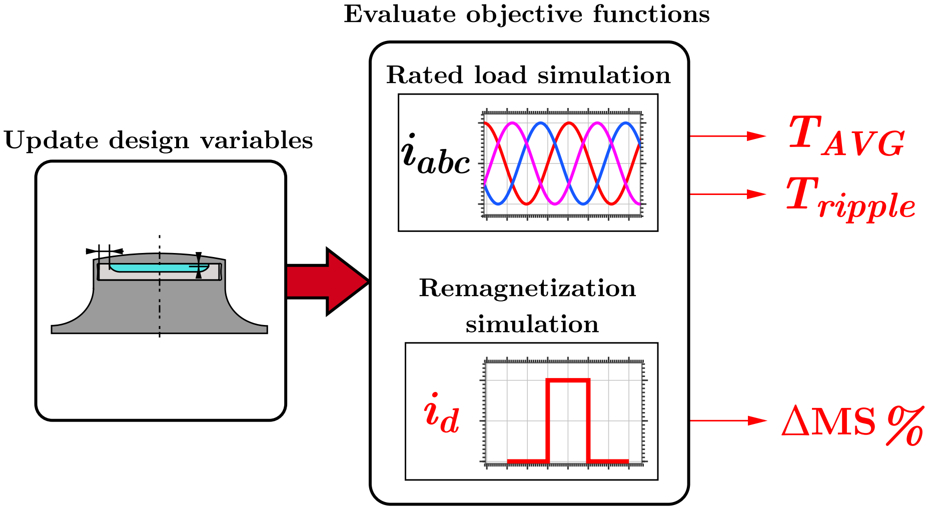

Figure 5-20: Workflow for described parametric optimization

first pulse, machine MS is effectively reduced to 65% MS. When the remagnetizing pulse is injected, machine MS is brought back to 100% MS, thus validating the design in terms of MS manipulation.

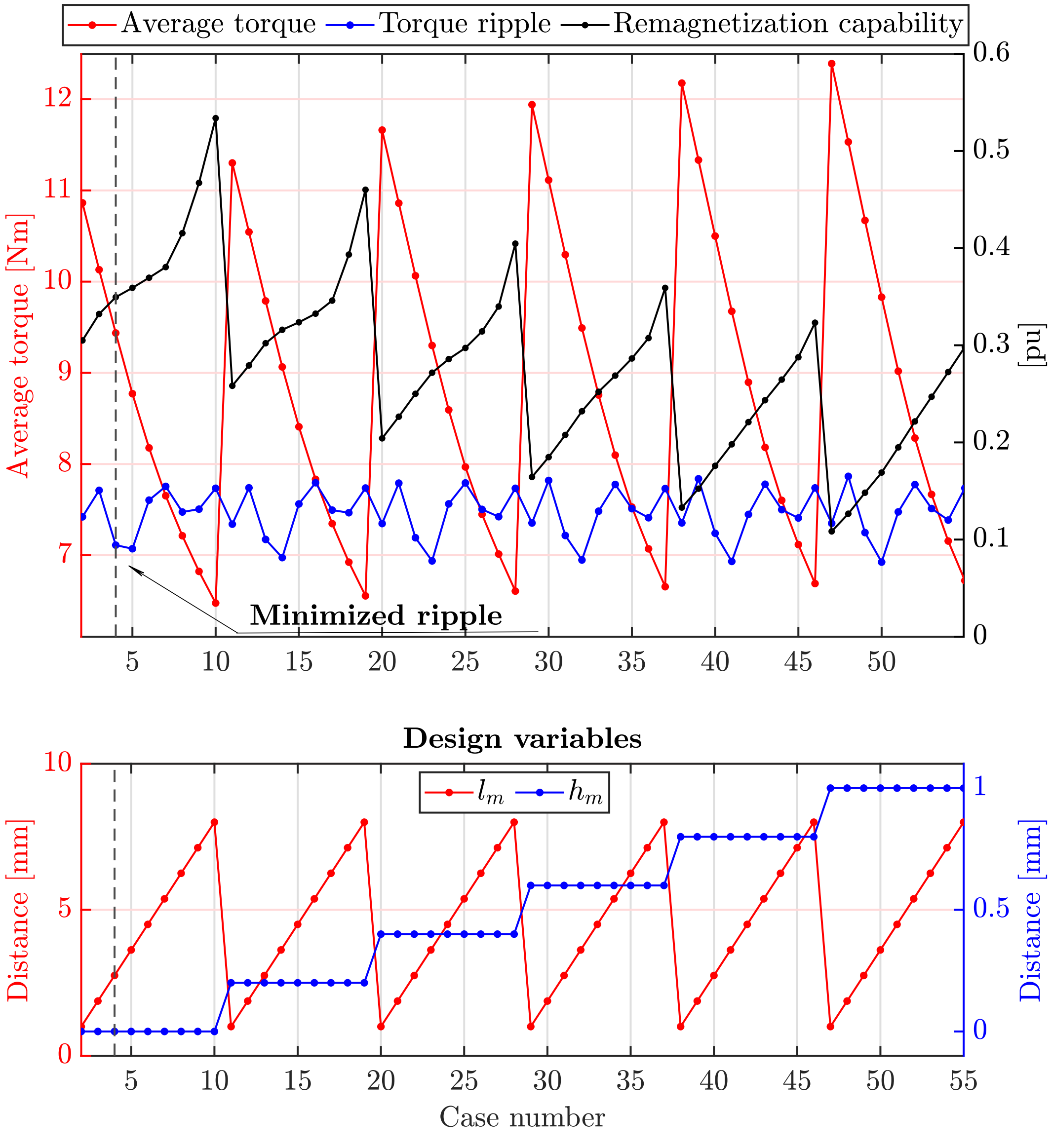

Figure 5-21: Obtained results after parametric sweep

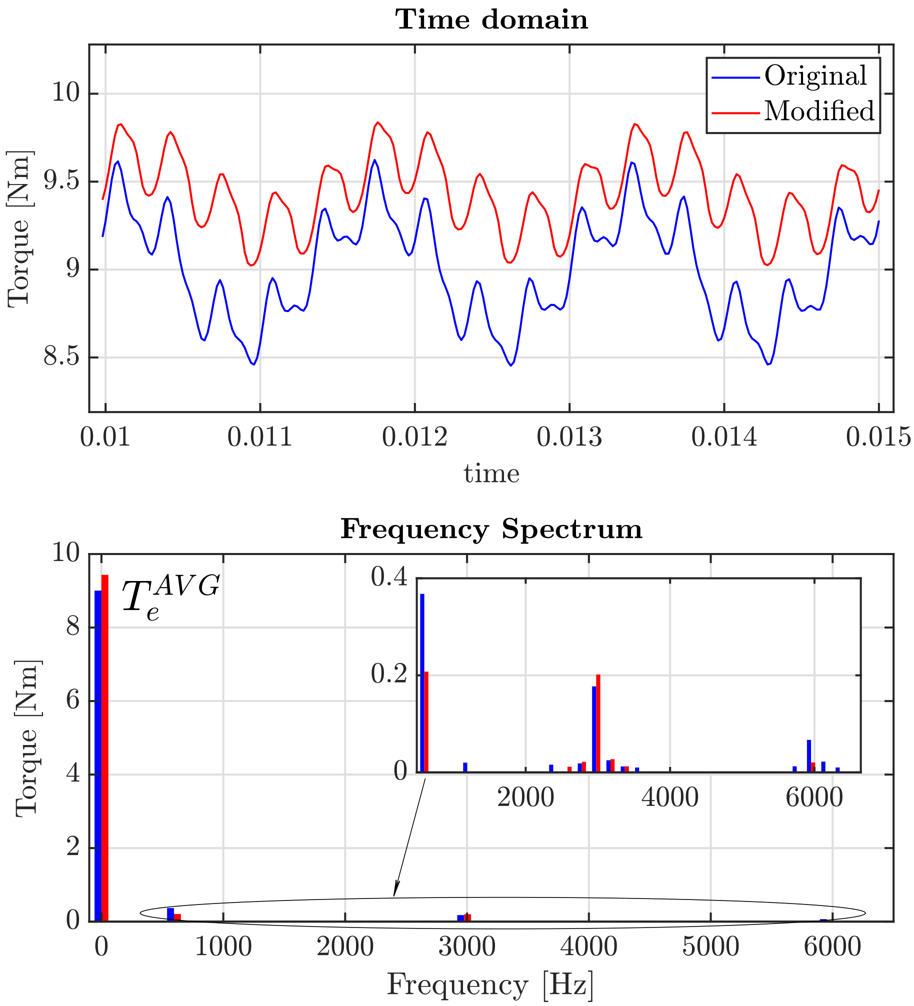

Figure 5-22: Torque comparison among machine designs

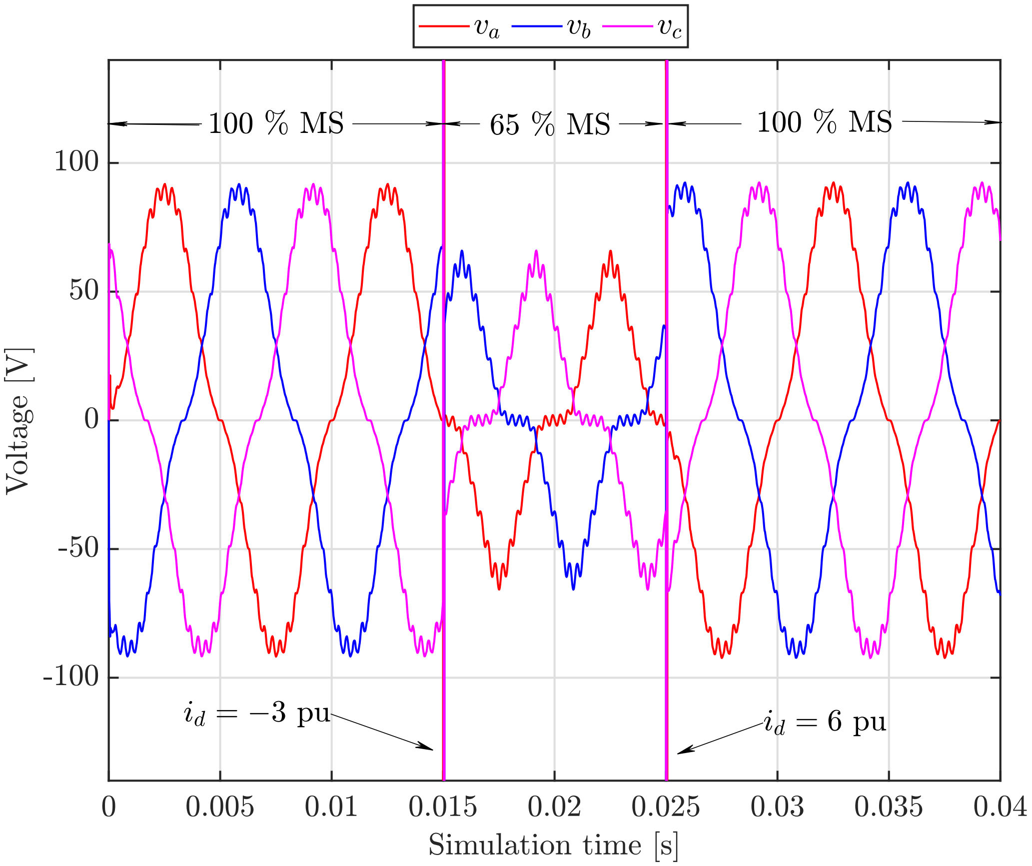

Figure 5-23: Induced BEMF for optimized design at $\omega_r = 1500$ RPM after MS manipulation

Chapter 6

Conclusions and future work

This chapter summarizes the conclusions obtained during the present master thesis. Additionally, future work to be developed will be proposed.

6.1 Conclusions

This work is part of a project aiming to study VF-PMSM adoption into aircraft applications. Its objectives were previously listed and can be summarised as:

- Comprehend VF-PMSM peculiarities against conventional permanent magnet machines
- Explore design optimization techniques and incorporate them into prototypes
- Understand power loss production mechanisms, as well as permanent magnet materials behaviour using both simulations and experimental data
- Use all previous information to research on potential impact of VF-PMSM on aircraft applications

After the completion of the work, several experiments were performed:

- Permanent magnet experimental characterization
- Iron loss measurement in known topology

- Machine efficiency measurement at different magnetization levels

Obtained data is then considered to feed simulation models. Then, these models have been used to address VF-PMSM impact in aircraft applications. Preliminary results show that average efficiency over a flight profile can be increased by 6.16% only due to MS manipulation, reducing energy consumption by 7.5%.

Additionally, finite-element software was used to improve an existing machine prototype, which is currently under development. Magnet behaviour was experimentally obtained and used to propose an optimized arrangement, showing an average torque increase of 5% and a ripple reduction of 30.21%.

Finally, a functional back-to-back converter was developed, enabling control of future prototypes inside a test bench.

6.2 Future work

After developed work, main objective is to complete the construction of test bench described in Fig. 2-1. This test bench will drive optimized machine design once constructed, and will be used in the future to evaluate:

- Machine efficiency as a function of magnetization level
- Detailed adjustment of simulation results
- Nature of machine power losses
- Different magnet arrangement topologies and MS estimation strategies
- Advanced control techniques: selective harmonic elimination, loss reduction, MS manipulation methods
- Extrapolation capabilities between test bench results and application results
- VF-PMSM design methodologies, using test bench results to develop higher power rating prototypes.

Bibliography

[1] V. Masson-Delmotte, P. Zhai, A. Pirani, S. L. Connors, C. Péan, S. Berger, N. Caud, Y. Chen, L. Goldfarb, M. Gomis, *et al.*, “Climate change 2021: the physical science basis,” *Contribution of working group I to the sixth assessment report of the intergovernmental panel on climate change*, vol. 2, no. 1, p. 2391, 2021.

[2] J. Cook, D. Nuccitelli, S. A. Green, M. Richardson, B. Winkler, R. Painting, R. Way, P. Jacobs, and A. Skuce, “Quantifying the consensus on anthropogenic global warming in the scientific literature,” *Environmental research letters*, vol. 8, no. 2, p. 024024, 2013.

[3] N. Oreskes, *The scientific consensus on climate change: How do we know we’re not wrong?* Springer, 2018.

[4] H. Ritchie, “Sector by sector: where do global greenhouse gas emissions come from?,” *Our World in Data*, 2020. https://ourworldindata.org/ghg-emissions-by-sector.

[5] H. Ritchie, “Cars, planes, trains: where do co emissions from transport come from?,” *Our World in Data*, 2020. https://ourworldindata.org/co2-emissions-from-transport.

[6] C. Bergero, G. Gosnell, D. Gielen, S. Kang, M. Bazilian, and S. J. Davis, “Pathways to net-zero emissions from aviation,” *Nature Sustainability*, vol. 6, no. 4, pp. 404–414, 2023.

[7] H. Ritchie, “What share of global co emissions come from aviation?,” *Our World in Data*, 2024. https://ourworldindata.org/global-aviation-emissions.

[8] S. Gössling and A. Humpe, “The global scale, distribution and growth of aviation: Implications for climate change,” *Global Environmental Change*, vol. 65, p. 102194, 2020.

[9] D. M. López Sánchez, *Air traffic and Sustainability Constraints and Paradigms: A Comprehensive Study on the Effects on Spanish Tourism and the Role of High-Speed Trains.* PhD thesis, Universitat Politècnica de València, 2023.

[10] B. Brelje and J. Martins, "Electric, hybrid, and turboelectric fixed-wing aircraft: A review of concepts, models, and design approaches," *Progress in Aerospace Sciences*, vol. 104, pp. 1–19, 01 2019.

[11] A. F. Zobaa, *Energy Storage: Technologies and Applications.* BoD–Books on Demand, 2013.

[12] M. Zareba, T. Szczegielniak, and P. Jabłoński, "Influence of the skin and proximity effects on the thermal field in a system of two parallel round conductors," *Energies*, vol. 16, no. 17, p. 6341, 2023.

[13] C. Liu, K. Chau, C. H. Lee, and Z. Song, "A critical review of advanced electric machines and control strategies for electric vehicles," *Proceedings of the IEEE*, vol. 109, no. 6, pp. 1004–1028, 2020.

[14] M. Orviz Zapico *et al.*, *Control, Diagnosis, and Monitoring of Permanent Magnet Synchronous Machines Using Search Coils.* PhD thesis, 2024.

[15] D. F. Laborda, *Control and monitoring of Variable Leakage Flux IPMSM.* PhD thesis, Universidad de Oviedo, 2022.

[16] D. W. Novotny and T. A. Lipo, *Vector control and dynamics of AC drives*, vol. 41. Oxford university press, 1996.

[17] J. Pyrhonen, T. Jokinen, and V. Hrabovcova, *Design of rotating electrical machines.* John Wiley & Sons, 2013.

[18] R. Jayarajan, N. Fernando, and I. U. Nutkani, "A review on variable flux machine technology: Topologies, control strategies and magnetic materials," *IEEE Access*, vol. 7, pp. 70141–70156, 2019.

[19] V. Ostovic, "Memory motors-a new class of controllable flux pm machines for a true wide speed operation," in *Conference Record of the 2001 IEEE Industry Applications Conference. 36th IAS Annual Meeting (Cat. No.01CH37248)*, vol. 4, pp. 2577–2584 vol.4, 2001.

[20] A. Athavale, K. Sasaki, B. S. Gagas, T. Kato, and R. D. Lorenz, "Variable flux permanent magnet synchronous machine (vf-pmsm) design methodologies to meet electric vehicle traction requirements with reduced losses," *IEEE Transactions on Industry Applications*, vol. 53, no. 5, pp. 4318–4326, 2017.

[21] N. Limsuwan, T. Kato, K. Akatsu, and R. D. Lorenz, "Design and evaluation of a variable-flux flux-intensifying interior permanent-magnet machine," *IEEE Transactions on Industry Applications*, vol. 50, no. 2, pp. 1015–1024, 2014.

[22] S.-H. Kim, *Electric motor control: DC, AC, and BLDC motors.* Elsevier, 2017.

[23] J. F. Mora and J. F. Ardanuy, *Accionamientos eléctricos.* Ibergarceta publicaciones, 2016.

[24] J. F. Gieras and J.-X. Shen, *Modern Permanent Magnet Electric Machines: Theory and Control.* CRC Press, 2022.

[25] A. Selema, M. Gulec, M. N. Ibrahim, R. Sprangers, and P. Sergeant, "Selection of magnet wire topologies with reduced ac losses for the windings of electric drivetrains," *IEEE Access*, vol. 10, pp. 121531–121546, 2022.

[26] G. Du, W. Ye, Y. Zhang, L. Wang, T. Pu, and N. Huang, "Comprehensive analysis of the ac copper loss for high speed pm machine with form-wound windings," *IEEE Access*, vol. 10, pp. 9036–9047, 2022.

[27] M. Zareba, T. Szczegielniak, and P. Jabłoński, "Influence of the skin and proximity effects on the thermal field in a system of two parallel round conductors," *Energies*, vol. 16, no. 17, p. 6341, 2023.

[28] M. Popescu and D. G. Dorrell, "Skin effect and proximity losses in high speed brushless permanent magnet motors," in *2013 IEEE Energy Conversion Congress and Exposition*, pp. 3520–3527, IEEE, 2013.

[29] S. Xue, J. Feng, S. Guo, J. Peng, W. Chu, and Z. Zhu, "A new iron loss model for temperature dependencies of hysteresis and eddy current losses in electrical machines," *IEEE Transactions on Magnetics*, vol. 54, no. 1, pp. 1–10, 2017.

[30] M. F. B. Omar, E. B. Sulaiman, I. A. Soomro, M. Z. B. Ahmad, and R. Aziz, "Design optimization methods for electrical machines: A review," *Journal of Electrical Engineering & Technology*, vol. 18, no. 4, pp. 2783–2800, 2023.

[31] T. Sato, H. Igarashi, S. Takahashi, S. Uchiyama, K. Matsuo, and D. Matsuhashi, "Shape optimization of rotor in interior permanent magnet motor based on topology optimizationmethod using normalized gaussian network," *D*, vol. 135, no. 3, pp. 291–298, 2015.

[32] X. Guo, H. Yang, and R. Tu, "Multi-objective sequential topology optimization method of interior pm machine based on ngnet," in *2023 IEEE 6th International Electrical and Energy Conference (CIEEC)*, pp. 4566–4571, 2023.

[33] R. Du and P. Robertson, "Dynamic jiles–atherton model for determining the magnetic power loss at high frequency in permanent magnet machines," *IEEE Transactions on Magnetics*, vol. 51, no. 6, pp. 1–10, 2014.

[34] S. Hussain and D. A. Lowther, "Prediction of iron losses using jiles–atherton model with interpolated parameters under the conditions of frequency and compressive stress," *IEEE Transactions on Magnetics*, vol. 52, no. 3, pp. 1–4, 2016.

[35] J. F. Mora, *Máquinas eléctricas*, vol. 5. McGraw-Hill, 2008.

[36] A. Bills, S. Sripad, W. L. Fredericks, M. Singh, and V. Viswanathan, "Performance metrics required of next-generation batteries to electrify commercial aircraft," *ACS Energy Letters*, vol. 5, no. 2, pp. 663–668, 2020.

[37] B. Jux, S. Foitzik, and M. Doppelbauer, “A standard mission profile for hybrid-electric regional aircraft based on web flight data,” in *2018 IEEE International Conference on Power Electronics, Drives and Energy Systems (PEDES)*, pp. 1–6, 2018.

[38] J. P.How, “*Aircraft Stability and Control*,” *Fall 2004*, vol. https://ocw.mit.edu/courses/16-333-aircraft-stability-and-control-fall-2004/, Massachusetts Institute of Technology: MIT OpenCourseWare. License: Creative Commons BY-NC-SA.

[39] D. Lawhorn, V. Rallabandi, and D. M. Ionel, “Electric aircraft system co-simulation including body, propeller, propulsion, and energy storage models,” in *2019 IEEE Transportation Electrification Conference and Expo (ITEC)*, pp. 1–5, IEEE, 2019.

[40] M. Orviz, D. F. Laborda, D. Reigosa, J. M. Guerrero, and F. Briz, “Optimization of magnetization state manipulation in variable-flux pmsms,” in *2022 IEEE Energy Conversion Congress and Exposition (ECCE)*, pp. 1–8, 2022.

[41] “Informe del sistema eléctrico español 2021,” *Red Eléctrica de España: Madrid, Spain*, 2022.